

A MICROCHANNEL DETECTION SYSTEM FOR DRAGON

by

Michael Joseph Lamey
B.Sc., Simon Fraser University, 2001

A thesis submitted in partial fulfillment
of the requirements for the degree of
MASTERS OF SCIENCE
in the
Department of Physics

© Michael Joseph Lamey 2004
SIMON FRASER UNIVERSITY
July 2004

All rights reserved. This work may not be
reproduced in whole or in part,
by photocopy or other means,
without permission of the author.

APPROVAL

Name: Michael Joseph Lamey

Degree: Masters of Science

Title of thesis: **A MICROCHANNEL DETECTION SYSTEM
FOR DRAGON**

Examining Committee: Dr. Jeff Sonier (chair)
Associate Professor, Department of Physics

Dr. John D'Auria (Senior Supervisor)
Professor, Department of Chemistry

Dr. David Hutcheon (Supervisor)
Senior Research Scientist, TRIUMF

Dr. Michel Vetterli (Supervisor)
Professor, Department of Physics

Dr. Barry Davids (Internal Examiner)
Adjunct Professor, Department of Physics

Date Approved: July 16, 2004

Abstract

The DRAGON facility at TRIUMF-ISAC was designed to measure the rates of astrophysically important nuclear reactions involving radioactive reactants. To this end, the mass spectrometer was designed to separate the result of a radiative proton or alpha capture reaction, between beam and target nuclei, from the beam itself. Yields are typically on the order 10^{-9} to 10^{-15} , thus, the feasibility of a particular reaction is driven by the suppression of the relatively intense beam, to that of the capture product. In the case of Nova explosions, important resonances occur at low beam energies (0.15 to 1.0 MeV/u) where the DRAGON suppression may be reduced.

An MCP (Micro Channel Plate) detection system has been commissioned to be used in a local time-of-flight approach for particle identification at the focal plane of the DRAGON recoil mass separator. It is the goal of this additional detection system to enhance the current suppression systems without significant loss in efficiency. Three properties of the MCP system have been investigated: the timing resolution, the efficiency and the position resolution. Two sources, ^{68}Ge and ^{148}Gd , were used off-line to test the detection system performance. The timing studies were performed with the use of a fast PMT (Photo Multiplier Tube) as a second detection system. A DSSSD (Double Sided Silicon Strip Detector) was used for the efficiency tests and masks were used during the position resolution studies. These off-line tests were followed by on-line studies of the well known resonance ($E_{cm} = 258.6$ keV) in the $^{21}\text{Ne}(p,\gamma)^{22}\text{Na}$ reaction. A simulation using the RELAX3D software along with a custom made tracking code, both written at TRIUMF, has also been studied, and its results pertaining to the three aforementioned important properties will be discussed.

This thesis is dedicated in loving memory to my mother.

Calvin: I've been reading about the beginning of the universe. They call it "the big bang."

Calvin: Isn't it weird how scientists can imagine all the matter of the universe exploding out of a dot smaller than the head of a pin, but they can't come up with a more evocative name for it than "the big bang"?

Calvin: That's the whole problem with science. You've got a bunch of empiricists trying to describe things of unimaginable wonder.

Hobbes: What would you call the creation of the universe?

Calvin: The Horrendous space kablooje!

Bill Watterson

Acknowledgements

There are several people who have contributed to the work herein. Dave Hutcheon was always available to answer my questions or at least listen to my ideas no matter how far fetched they may have seemed. Dan Melconian did a lot to help out regarding the fits used and introduced me to the software packages used for the analysis. He always took the time to explain the methods used with regard to the data analysis, thanks Dan.

Dave Ottewell, Art Olin and Lothar Buchmann were also available whenever I had questions and always provided helpful comments. Larry Root wrote the simulation used and showed a genuine interest in its success, he was also helpful in answering the several questions I had with regards to how it worked. I would also like to thank Peter Machule and Robert Openshaw whose technical expertise was appreciated.

Steve Chan and Herb Coombs helped out with the design considerations of the phototube used. They also displayed a genuine interest in the results obtained, also thankyou Herb for taking time to show me how to properly setup the CFD.

Thankyou to ISAC operations for delivering and tuning the beams used. I would also like to thank Barry Davids and Mike Vetterli for taking the time to read my thesis and be part of the committee. I extend a special thanks to Mike for working with me after the defense. Thankyou Dario, Chris, Jonty and Mike T for their shift work and hand in setting up DRAGON before beam delivery. Also thankyou Chris wrede for the lunch time discussions which allowed a break in the day.

Finally I would like to thank my supervisor John D'Auria, I may not have attended grad school without his encouragement. Your drive and determination toward the success of the DRAGON program is admirable. I have enjoyed working under your tutelage, thankyou.

Table of Contents

Approval	ii
Abstract	iii
Dedication	iv
Quotation	v
Acknowledgements	vi
Table of Contents	vii
List of Tables	x
List of Figures	xi
Chapter 1 Introduction	1
1.1 Novae	2
1.2 Supernovae	4
1.3 X-Ray Bursts	5
1.4 CNO cycle and rp-process	5
Chapter 2 Experimental Facilities	7
2.1 ISAC	7
2.2 DRAGON	10

2.2.1	The Windowless Gas Target	12
2.2.2	The BGO Array	14
2.2.3	The Magnetic and Electric Elements	16
2.2.4	End Detectors	18
Chapter 3	The Microchannel Plate System	23
3.1	Resistive Anode Encoder	24
3.2	The DRAGON Microchannel Plate	25
3.2.1	Gain and Pulse Height Distribution	27
3.2.2	Dark Current	27
3.2.3	The Detection System	28
Chapter 4	The Detection System Simulation	31
4.1	Secondary Electrons	38
Chapter 5	Testing of the DRAGON MCP	40
5.1	Timing	40
5.1.1	The Photomultiplier and Scintillator	41
5.1.2	Work Station, Electronics and Time Calibration	42
5.1.3	Studies using a ^{68}Ge Source	45
5.1.4	Studies using a ^{148}Gd Source	50
5.1.5	Studies Using ^{21}Ne at $E_{cm} = 258.6$ keV	54
5.1.6	Simulation results	67
5.2	Efficiency	71
5.2.1	Optimization and Efficiency	71
5.2.2	Simulation Results	73
5.3	Position Resolution and Linearity	74
5.3.1	Simulation results	80
Chapter 6	Future Considerations	85
Chapter 7	Conclusions	88

Appendix A	MCP Mirror Assembly	90
Appendix B	Mass Monte Carlo	94
Bibliography		98

List of Tables

2.1	Yields of resonant capture reactions involving specific states. These reactions were approved by the TRIUMF EEC.	12
2.2	Properties of the DRAGON Electric and Magnetic Dipoles.	18
3.1	Selected properties of the DRAGON MCP detection setup.	27
5.1	Summary of the Results from the analysis of the time calibration data.	45
5.2	Previous runs used to calibrate the measured energy of the DSSSD. . .	63
5.3	MCP detection efficiency for various numbers of secondary electrons. .	72
5.4	MCP system detection efficiency as a function of preamplifier discriminator threshold.	73
5.5	Selected properties of the DRAGON MCP detection setup.	84

List of Figures

1.1	Artist's view of the accretion of matter, in a binary star system, from an extended main sequence star to a dense companion. © Chris Ruiz, 2002, by permission.	3
1.2	The CNO cycle.	6
2.1	3-d schematic of the ISAC facility at TRIUMF showing the proton beam line, the ISAC accelerators and the location of the DRAGON facility. © TRIUMF, 2003, by permission.	8
2.2	Plan view of the ISAC accelerator at TRIUMF. Stable beam is extracted from the Off-Line Ion Source (OLIS), the switchyard can then be used to guide the beam toward the higher energy experiments. © TRIUMF, 2004, by permission.	9
2.3	3-d illustration of DRAGON displaying the layout of the facility. Also labelled are the important features. © TRIUMF, 2002, by permission.	11
2.4	The DRAGON windowless gas target. As illustrated, beam enters from the left. © TRIUMF, 2002, by permission.	13
2.5	Schematic of the DRAGON pumping system illustrating the gas recirculation. © TRIUMF, 2002, by permission.	13
2.6	DRAGON BGO array surrounding the gas target. © Dario Gigliotti, 2002, by permission.	15
2.7	Originally proposed detection system for DRAGON. Energy loss along each anode is indicated by the lines above them. © TRIUMF, 2001, by permission.	19

2.8	$^{13}\text{C}(\text{p},\gamma)^{14}\text{O}$ ionchamber data. Shown is the energy collected in anode1 versus the total energy collected.	20
2.9	Schematic diagram of the current MCP detection system. Heavy ions knock out low energy electrons from a thin foil which are accelerated and deflected on the MCP. The heavy ion continues along its original trajectory to be detected downstream.	22
3.1	Schematic operating principle of an MCP. Input radiation initiates the avalanche process.	24
3.2	Schematic diagram of the arc shaped RAE. Also shown is the circular projection of the MCP.	24
3.3	Side view of a chevron configuration of a microchannel plate detection system with an anode for position sensitivity.	26
3.4	Pulse height distribution of the DRAGON microchannel plate.	27
3.5	Photo of the DRAGON Microchannel Plate detection system.	29
3.6	Schematic of the electronics of the MCP-RAE system. The HV_{in} is supplied by a Stanford Research Systems PS350 model power supply.	30
4.1	Mesh approximation of a $20\ \mu\text{m}$ wire with a 3x3 grid.	33
4.2	A plot of contours around the DRAGON MCP mirror setup solved using RELAX3D. These should be compared to Figure 2.9.	34
4.3	A close up of the contours around two wires of the first grid.	34
4.4	Theta, phi and energy distributions of 20000 electrons started at the carbon foil. Also shown is the definition of phi, similarly θ is the angle between the x-axis and the projection of the electron velocity vector onto the xy-plane.	35
4.5	Schematic illustrating the electron tracking method, using numerical interpolation and differentiation.	37
5.1	Calibration of the MCA scale using an ORTEC 462 Time Calibrator.	43
5.2	First peak of the calibration data in Figure 5.1 with the fit shown.	44

5.3	Top: Linear fit of the calibration of the MCA data from Table 5.1. Relative time is that from the first calibration peak. Bottom: fitted line along with the slope from peak to peak.	46
5.4	DRAGON “final slit” box components including the MCP setup as shown. © TRIUMF, 2000, by permission.	46
5.5	Box diagram of the electronics used for the PMT-MCP timing tests. . .	47
5.6	Results from the first run of a MCP-PMT1 coincidence with a ^{68}Ge 511 keV gamma source.	48
5.7	Results from the run of a MCP-PMT2 coincidence with a ^{68}Ge 511 keV gamma source.	48
5.8	Results from the run of an PMT1-PMT2 coincidence with a ^{68}Ge 511 keV gamma source.	49
5.9	The fast PMT and puck used during the timing studies of the MCP. . .	51
5.10	Simplified schematic of the timing studies performed with a ^{148}Gd alpha source.	52
5.11	Top: Background pulse height spectra above the 750 mV threshold on the CFD. Bottom: Background corrected pulse height spectra from the 3.183 MeV ^{148}Gd alphas.	52
5.12	Coincidence spectrum between the MCP and PMT with a 3.183 MeV ^{148}Gd alpha source.	53
5.13	Electronics schematic with a PMT at the end of DRAGON.	55
5.14	Coincidence spectra between the MCP and a PMT mounted at the end of DRAGON.	56
5.15	SRIM simulation of the spread in energy of 5.664 MeV ^{21}Ne after transmission through a $20\text{ }\mu\text{g}/\text{cm}^2$ carbon foil.	57
5.16	Timing spectra showing the clear separation of ^{22}Na from ^{21}Ne . Also shown in the blue curve are the counts in coincidence with the BGO array.	59
5.17	Electronics used with the DSSSD at the end of DRAGON.	60
5.18	Data from the $^{21}\text{Ne}(p,\gamma)^{22}\text{Na}$ reaction. (a) Time of Flight spectra of ^{21}Ne and ^{22}Na between the MCP and DSSSD. (b) Energy spectra of ^{21}Ne and ^{22}Na from the DSSSD.	61

5.19	Data from the $^{21}\text{Ne}(p,\gamma)^{22}\text{Na}$ reaction. (a) Two dimensional plot of energy versus time of flight. (b) Et^2 mass spectra of the leaky beam and recoils.	62
5.20	Blowup of the energy vs. time plot for attenuated ^{21}Ne beam from the MCP-DSSSD setup illustrating the strong energy-time correlation. . . .	66
5.21	Transit time of the secondary electrons from the carbon foil to the MCP.	67
5.22	Results from the Monte Carlo simulation of an Et^2 analysis.	69
5.23	Simulated results for the $^{17}\text{F}(p,\gamma)^{18}\text{Ne}$ reaction. (a) Mass plot of the ^{17}F and ^{18}Ne particles. (b) Time of flight of the ^{17}F and ^{18}Ne particles.	70
5.24	Number of secondary electrons reaching the MCP, from a point source stepped in 0.2 mm intervals. 5000 electrons were started in each case. .	74
5.25	(a) Mask used to test the position resolution of the MCP/RAE system. (b) Mask used to test the 2-d linearity of the RAE.	75
5.26	The four position signal extracted from the RAE. The Poisson-like distribution is a result of the Poisson-like behaviour of the MCP amplification and the number of secondary electrons produced.	76
5.27	(a) 2-d spectra resulting from a mask placed at the foil position. (b) X spectra of the projection along a line of mask holes.	77
5.28	2-d spectrum obtained with ^{21}Ne bombarding the mask shown in Figure 5.25(a).	78
5.29	(a) Z spectrum of the projection along a line of mask holes. (b) Y spectra of the projection along a line of mask holes.	79
5.30	Folding of the projection of a circular hole and Gaussian noise.	80
5.31	Z and Y spatial distributions resulting from 5000 electrons started off at the center of the foil.	81
5.32	Trajectories of several electrons started out with random initial conditions.	81
5.33	Illustration of the focusing properties of the wire plane used for the electron mirror setup. Shown are several electron trajectories and the effect the field around the wire's on their path.	82

5.34	(a) Resulting Z position spectra from a point source after averaging the position of every 11 th electron. (b) Resulting Y position spectra from a point source after averaging the position of every 11 th electron.	83
6.1	Illustration of a possible setup with magnetic fields in order to attain improved position resolution.	86
A.1	Detailed schematic of the entrance grid (grid 1), with a few of the 20 μm wires shown. All dimensions are in inches unless otherwise stated. .	91
A.2	Detailed schematic of the 45° grids (grids 2 and 3), with a few of the 20 μm wires shown. All dimensions are in inches unless otherwise stated.	92
A.3	Detailed schematic of the grid just in front of the MCP (grid 4), with a few of the 20 μm wires shown. All dimensions are in inches unless otherwise stated.	93

CHAPTER 1

Introduction

Particle detectors have played a key role in the discovery of “new” particles. They provide the experimenter a direct connection to the fundamental building blocks of nature. These detectors have become more advanced and have given researchers a probe to quench one of our deepest thirsts, the quest for knowledge. Some of the first of these detectors were described in a small book by J. Chadwick entitled *Radioactivity and Radioactive Substances* back in 1923 [1]. He describes two methods of counting alpha particles, the scintillation method and the electrical method. The scintillation method involved the use of a phosphorescent zinc sulfide screen. In those days the experimenter counted the number of scintillations seen over a given period of time. As one could imagine this would be a very tedious task. Luckily, for us, the electrical method took off and has become a powerful technique, not only for alpha particle detection, but for particles in general. The α -ray electroscope as it was called consisted of a gold leaf whose deflection angle from a rod depended on the charge on the rod and leaf. As charge is collected from the ionization by the alpha particles the charge on the rod and leaf decreases, leading to a slow decline in the angle of the leaf. The rate of this decline is a measure of the amount of charge collected over time. Using standard sources one could then determine the decay rate of the sample.

In the preface to the first edition Chadwick writes the following: *The study of radioactive elements is in some respects far more important than the study of the ordinary stable elements... The processes of radioactive transformations are indeed of fundamental nature; they throw light on the detailed structure of the atom, the problem which lies at the basis of physics and chemistry.* Although it’s taken a bit out of context the same may be said of the current state of theoretical and experimental

nuclear astrophysics. One of the biggest questions we wish to solve is: how were the elements produced? We believe that only trace quantities of elements heavier than mass 7 were produced by the Big Bang, yet life depends on the existence of these heavier elements.

One of the major breakthroughs in nuclear astrophysics was when Fred Hoyle predicted the existence of an excited state in ^{12}C which allowed the synthesis of ^{12}C to proceed much faster than previously thought. Until this time astronomers had always believed that the synthesis of the elements occurred at the time of the Big Bang [2]. It was not long after this discovery that the view on how the elements were made changed.

Nuclear astrophysics is concerned with understanding of the production of the elements. Leading candidates for the sites of this production are novae, supernovae and to a lesser extent x-ray bursts. The experimental data from observations of these explosive events provides a tool toward our understanding of nucleosynthesis. Theoretical models use these data to compare to their predicted abundances. It is one of the goals of experimental nuclear astrophysics to provide the relevant data for these models. Two of the biggest unknowns remaining for nucleosynthesis calculations are the masses of nuclei far from stability [4], and the reaction rates of radioactive species [11]. Explosive environments such as novae and supernovae are believed to be sites upon which the distribution of the elements has been partially produced. Observations of the ejecta of the events tag the production of certain elements in the explosion [3].

This work was concerned with the commissioning of a microchannel plate detection system, for the Detector of Recoils And Gammas Of Nuclear reactions (DRAGON) facility. DRAGON was designed to measure resonance strengths for reactions of astrophysical importance.

1.1 Novae

The current model of the nova process involves a binary-star system comprised of a white dwarf and an extended main sequence star. The main sequence star loses mass to its compact companion, leading to the end result of an explosion. An artist's

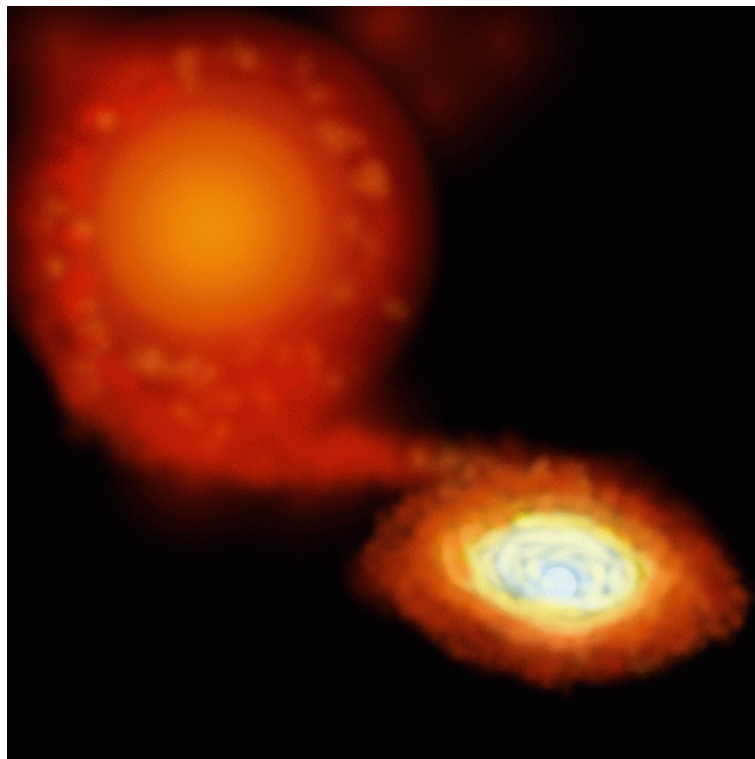


Figure 1.1: Artist's view of the accretion of matter, in a binary star system, from an extended main sequence star to a dense companion. © Chris Ruiz, 2002, by permission.

impression of the nova mechanism is shown in Figure 1.1. In 1964 reference [5] developed the theory that the explosion took place in a binary system. The idea that the nova outburst was caused by mass transfer was suggested by [6]. The main sequence star fills its Roche lobe[†] and loses mass, predominantly comprised of H_2 or He, to its white dwarf companion. As matter accumulates on the surface of the white dwarf an envelope of accreted material builds up.

As accreted material accumulates on the surface of the white dwarf temperatures at the bottom of the envelope increase to the extent where nuclear reactions can occur. These reactions proceed as a degenerate gas, that is, constant density and pressure

[†]The Roche lobe is one of the gravitational equipotentials of the binary system. It is where the forces from the two objects in the binary system exactly cancel.

conditions of the degenerate white dwarf, causing rapid increases of the surrounding temperature. In a normal gas as the temperature increases the gas expands and results in a decrease in temperature. Due to the temperature dependance of charged particle nuclear reactions, as the temperature increases so do the rates. This all leads to a thermonuclear runaway and a violent outburst. The early stages of the runaway energy generation are primarily a result of the p-p reactions. However during the final stages of the runaway the energy generation is primarily a result of the CNO cycle [7]. It has been suggested [8] that the overall enrichment of matter nova explosions provide to the galaxy is small, however, these explosions may make significant contributions to particular nuclei near the CNO cycle or NaNe cycle regions [9].

1.2 Supernovae

Much like nova explosions, a supernova is a star which experiences a sudden increase in luminosity. The underlying difference is the magnitude of the catastrophic event. A supernova can reach luminosities up to $10^9 L_{\odot}^{\ddagger}$, 10^6 greater than that of a nova event [10]. Generally supernovae are categorized in two main groups; those which are hydrogen poor (Type-I) and those which are hydrogen rich (Type-II). Type-II supernovae are the result of the familiar core collapse of main sequence stars with $M > 8M_{\odot}^*$ [15]. Under the massive gravitational conditions neutronization occurs and the r-process, rapid neutron capture, is believed to determine the path for heavy element production.

We begin to understand the magnitude of these outbursts if we consider the following. The remnant of the last supernova to have exploded in our galaxy, the Vela remnant, indicates that the explosion occurred around 9000 B.C. [10]. Given its proximity to earth, $\approx 103 \times 10^6$ A.U.^{††}, it is believed that it may have been as bright as the moon. It's hard not to be in awe of such a catastrophic event.

[‡] L_{\odot} is the standard shorthand of the solar luminosity.

^{*} M_{\odot} is the solar mass.

^{††} A.U. or Astronomical unit is the average distance from the earth to the sun.

1.3 X-Ray Bursts

The standard model of an x-ray burst is very similar to that of a nova explosion, with the significant difference being that the compact object is a neutron star rather than a white dwarf. In this case nuclear burning is ignited with densities $\approx 10^3$ times larger than those in nova explosions [11]. Peak temperatures up to $T = 2$ GK can be reached before the degeneracy is completely lifted [12]. It is believed that the energy generation from the 3α -process drives the runaway [13]. These x-ray bursts should be distinguished from x-ray pulsars. As material in the accretion disk spirals toward the neutron star it loses energy in the form of x-rays. We then observe these x-rays as pulses due to the rotation or revolution of the neutron star, and thus have termed the sources, x-ray pulsars.

Generally one can split the burst up into four phases where different reactions dominate. For example the CNO cycle and the triple alpha process dominate the first and second stages respectively, while the latter stages are dominated by the α -process (alpha capture accompanied with the ejection of a proton) and rp-process (rapid proton capture) beyond the mass 56 region.

If a significant mass can escape the gravitational potential of the neutron star then elements with mass > 70 are enriched. The abundance of elements with mass > 70 on the surface of the neutron star is built up 10^6 times more than the initial accreted material abundance (Reference [11]). With such enrichments, the study of the cycles and the processes governing the energy generation is of extreme importance.

1.4 CNO cycle and rp-process

In order to understand the above high temperature events we must understand what drives the runaway or how the energy generation is produced. The CNO cycle and the rp-process are two such important processes. The CNO cycle at two different temperatures is shown in Figure 1.2. At lower temperatures the cycle results in the conversion of four protons into a ${}^4\text{He}$ particle, most of the energy liberated remains in the interior, only a small amount is carried away by the two neutrinos as result of the two β^+ decays involved. At higher temperatures the path of the reaction flow

CHAPTER 2

Experimental Facilities

The Detector of Recoils And Gammas Of Nuclear reactions (DRAGON) is in the ISAC-1 building of TRIUMF, in Vancouver, British Columbia, Canada. TRIUMF is Canada's national laboratory for nuclear and particle physics. A 3-d schematic of the facility is shown in Figure 2.1. The major components of both ISAC and DRAGON will be discussed in this chapter. The DRAGON facility consists of four major components: a windowless gas target, a Bismuth Germanium Oxide (BGO) gamma detector array surrounding the gas target, an electromagnetic recoil mass separator and a recoil detection system.

2.1 ISAC

Nuclear reactions occur over a range of energies corresponding to a large range of temperatures in stellar environments. Therefore the energies of reactions of astrophysical importance span a wide range. Thus, a facility capable of fully variable beam energy is a necessity. This makes the ISAC (Isotope Separator and ACcelerator) facility at TRIUMF ideal for the study of astrophysically important nuclear reactions. A plan view of the ISAC accelerators is shown in Figure 2.2. An ion beam from the Off-Line Ion Source (OLIS) is produced and injected into a pre-buncher. The pre-buncher operates at a fundamental frequency of 11.8 MHz, resulting in a 85 ns bunch spacing. The Low Energy Beam Transport (LEBT) then delivers this beam at 2 keV/u to the 8 m long RFQ. The RFQ operates at 35.4 MHz, focusing and accelerating the beam of $A/q \leq 30$ to 153 keV/u. A Drift Tube Linac (DTL) then accelerates the

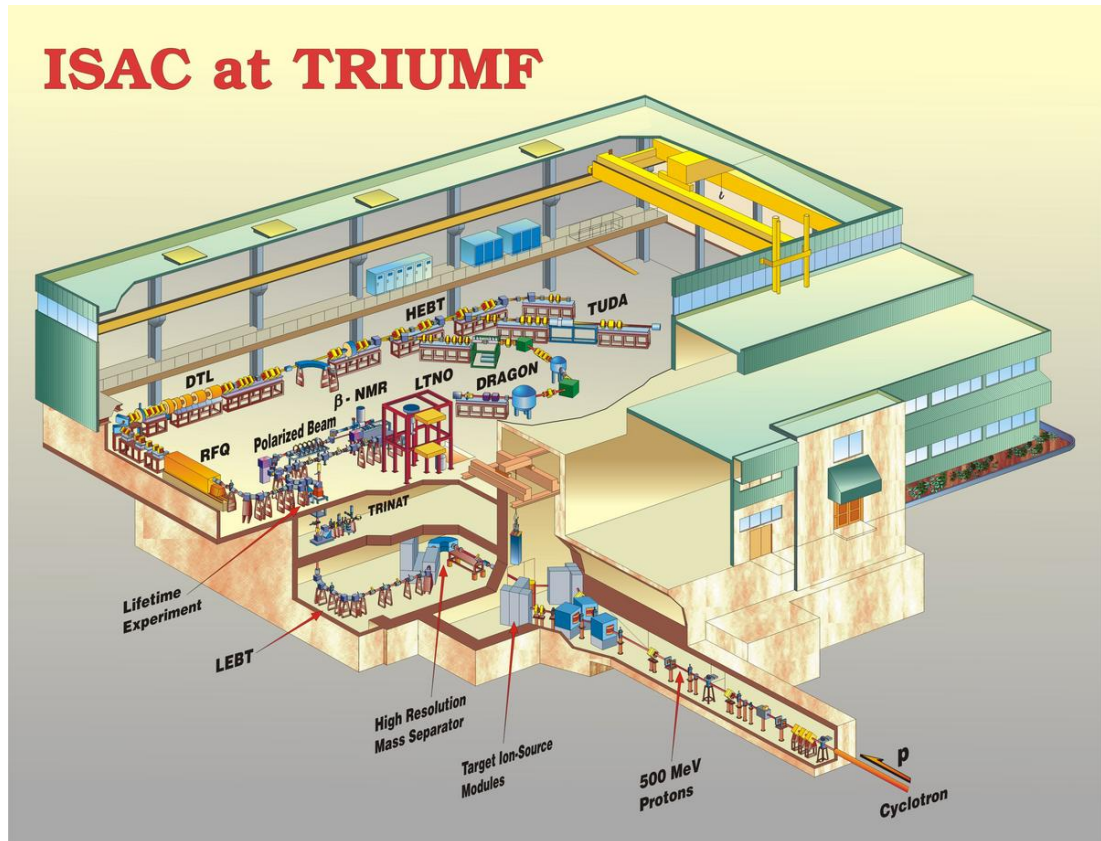


Figure 2.1: 3-d schematic of the ISAC facility at TRIUMF showing the proton beam line, the ISAC accelerators and the location of the DRAGON facility. © TRIUMF, 2003, by permission.

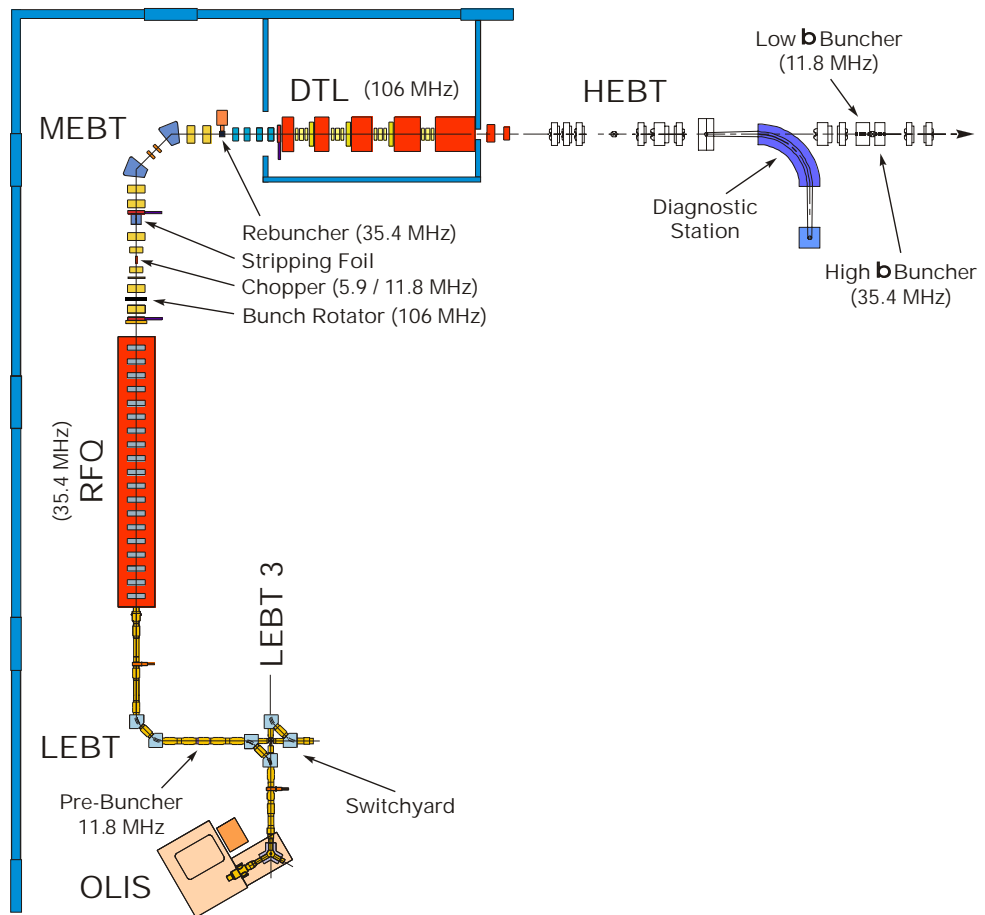


Figure 2.2: Plan view of the ISAC accelerator at TRIUMF. Stable beam is extracted from the Off-Line Ion Source (OLIS), the switchyard can then be used to guide the beam toward the higher energy experiments. © TRIUMF, 2004, by permission.

beam to a final energy fully variable between 153 keV/u and 1.73 MeV/u[†]. The High Energy Beam Transport (HEBT) system then delivers the beam to experiments like DRAGON.

Although not used during this study, the DRAGON program is dependant upon the radioactive beam facility at ISAC. Radioactive beams are produced via the ISOL technique [19], that is, bombardment of an intense, up to 100 μ A, proton beam from the 520 MeV cyclotron onto a thick target. The target then releases specific elements into an ion source where ionization takes place and a beam is extracted. The mode of beam formation depends on the proton beam energy, i.e. spallation or fusion reactions. A high resolution mass analyzer magnet is used to select the mass of interest, and suppress isobaric contaminants. The ISAC mass separator is capable of $M/\Delta M \approx 10000$ [20].

2.2 DRAGON

As previously mentioned DRAGON [76] was designed to measure radiative proton and alpha capture strengths of astrophysically important nuclear reactions, The facility is shown schematically in Figure 2.3. The measurable quantity is the ratio of the reaction product to that of the beam. Generally these yields are of the order of 10^{-9} to 10^{-15} per incident beam particle. Therefore separation and identification of the fused nuclei are important, and this is exactly what DRAGON was designed to accomplish. A beam of the desired energy from ISAC is delivered to DRAGON, impinging on an H_2 or 4He gas target[‡]. The product in an excited state releases energy by emitting one or in general several gammas. A BGO array is used to detect the high energy gammas which can be used as a tag of good events. The beam and recoils leave the target and enter two stages of mass separation. The final fate of the recoils is the detection by one or several end detectors which will be discussed below.

As previously mentioned there are four major components: a windowless gas target, a BGO array, an electromagnetic mass separator (EMS), and the final detectors. One of the original goals of DRAGON was to achieve an overall suppression of beam

[†]This energy range has been a recent improvement in the ISAC facility.

[‡]A solid target setup has been built for and used in the $^{12}C(^{12}C,\gamma)^{24}Mg$ experiment.

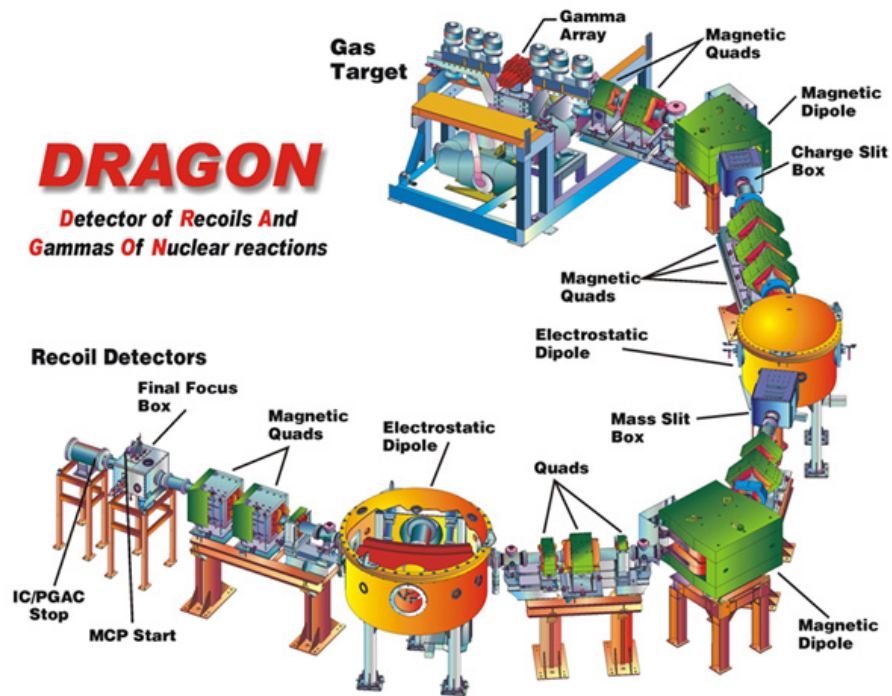


Figure 2.3: 3-d illustration of DRAGON displaying the layout of the facility. Also labelled are the important features. © TRIUMF, 2002, by permission.

particles on the order 10^{-16} . This was to be achieved by the combination of the EMS, a gamma coincidence with the BGO and an end detector system with time-of-flight and or Z -discrimination methods. The yields of some of the approved reactions proposed for DRAGON are shown in Table 2.1. These yields are those of the weakest capture strength over the proposed energy regime. Higher energy resonances are much stronger and such suppression factors are not required.

Table 2.1: Yields of resonant capture reactions involving specific states. These reactions were approved by the TRIUMF EEC.

Reaction	yield (recoils/beam)
$^{15}\text{O}(\alpha, \gamma)^{19}\text{Ne}$	1×10^{-15}
$^{26}\text{Al}(\text{p}, \gamma)^{27}\text{Si}$	3×10^{-14}
$^{17}\text{F}(\text{p}, \gamma)^{18}\text{Ne}$	1.9×10^{-14}

2.2.1 The Windowless Gas Target

Generally at nova temperatures reactions of interest occur at very low center of mass energies. In order to study these reactions, low beam energies are required and the introduction of any excess material at these energies produces unwanted scattering, straggling and possible uniformity problems. The entrance of DRAGON has been outfitted with a recirculating windowless gas target capable of maintaining thicknesses* $\approx 6.5 \times 10^{18}$ of atoms/cm² of H₂ gas.

The target is shown in Figure 2.4. Beam delivered by ISAC enters from the left. Entrance and exit apertures of 6 and 8 mm were chosen to limit the spill of radioactive beam and allow for a 20 mrad acceptance^{††}. Recently in order to increase the acceptance of DRAGON a target with 4 and 10 mm entrance and exit apertures has been constructed. Two silicon detectors mounted at 30° and 57° monitor the amount of elastically scattered protons as a measure of beam intensity passing through the target.

*The design with a larger exit aperture and pumping tubes cannot reach this target thickness.

††The acceptance here refers to that from the center of the target.

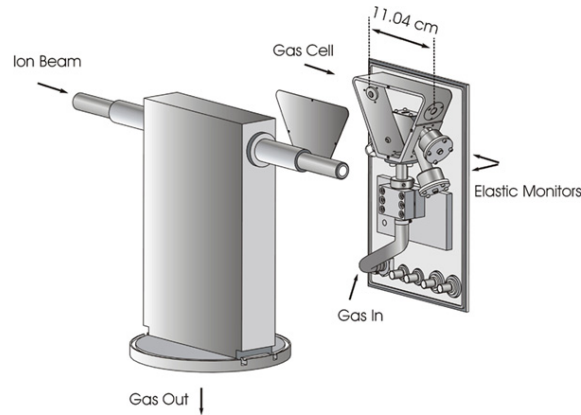


Figure 2.4: The DRAGON windowless gas target. As illustrated, beam enters from the left. © TRIUMF, 2002, by permission.

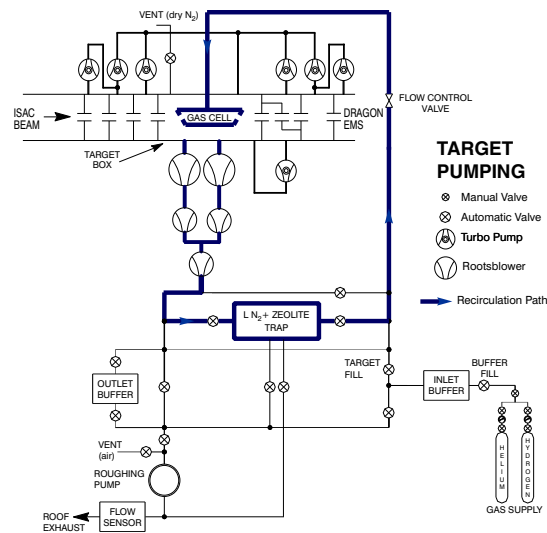


Figure 2.5: Schematic of the DRAGON pumping system illustrating the gas recirculation. © TRIUMF, 2002, by permission.

The pumping system is shown in Figure 2.5. Gas is recirculated through a zeolite trap, cooled via liquid nitrogen, which cleans and stabilizes the pressure in the cell to better than 1 % [76]. Three stages of roots blowers circulate the gas from the target through the trap. Turbo pumps located just outside the target box area collect any gas escaping the cell and also recirculate the gas through the target cell. With the 6 and 8 mm entrance and exit apertures these turbo pumps reduce the pressure to $< 3 \times 10^{-6}$ Torr near the edges of the pumping system.

2.2.2 The BGO Array

Surrounding the gas target is an array of 30 BGO (Bismuth Germanate Oxide) scintillators coupled to Photo Multiplier Tubes (PMT). The array is shown in Figure 2.6. The hexagonal shape allows the scintillators to be packed in a close configuration for maximum efficiency. BGO was selected due to its short radiation length, leading to high efficiency. It was also selected for its decent timing characteristics and low cost. Perhaps the most powerful aspect of the array is the background suppression it contributes. Depending on the background rate a gamma ray detected in coincidence with an end detector event allows an additional suppression factor of up to 10^4 [76]. Depending on the beam energy and tune, the 6 mm entrance aperture allows large transmission. However a small portion of the beam still gets deposited around the gas cell box entrance aperture. This leads to a background of 511 keV gammas from the positron emission of the beam, which can masquerade as good gamma events. These can be suppressed by increasing the hardware threshold. However the gamma decay scheme of the excited nucleus may limit the use of very high discriminator thresholds. The array must also provide good energy resolution in order to separate the good gamma events from background. Decay schemes are not always well known and a measure of the gamma energies provides useful nuclear structure information. DRAGON was used in this manner during a study of the $^{21}\text{Na}(p,\gamma)^{22}\text{Mg}$ reaction [21]. The γ -detector array efficiency and simulation is the topic of another M.Sc. thesis (for more details see [22]).

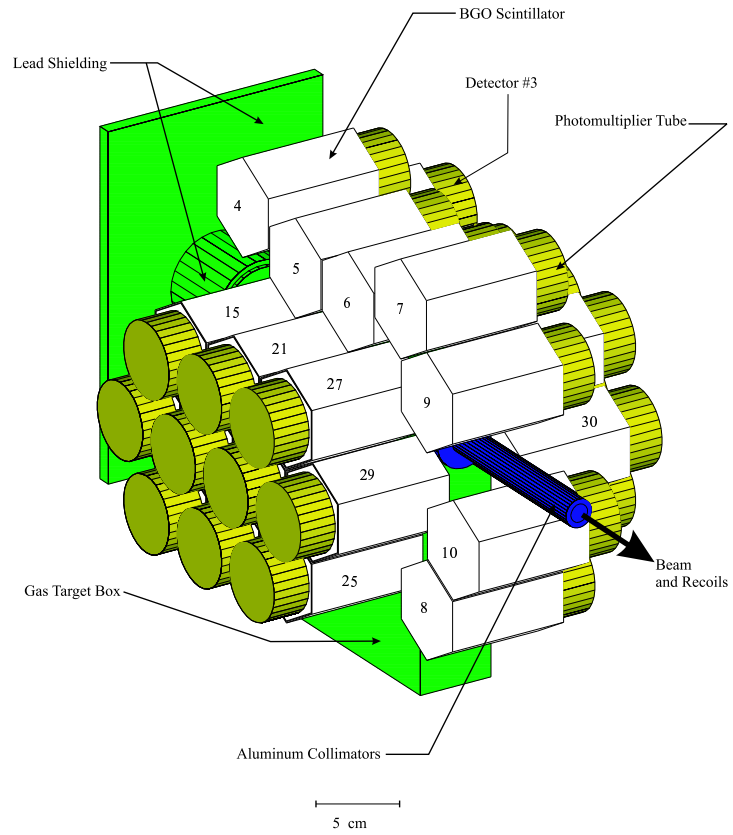


Figure 2.6: DRAGON BGO array surrounding the gas target. © Dario Gigliotti, 2002, by permission.

2.2.3 The Magnetic and Electric Elements

Upon exiting the gas cell the beam and recoils enter the DRAGON EMS. The separator consists of magnetic quadrupoles (Q)[‡], magnetic dipoles (M), magnetic sextupoles (S) and electric dipoles (E) in two stages of mass separation, arranged in the order (QQMSQQQSE) and (QQSMQSEQQ). Beam diagnostic devices such as Faraday cups, slits and beam centering monitors allow small adjustments of the tune to be made, with the use of steerers, all the way along the ≈ 21 m from the target to the final detectors. A CCD camera mounted on MD1 facing the gas cell monitors the ionization of gas allowing centering of the beam through the gas target. It has also recently been used as another measure of beam intensity on target. The first magnetic dipole is equipped with an NMR probe which allows beam energy determination. Well known resonance energies were used to calibrate the NMR [73]. Manipulation of the magnetic, electric and vacuum components are made with the Experimental Physics and Industrial Control System (EPICS). EPICS is a set of software tools which allows real time adjustments to the interfaced equipment. More information about the EPICS software may be found at [26].

The key components of the EMS are the magnetic and electric dipoles. We wish to understand the role of these elements; thus consider the following. Equating the centripetal and Lorentz forces along the bend of the magnetic dipoles we get:

$$\frac{\gamma m v^2}{\rho} = q v B \quad (2.1)$$

where m is the mass, v the velocity, q the charge, ρ the bend radius, B the magnetic field and γ the relativistic correction factor. This leads to:

$$\frac{p}{q} = \rho B \quad (2.2)$$

where p is the momentum. Thus the magnetic dipoles disperse particles according to their momentum to charge ratio. Due to the small velocities of the gas in the target cell, the beam and recoils leave with essentially the same momentum. Thus the first magnetic dipole acts solely to select a particular charge state of beam and recoils. The selection of one particular charge state is one of the biggest efficiency losses. In order

[‡]The second quadrupole was shaped to include a 5 % sextupole component.

to determine the correct yield a measure of the charge state distribution is essential and was the topic of another M.Sc. thesis [23].

Mass separation of beam and recoils occurs due to the electric dipoles. Once again equating the forces involved:

$$\frac{\gamma m v^2}{\rho} = q\mathcal{E} \quad (2.3)$$

where \mathcal{E} is the electric field. This leads to:

$$\frac{pv}{q} = \rho\mathcal{E} \quad (2.4)$$

and for the non-relativistic case:

$$\frac{E}{q} = \frac{\rho\mathcal{E}}{2} \quad (2.5)$$

where E is the kinetic energy. The electric dipoles then disperse in energy over charge. We can rewrite equation 2.4 in terms of the momenta and utilize the fact that the beam particle and the reaction product momentum and charge are virtually identical**.

$$\frac{p_b^2}{q\mathcal{E}} \approx \rho_b m_b \approx \rho_r m_r \approx \frac{p_r^2}{q\mathcal{E}} \quad (2.6)$$

Where the subscripts “ b ” and “ r ” refer to beam and recoils respectively and p is the momentum. Equation 2.6 directly illustrates that the combination of EDs and MDs in DRAGON acts as a mass separator, with the ratio of bending radius of the beam to recoils dependent only on their mass ratio (given a specified charge state). After the first magnetic/electric dipole combination a second stage of mass separation is used in order to reach suppression of the beam on the order of 10^{10} . Some of the properties of the magnetic and electric dipoles are shown in Table 2.2[§].

**The momenta are not identical but very close, and these equation assume non-relativistic kinematics.

[§]Recently both ED1 and ED2 were conditioned up to and just past the designed potentials shown in Table 2.2.

Table 2.2: Properties of the DRAGON Electric and Magnetic Dipoles.

Property	MD1	MD2	ED1	ED2
Bending Radius (cm)	100	81.3	200	250
Bend Angle	50°	75°	20°	35°
Gap (cm)	10	12	10	10
Max Field/Voltage	5.9 kG	8.2 kG	±200 kV	±160 kV
Effective Length (cm)	87.27	106.42	69.81	152.72

2.2.4 End Detectors

In order to reach a final suppression goal of 10^{16} , for the overall DRAGON operation, a detector system was proposed to further reduce the background effects by up to 10^3 . All of the reactions in Table 2.1 have been approved by the TRIUMF EEC and require suppression factors of 3×10^{13} to 1×10^{15} [¶] for a one-to-one ratio of leaky beam to recoils. One other important factor relating to the suppression of DRAGON, is the Q value of a reaction (the energy available for a ground state transition from the excited state). A reaction such as $^{19}\text{Ne}(p,\gamma)^{20}\text{Na}$ has a low excited state of 2.6 MeV, and there exists a dearth of information about the decay scheme of the level of astrophysical importance [24]. If the decay runs through a few levels, the background from pileup of 511 keV γ -rays may significantly reduce the BGO suppression.

DSSSD

A Double Sided Silicon Strip Detector (DSSSD) was used as the sole end detector in the successful measurement of the $^{21}\text{Na}(p,\gamma)^{22}\text{Mg}$ reaction rate, under nova temperature conditions [25]. This detector provides 2-d position measurement along with excellent intrinsic energy resolution ($< 1\%$ FWHM) and decent timing resolution (≈ 1.2 ns FWHM) [80]. The detector consists of 16x16 3 mm wide segmented strips on a silicon wafer. The DSSSD is mounted in its own vacuum box and fits in place of the

[¶]The role of the $^{15}\text{O}(\alpha,\gamma)^{19}\text{Ne}$ reaction as a breakout path from the hot CNO cycle to the rp-process has recently become less important. However its study is still being pursued with backup priority.

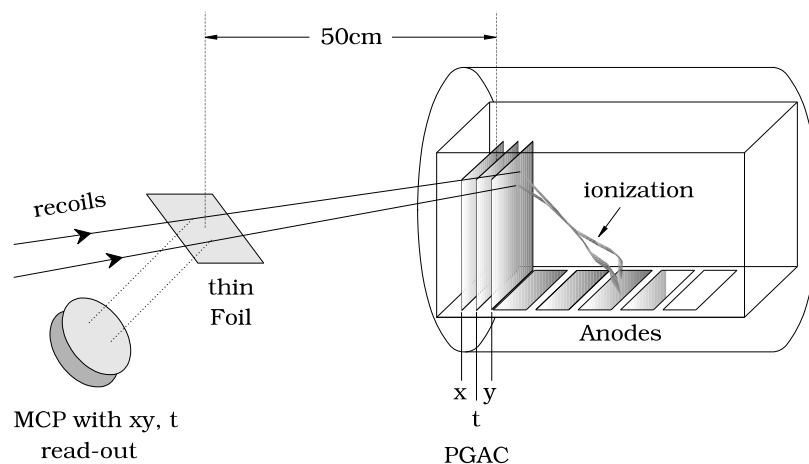


Figure 2.7: Originally proposed detection system for DRAGON. Energy loss along each anode is indicated by the lines above them. © TRIUMF, 2001, by permission.

ion chamber shown in Figure 2.3. The study and commissioning of this detector was the topic of another M.Sc. thesis [80].

Further Detection Systems

The original detection system proposed for DRAGON involved two fast timing detectors along with an ion chamber, which provides both Z -discrimination and good energy resolution. The system is shown in Figure 2.7. The commissioning of this detection system is still underway and will provide a powerful recoil-beam separation system for DRAGON.

Ion Chamber

A schematic of the DRAGON ionization chamber is shown in Figure 2.7. Currently it consists of 5 anodes a single cathode and a Frisch grid located just above the anodes. The purpose of the Frisch grid is to shield the anodes from the charge buildup between

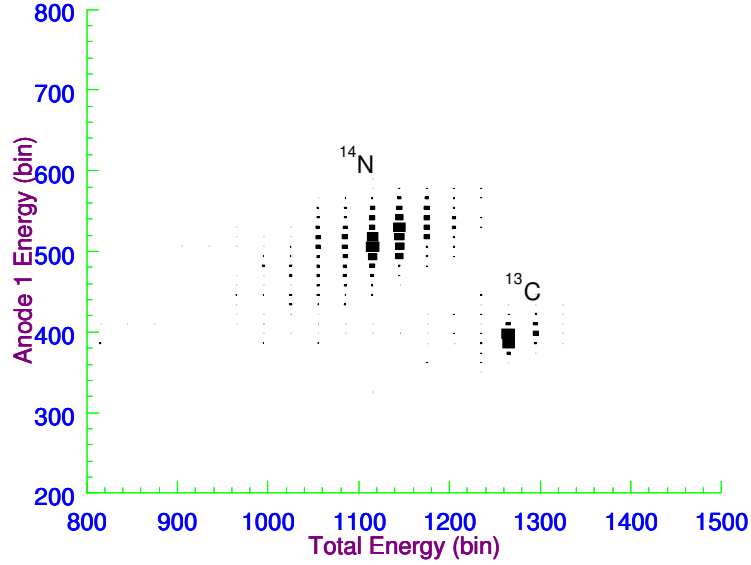


Figure 2.8: $^{13}\text{C}(p,\gamma)^{14}\text{O}$ ionchamber data. Shown is the energy collected in anode1 versus the total energy collected.

the Frish grid and the cathode. Since it is a Bragg counter an ionization chamber performs separation on the basis of the proton number of the particle, Z .

The properties of the ionchamber have been studied in a few heavy ion reactions, for example $^{13}\text{C}(p,\gamma)^{14}\text{O}$, $^{16}\text{O}(\alpha,\gamma)^{20}\text{Ne}$ and most recently $^{26}\text{Mg}(p,\gamma)^{27}\text{Si}$. It has shown to provide respectable discrimination. This can be seen from data of the $^{13}\text{C}(p,\gamma)^{14}\text{O}$ reaction at $E_{lab} = 650$ keV/u shown in Figure 2.8. The data shown result from the overlay of the data sets from two different runs. One with attenuated ^{13}C into the IC, and the second with DRAGON tuned for ^{14}N . All other run conditions were the same for these two runs. However this discrimination is largely dependent on the energy of the beam. Energy resolution on the order of 1% and Z -discrimination $Z/\Delta Z = 47$ with ^{28}Si at 1.5 MeV/u have been measured elsewhere [28]. Such resolving power may not be possible at lower beam energies.

Parallel Grid Avalanche Counter

As illustrated in Figure 2.7 the Parallel Grid Avalanche Counter (PGAC) consists of three parallel planes: two cathodes and a central anode. The planes consist of a grid of wires of $50\text{ }\mu\text{m}$ diameter with 1 mm pitch. The two cathode planes are oriented perpendicular such that 2-d position information may be extracted. The timing signal is picked up from the anode. Also, as shown in Figure 2.7, the PGAC is operated in the front of the ion chamber, which is filled with isobutane gas at a pressure of typically 4-20 Torr.

Charged particles enter the ion chamber through a thin window and ionize the gas near its trajectory. Liberated electrons from the ionized gas molecules are accelerated toward the anode, and the positively charged ions are accelerated toward the cathodes. Strong electric fields between the planes and near the wires accelerate the electrons, and these electrons may produce further ionization and an avalanche process occurs. The collected charge at the anode induces a positive charge on the cathode wire planes. A charge collecting preamplifier can convert the signal at the anode into a measurable pulse. Position signals are determined by the use of delay lines between each wire along the cathode grids.

Timing properties of the PGAC have been studied elsewhere, Fabris et al. [71] report a time resolution of 200 - 300 ps using fission fragments, with a wire grid density of 45 lines per inch (LPI). Using 25 LPI, our current setup, [71] finds a time resolution of 400 ps. Currently the PGAC has undergone bench tests, but further commissioning is required.

MCP Detection System

A microchannel plate is a detector which can be used in fast timing applications. A sketch of the MCP detection system is shown in Figure 2.9. Beam and recoils lose energy through a thin carbon foil ($20\text{ }\mu\text{g}/\text{cm}^2$) and pass through the electrostatic mirror. Secondary electrons escape the foil and are accelerated by the first grid. After passing through grid 2 they are deflected toward the MCP where they are detected. The study of this detection system was the subject of this thesis, the goal of which was to commission the system and provide the first studies of a local time-of-flight

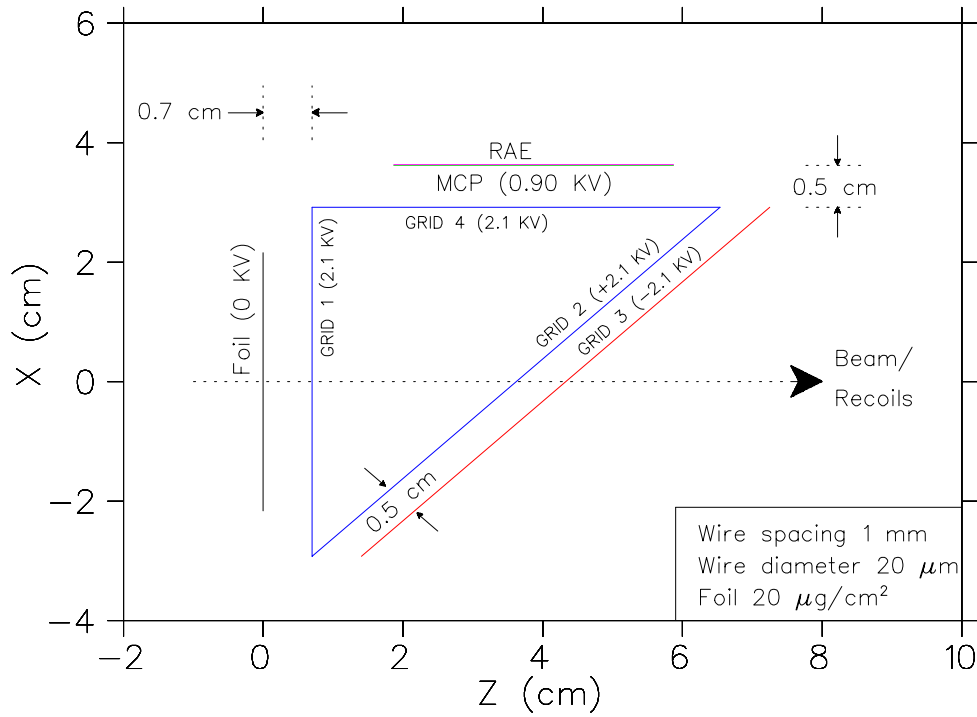


Figure 2.9: Schematic diagram of the current MCP detection system. Heavy ions knock out low energy electrons from a thin foil which are accelerated and deflected on the MCP. The heavy ion continues along its original trajectory to be detected downstream.

measurement for mass separation. More detailed discussion follows.

CHAPTER 3

The Microchannel Plate System

A Microchannel plate is an amplifier of electrons and can be used to detect charged particles as well as some types of radiation. MCPs consist of a 2d array of millions of small diameter ($\approx 10 \mu\text{m}$) glass capillaries. The operating principle of an MCP is shown in Figure 3.1. The channel walls are coated with a semiconductive layer in which the bias current flows and allows electron replenishment. Incident radiation with sufficient energy ionizes the atoms in the channel walls. The knocked out electrons then escape as low energy secondary electrons. The bias is set up such that the electrons are then accelerated toward the back side of the channel. Due to the small transverse velocities of the secondary electrons along with the bias the paths through the channel are parabolic. If the bias along the channel is adequate the energy of these electrons will be large enough to knock out further electrons and an avalanche process ensues. The channel walls then act as a continuous dynode for the avalanche process.

The use of microchannel plates as image intensifiers has become ubiquitous. For example MCPs are used in night vision goggles and are considered to have been one of the major breakthroughs in night vision research [34]. The high resolution camera on the Chandra x-ray observatory also utilizes an MCP for x-ray imaging [31]. Other areas of physics research in which MCPs are used as detectors of radiation or charged particles are: beta-radiography [35], magnetospheric research [36], fundamental symmetry tests of the standard model [37] and nucleosynthesis research (i.e. this paper).

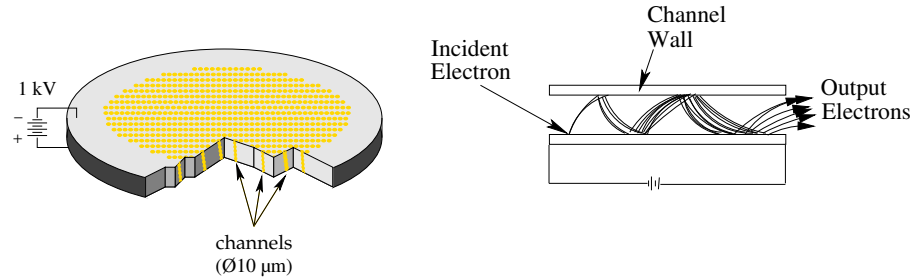


Figure 3.1: Schematic operating principle of an MCP. Input radiation initiates the avalanche process.

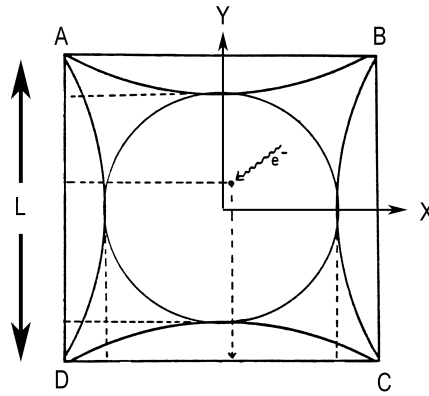


Figure 3.2: Schematic diagram of the arc shaped RAE. Also shown is the circular projection of the MCP.

3.1 Resistive Anode Encoder

By themselves MCPs offer no position measurement beyond the dimensions of the detector. Generally a Resistive Anode Encoder (RAE) is used to obtain 2-d position information. The shape of the encoder is of particular interest and is illustrated in Figure 3.2. It resulted from a suggestion by C.W. Gear [38]. The geometry suggests theoretically distortionless encoding of 2-d coordinates. Gear pointed out that a circular hole of radius b has no effect on the current flow through an infinite sheet having resistivity r , if the hole is bordered by a line resistor of value $R=r/b$.

The position can be determined if we assume the anode is square, this is allowed since the shape of the anode is such that it mimics the current flow through a square sheet of length L and uniform resistivity. In this case the charge received at each corner is then related to the area between the respective corner and the point of the voltage pulse V :

$$I_a = \frac{V}{r(\frac{L}{2} + x)(\frac{L}{2} - y)} \quad (3.1)$$

$$I_b = \frac{V}{r(\frac{L}{2} - x)(\frac{L}{2} - y)} \quad (3.2)$$

$$I_c = \frac{V}{r(\frac{L}{2} - x)(\frac{L}{2} + y)} \quad (3.3)$$

$$I_d = \frac{V}{r(\frac{L}{2} + x)(\frac{L}{2} + y)} \quad (3.4)$$

where as mentioned previously r is the sheet resistivity, and L as shown in Figure 3.2 is the non-diagonal length from corner to corner, and the currents (a , b , c and d) correspond to those shown in Figure 3.2. We have also neglected any input impedance from amplifiers or whatever electronics are used during signal processing. One can solve these equations for x and y :

$$x = \frac{L}{2} \frac{(I_b + I_c) - (I_a + I_d)}{I_a + I_b + I_c + I_d} \quad (3.5)$$

$$y = \frac{L}{2} \frac{(I_a + I_b) - (I_c + I_d)}{I_a + I_b + I_c + I_d} \quad (3.6)$$

These equations were used during the analysis of the commissioning of the MCP /RAE.

3.2 The DRAGON Microchannel Plate

The DRAGON microchannel plate was purchased from Quantar Technology Inc. [42] in June of 1999. It is a 3394A MCP/RAE sensor. The detector consists of two microchannel plates in the well known chevron configuration. Generally we will refer to the MCPs in a singular manner where the plural is understood. Figure 3.3 illustrates

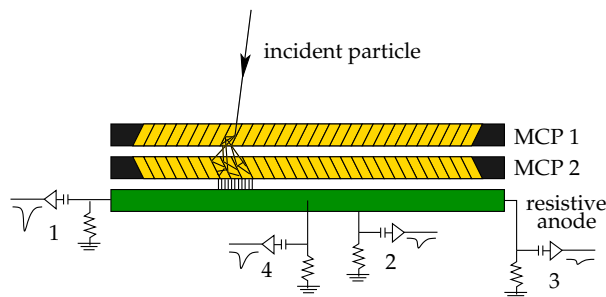


Figure 3.3: Side view of a chevron configuration of a microchannel plate detection system with an anode for position sensitivity.

the chevron configuration. It consists of two MCPs stacked one behind the other. Generally MCPs are produced such that the glass capillaries are set at some angle to the front or back face of the MCP. This angle is chosen with several factors in mind [43]; detection efficiency, prevention of incident particles from passing through the channels with no interaction, spatial resolution and positive ion trap efficiency when two or more MCPs are used. The angle of the MCPs used for DRAGON is 8° . Microchannel plates are operated under vacuum conditions, $< 10^{-6}$ Torr, and should be kept under vacuum while not in use; non vacuum conditions may be pernicious.

The chevron configuration has the advantage of increased gain and reduction of noise due to positive ion feedback. That is residual gas in the glass capillaries could get ionized and accelerated toward the front face of the MCP. This would lead to the production of a second pulse, if the ionized molecules accelerated along the electric field had enough energy to produce secondary electrons from the channel walls. The density of the cloud of electrons is greatest near the output end of the MCP and this is where the greatest threat of ionization occurs. The stacked configuration of the chevron reduces this noise due to absorption at the junction of the plates. Some of the properties of the MCP system are shown in Table 3.1. Detailed schematics of the mirror grid planes are given in appendix A.

Table 3.1: Selected properties of the DRAGON MCP detection setup.

Property	Dimensions
channel diameter	10 μm
center-to-center distance	12 μm
active diameter	40 mm
open area ratio	63 %
foil thickness	20 $\mu\text{g}/\text{cm}^2$
mirror wires	20 μm diameter gold plated tungsten

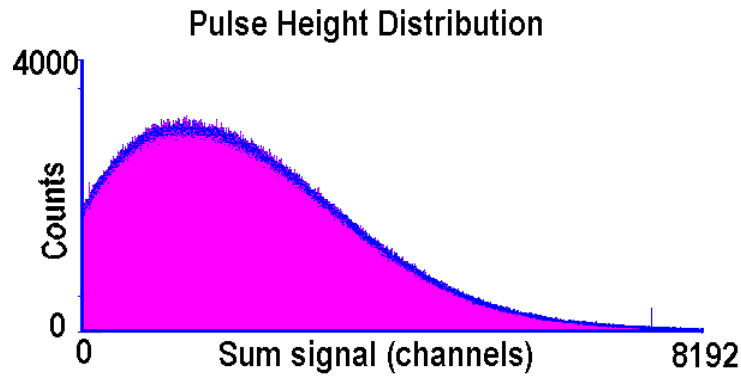


Figure 3.4: Pulse height distribution of the DRAGON microchannel plate.

3.2.1 Gain and Pulse Height Distribution

The pulse height distribution of the DRAGON microchannel plate, and microchannel plates in a chevron configuration in general, is shown in Figure 3.4. The pulse height distribution has a direct effect on the efficiency of the MCP. That is high thresholds may cut out good events; whereas low thresholds may allow noise to sneak in.

3.2.2 Dark Current

According to [43] the dark current from MCPs arises from four factors: thermionic and electric field emission from the channel walls, the ionization of residual gases, local discharge by a high electric field and the photoelectron emission by photons produced

in electric field scintillation of the MCP supporters. Noise has been known to be reduced by cooling. The intensity of the electric field can be reduced by increasing the channel diameter and increasing the length d , while keeping the gain constant. A typical MCP shows a dark count rate of less than 3 cps/cm². However this is not a problem for the DRAGON setup since any local time-of-flight measurement requires the coincidence of two detectors and such a dark current will be insignificant. At the current threshold the background rate is ≈ 1 cps.

3.2.3 The Detection System

The detection system is shown in Figure 3.5. In this view beam and recoil ions travel nearly out of the page. The front face of the first MCP is also visible as shown. The foil rests on its own motor drive and is not shown here but in the vacuum box would reside just behind the assembly as it is shown here. The active diameter of the MCP is 40 mm, and typical biases are in the range 910-950 volts. The motor drive is controlled via the EPICS system allowing the MCP or the final Faraday cup to be inserted.

The carbon foils are supplied by ACF metals [45]. Natural carbon is arc deposited onto 50 mm x 70 mm glass slides with a parting agent such as a detergent to allow ease of removal by floating. The supplier quotes a uniformity of 10 % or better across the foil. The self supporting foils are floated off the slides and mounted on foil holders. Currently the diameter of the foils used is 25.4 mm.

The voltage divider network is shown in Figure 3.6. The HV_{in} is supplied by a PS350 model Stanford Research Systems power supply [44]. It has a 0.001 % regulation rating. The timing out signal is derived from the back of the second MCP and is the result of a dip in voltage from the electron multiplication. The signal itself is actually a result of the recharge signal from the power supply. If the large resistance of the MCPs is neglected (typically 100-1000 M Ω), it is easy to see that the bias across each MCP is given by:

$$V_{MCP} = \left(\frac{2.1 \text{ M}\Omega}{6.8 \text{ M}\Omega} \right) HV_{in} \quad (3.7)$$

Typically HV_{in} ranges between 2960 to 3060, meaning that each MCP operates

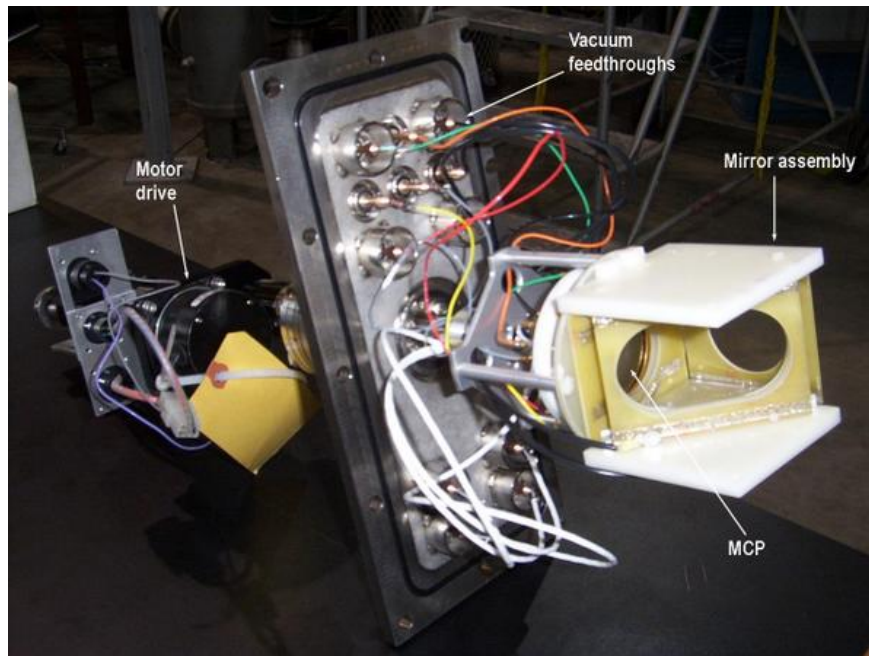


Figure 3.5: Photo of the DRAGON Microchannel Plate detection system.

with a potential of 910 - 950 V.

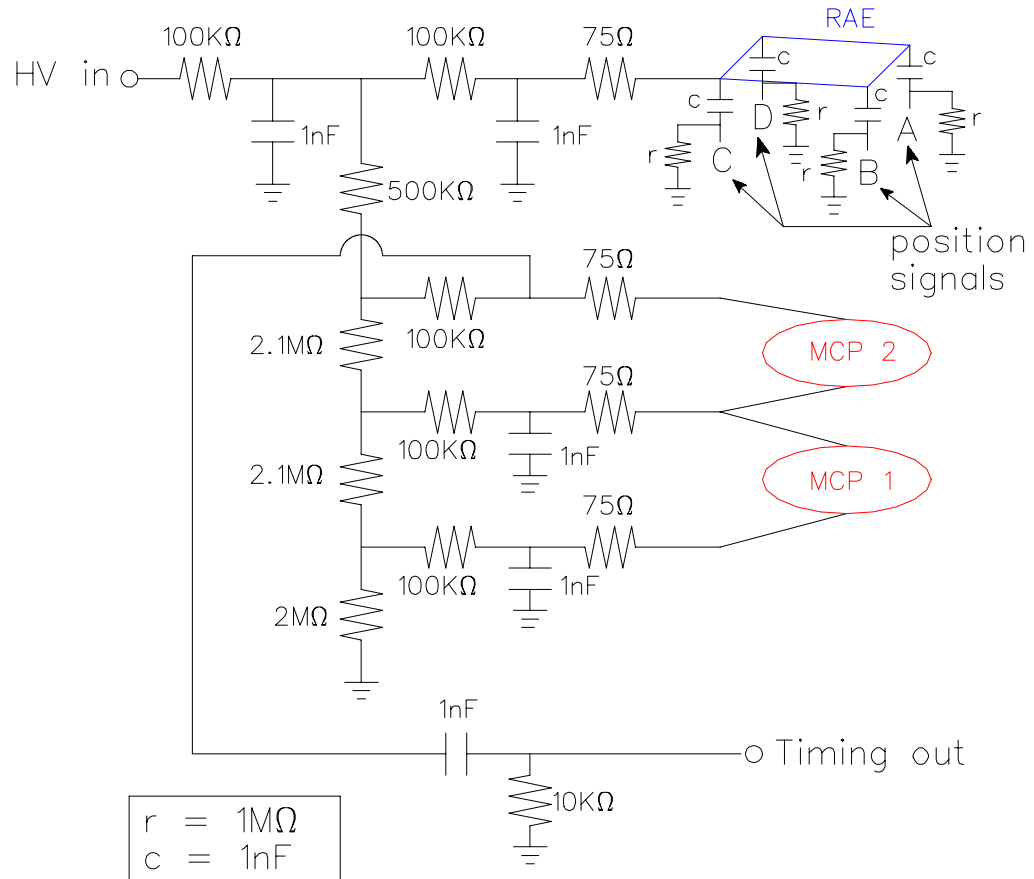


Figure 3.6: Schematic of the electronics of the MCP-RAE system. The HV_{in} is supplied by a Stanford Research Systems PS350 model power supply.

CHAPTER 4

The Detection System Simulation

A simulation designed to track the electrons from the carbon foil to the MCP through the electrostatic mirror was written in 2001 at TRIUMF[†]. Laplace's equation for the electrostatic potential was solved using a program written at TRIUMF called RELAX3D [46]. The program expects one to break up the system into an array of grid points. The boundary conditions, Dirichlet in our case, are then set to a fixed potential at the desired grid points by a user-written subroutine. The program then uses the relaxation technique to satisfy a set of finite difference equations.

The approximation used by the relaxation technique involves a difference equation relating neighboring points rather than a differential equation. In a cartesian coordinate system RELAX3D uses the second order approximation:

$$\frac{\partial^2 V}{\partial x^2}(i, j, k) \approx \frac{V_{i-1,j,k} + V_{i+1,j,k} - 2V_{i,j,k}}{h_x^2} \quad (4.1)$$

where $V_{i,j,k}$ is the potential at grid location (i,j,k) , h_x is the grid spacing in the x direction and the same approximation is made in the y and z directions. The general differential finite-difference approximation to the differential equation then has the form:

$$F_{i,j,k} = \frac{V_{i-1,j,k} + V_{i+1,j,k} - 2V_{i,j,k}}{h_x^2} + \frac{V_{i,j-1,k} + V_{i,j+1,k} - 2V_{i,j,k}}{h_y^2} + \frac{V_{i,j,k-1} + V_{i,j,k+1} - 2V_{i,j,k}}{h_z^2} \quad (4.2)$$

[†]The code was written by Larry Root.

in our case the problem is simplified since $h_x = h_y = h_z = h$, for a 2-dimensional system we find after rearranging:

$$V_{i,j} = \frac{1}{4}(V_{i-1,j} + V_{i+1,j} + V_{i,j-1} + V_{i,j+1}) - \frac{h^2 F_{i,j}}{4} \quad (4.3)$$

with $F_{i,j}$ the corresponding two dimensional analog to equation 4.2, which in the absence of charge is zero. The relaxation method assigns a new value to the grid point given by Equation 4.4.

$$V'_{i,j} = \frac{1}{4}(V_{i-1,j} + V_{i+1,j} + V_{i,j-1} + V_{i,j+1}) \quad (4.4)$$

The process of reassigning potentials is then done in an iterative manner until the desired residuals are reached. That is we monitor the change $V'_{i,j} - V_{i,j}$. RELAX3D allows one to set a tolerance such that once the largest residual is smaller than the tolerance a solution is reached and the iteration process is halted. The grid is said to be fully relaxed when potentials from one iteration to another no longer change. Methods increasing the speed of convergence exist; for example see Reference [47].

The MCP is shifted from the central part of its adjacent grid due to the small shift that the electrons experience as they traverse the mirror. It is straight forward to show that this shift is given by:

$$\Delta x = d\sqrt{2} \frac{|V_p|}{|V_n| + V_p} \quad (4.5)$$

where V_n is the negative mirror potential, V_p is the positive mirror potential and d is the distance between the positive and negative grids. In our case $d = 0.5$ cm and $|V_n| = V_p = 2100$ V. This leads to $\Delta x = 3.5$ mm. Our current design actually allows a 2.5 mm shift, thus in the current setup we are losing 1 mm of the active diameter of the MCP. However this does not pose a large problem since the largest foil diameter used is 25.4 mm.

The grid wires of the MCP mirror are $20 \mu\text{m}$ in diameter. The mesh approximation to this diameter is shown in Figure 4.1. A second approximation was the distance between the wires along the 45° wire planes. The simulation used a 1.004091 mm spacing rather than the true 1 mm spacing. This however is a small effect. The grid consisted of just over 94 Million mesh points. A contour plot of the potentials is shown

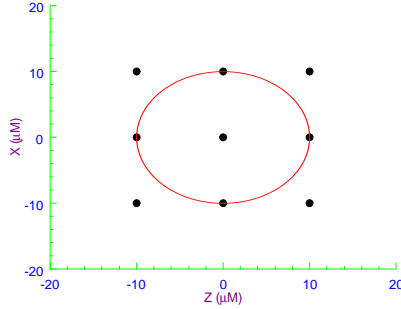


Figure 4.1: Mesh approximation of a 20 μm wire with a 3x3 grid.

in Figure 4.2, and Figure 4.3 shows a blowup of the contours around two of the wires on the first grid. One of the major problems was the question of the convergence of a solution with the relaxation method using such a large number of points. In order to encourage convergence we inserted an inner triangle filled with boundary points inside the triangular portion of the mirror at a bias of +2.1 kV. These inner triangle points reduced the number of grid points by over 8 million and helped set up the field free region within the +2.1 kV triangle. This triangle was set up 0.5 cm inside the “real” wire planes such that it would not affect the true potentials around the wire. The wires were 3 mesh points wide while this 0.5 cm corresponds to 500 mesh points, so we felt confident this inner triangle would introduce no ill effects. Over 80,000 sweeps through the entire mesh were done before arriving at these contour plots. A couple of features which look good are the symmetry and smoothness shown in Figure 4.3. Contours such as those around the wires were checked following 5,000 sweep sequences and by the end only very small changes in the contours reaching between the wire planes, such as contour 7 in Figure 4.3, could be seen. The closed contours around the wires seemed to have converged, or were extremely close to convergence. Thus there exists the question about how much of a systematic effect this would introduce into our simulation. In the end we assigned a 5 % systematic error based on the above checks after 5000 sweep intervals.

The initial conditions are shown in Figure 4.4. The secondary electron angular distribution is known to be well represented as a cosine function. This is accomplished by the flat θ and cosine ϕ distribution shown. The secondary electron energy

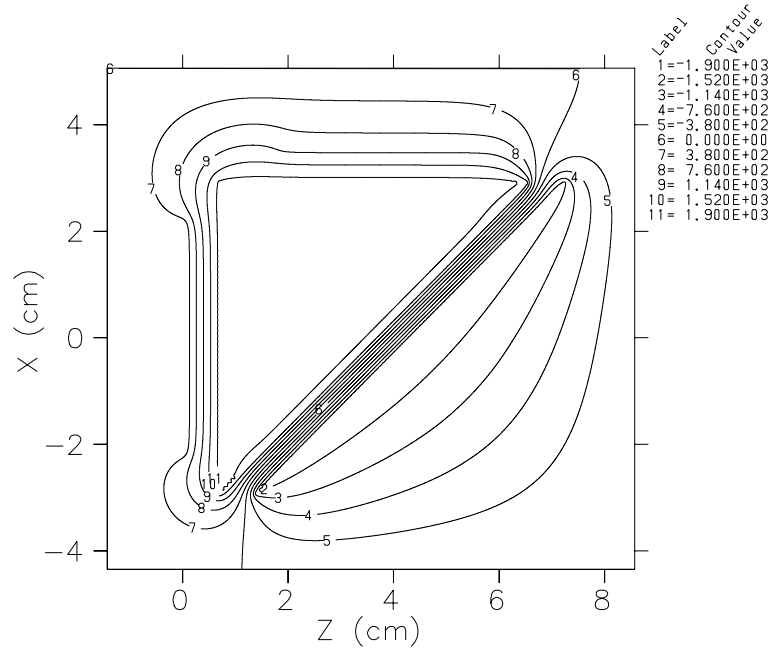


Figure 4.2: A plot of contours around the DRAGON MCP mirror setup solved using RELAX3D. These should be compared to Figure 2.9.

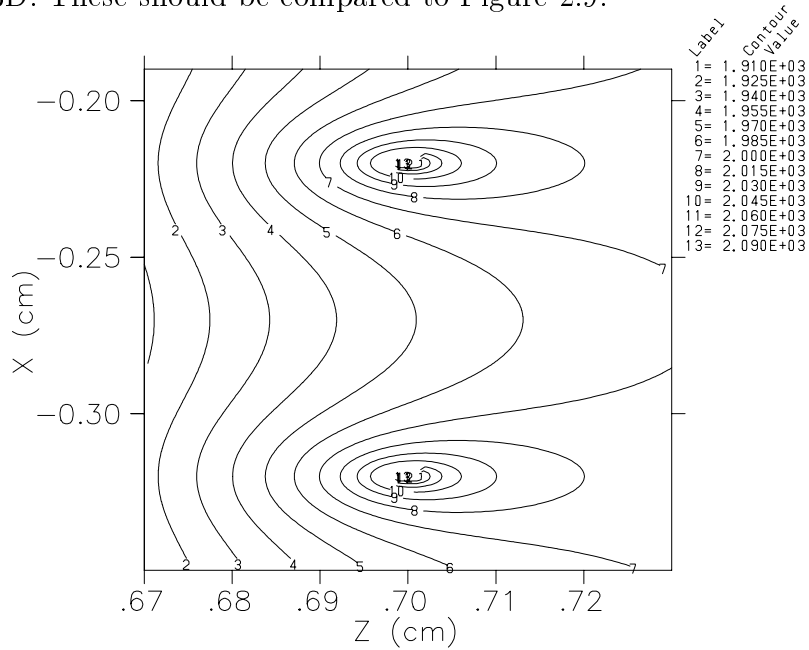


Figure 4.3: A close up of the contours around two wires of the first grid.

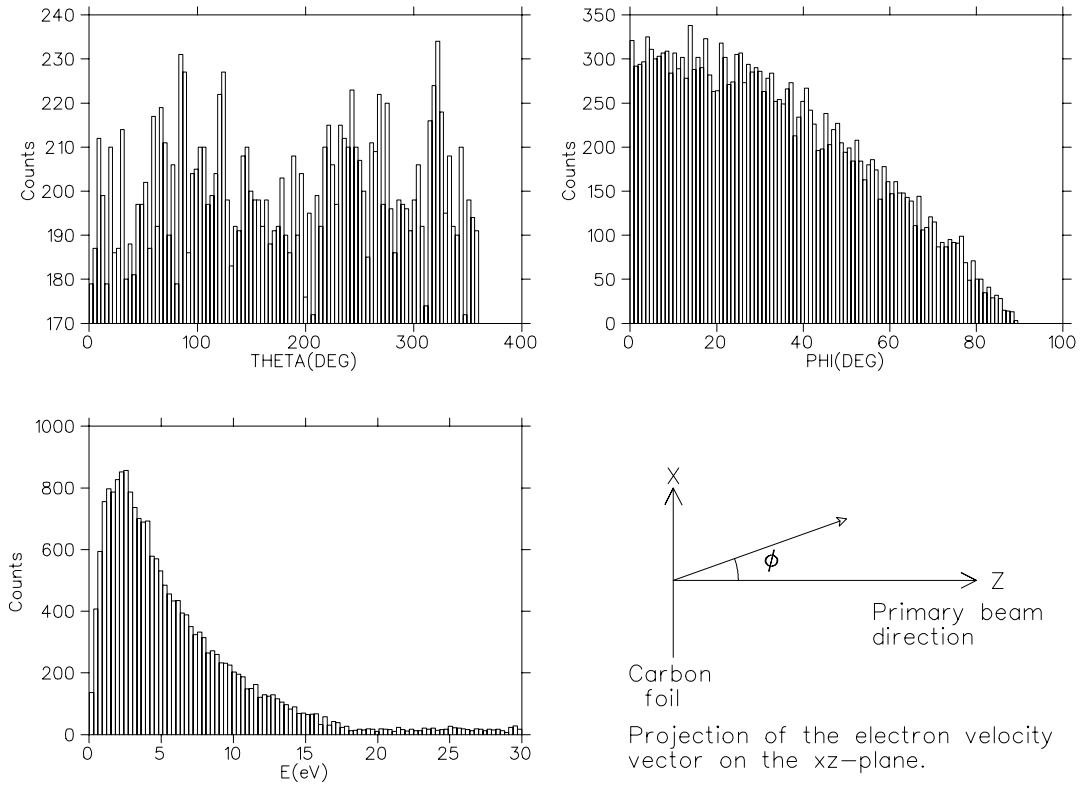


Figure 4.4: Theta, phi and energy distributions of 20000 electrons started at the carbon foil. Also shown is the definition of phi, similarly θ is the angle between the x-axis and the projection of the electron velocity vector onto the xy-plane.

distribution is given by Rothard et al. [81].

The output of the RELAX3D solved potentials were read into an electron tracking program written in FORTRAN. The relativistic equations of motion, equation 4.6, of the electron to be solved are given by Landau and Lifshitz [82].

$$\frac{d\mathbf{P}}{dt} = e \left[\mathbf{E} + \frac{\mathbf{v}}{c} \times \mathbf{B} \right] \quad (4.6)$$

where e is the charge, \mathbf{v} the velocity, \mathbf{P} the momentum, \mathbf{E} the electric field, \mathbf{B} the magnetic field and all bold face characters are vectors. This implies that the acceleration of a charged particle in an electric and magnetic field is:

$$\frac{d^2\mathbf{x}}{dt^2} = \frac{e}{mc^2} \sqrt{1 - \frac{v^2}{c^2}} \left[c^2 \mathbf{E} + c \mathbf{v} \times \mathbf{B} - \mathbf{v}(\mathbf{v} \cdot \mathbf{E}) \right] \quad (4.7)$$

In our case no magnetic field elements were used which simplified the equations to be solved. Runge-Kutta integration was used to track the electrons through the RELAX3D solved mesh. Integration step sizes one tenth the size of the mesh spacing were used, thus interpolation along the grid was necessary. The tracking technique is best illustrated with the use of Figure 4.5. The points shown in black are a small 3x3 subsection of the mesh points solved with RELAX3D, whose potentials are known. If the current Runge-Kutta step is given by the red point, in the Figure, the 2-d derivatives are required at the point. Numerical interpolation along the grid is done to produce the blue points shown. Numerical interpolation is then done again to produce the potential at the red point (current integration position). Numerical differentiation is done along the blue points to solve for the slope at the red point. As we step along the grid the 3 x 3 mesh points used for the interpolation and differentiation are also changed until the electron hits a wire or the MCP.

Numerical interpolation across the grid points is performed on a grid containing the neighbors of a particular point. Quadratic interpolation was done using Newton's interpolation formula. If the grid of points are given by x and y coordinates then the k^{th} point is determined as:

$$y_k = y_0 + \frac{x_k - x_0}{\delta} \Delta y_0 + \frac{(x_k - x_0)(x_k - x_0 - \delta)}{2} \Delta^2 y_0 \quad (4.8)$$



Figure 4.5: Schematic illustrating the electron tracking method, using numerical interpolation and differentiation.

where $\Delta y_0 = y_1 - y_0$ and δ is the step size in the x direction.

The numerical differentiation is also done using a second order polynomial.

$$y'_k = \frac{1}{\delta}(\Delta y_0 - \frac{1}{2}\Delta^2 y_0) \quad (4.9)$$

Given the above definition of Δy_0 we can see that the $\Delta^2 y_0$ term is given by $\Delta^2 y_0 = y_2 - 2y_1 + y_0$. Fourth order Runge-Kutta integration is then performed which involves a global error of $\mathcal{O}(h^4)$, where h is the integration step size. The method uses the so called classical Runge-Kutta algorithm to solve the equation:

$$\frac{dy}{dx} = f(x, y) \quad (4.10)$$

The algorithm is as follows:

$$\begin{aligned} a &= hf(x_n, y_n) \\ b &= hf(x_n + h/2, y_n + a/2) \\ c &= hf(x_n + h/2, y_n + b/2) \\ d &= hf(x_n + h, y_n + c) \\ y_{n+1} &= y_n + \frac{1}{6}(a + 2b + 2c + d) \end{aligned} \quad (4.11)$$

where n is the n^{th} point along the algorithm. We use the slope at the starting point (x_n, y_n) to predict the value of y at the midpoint $x_n + h/2$. We then calculate the slope at this estimated midpoint and use it to get a better estimate of the slope at the midpoint. This slope is then used to predict a value at $x_n + h$, and a fourth estimate of the slope is calculated at this point. All four estimates of the slope are then used as shown in the final line of equation 4.11, for the final estimate at y_{n+1} .

4.1 Secondary Electrons

A key role is played by the process of secondary electron production. Therefore before we proceed any further it is imperative to discuss a few of the general features of secondary electrons. Generally secondary electrons are produced whenever ionizing radiation interacts with matter. Three properties of the secondary electrons are important, namely the number produced, their energy and their angular distribution. These properties have important effects on the MCP efficiency and the observed position resolution. It has been known for some time that a cosine distribution represents the angular distribution of secondary electrons very well [83, 84]. This distribution was used in the simulation.

Primary radiation liberates valence electrons from the target material. The escape of these electrons is determined by the amount of scattering they undergo before reaching the surface, and the work function of the material. For metals the escape depth may be on the order 5 nm while for insulators a typical number is 50 nm. Free electrons are then swept away by the field between the foil and the first wire grid and collected by the MCP.

The total number of secondary electrons emitted has a direct effect on the efficiency, and as we will soon see, the position resolution and linearity. The forward emitted electron distribution has been studied by References [85] and [86]. There exists a direct relationship between the number of secondary electrons, the stopping power (dE/dx) of the carbon foil, and the charged particle producing the ionization. Generally the constant Λ is used to relate the number of secondaries to the stopping power by:

$$\Lambda = \frac{Y}{dE/dx} \quad (4.12)$$

where Y is the total number of liberated electrons, forward and backward. Rothard et al. [85] give this experimentally determined constant and produce a formula for the number of secondary electrons emitted in the forward direction:

$$\gamma_f = 0.17C_f dE/dx \quad (4.13)$$

where γ_f is the average number of secondary electrons emitted per incoming projectile in the forward direction, C_f for heavy ions is 0.5 and dE/dx is measured in units of eV/Å.

Equation 4.13 is good to within a factor of 2 according to Rothard. Shi et al. [86] have also reported the yield of secondary electrons for heavy charged ions ($^{16}O^{3+}$, $^{19}F^{3+}$ and $^{35}Cl^{3+}$) and their results agree very well with equation 4.13. For example in the case of ^{16}O Shi et al. report a Λ of $6.97 \mu g/cm^2/keV$, compared to $7 \mu g/cm^2/keV$ reported by Rothard et al.

A typical example of relevance to DRAGON would be ^{21}Ne at 300 keV/u, in which case we use the Stopping and Range of Ions in Matter (SRIM) [75] to get an estimate of the stopping power in a carbon foil. SRIM performs a Monte Carlo simulation of the energy loss through the foil and provides the stopping power. SRIM gives 276.2 eV/Å, resulting in an average number of secondaries of 23.5.

CHAPTER 5

Testing of the DRAGON MCP

Three characteristics of the MCP needed to be understood before it could be used in an experimental setup: the timing resolution, the efficiency and the position resolution. The timing is important since in a local time of flight one desires the best timing possible. The efficiency must be well understood so that one may correct for any losses, which can then be added in with other losses along DRAGON [74]. The position resolution is useful when the MCP is to be used in conjunction with the PGAC/IC setup as described earlier. It may allow suppression relating to the difference in position in the dispersion direction at the end of DRAGON.

5.1 Timing

Microchannel plates are known to have excellent timing properties; for example see References [55]-[67]. As previously mentioned, the original goal of the end detection system was to achieve additional leaky beam suppression. One of these methods involved the use of two fast timing detectors in a local time-of-flight approach at the end of DRAGON. In general it is hard to state the required timing resolution. The time spread between beam and recoils depends on the particular experiment since it depends on the mass, the Q-value and gamma branching of the reaction. The kick given to the fused product by the emitted γ -ray influences the final energy of the recoil and therefore the local time-of-flight at the end of DRAGON. The required timing will be discussed later in the chapter.

5.1.1 The Photomultiplier and Scintillator

Microchannel plates are intrinsically fast detectors, thus, in order to test the MCP a second fast detector was needed. Photomultiplier tubes, PMTs, are known to be fast detectors and have been used for many years [48]. Two designs were used; one for the ^{68}Ge studies and the second, for the ^{148}Gd alpha source and ^{21}Ne beam tests. In both cases a Bicron BC-418 plastic scintillator, of 0.25" thickness, was used in conjunction with a Philips 12 stage XP 2262B photomultiplier tube. Both were chosen for their fast timing characteristics: Bicron quotes a rise time of 500 ps associated with the scintillator, while the PMT had a quoted ≈ 2 ns rise time. In fact in all the tests to be described the measured rise time was 2 - 2.5 ns, part of which was a result of the limited bandwidth of the oscilloscope. Leo [53] provides an estimate of the rise time due to the limited bandwidth of the scope. If we take this into account our signal rise times were in the range 1.8 - 2.3 ns. While the diameter of the face of the PMT is closer to 2", the diameter of the scintillator used was 1". This was done at the cost of a loss in efficiency to minimize any possible time straggling near the edges of the PMT [49]. Also in both cases a light guide was not used. The scintillator resembled a small hockey puck and will be referred to hereafter as such.

The first studies were conducted with the use of a ^{68}Ge source, which involved the detection of 511 keV annihilation photons. The construction of the puck/PMT involved the use of teflon tape backed by aluminized mylar whose purpose was to reflect light into the PMT. Between the scintillator and the PMT face, optical grease was used to facilitate 100 % transmission. The puck was held in place on the PMT by a cap which could be twisted on. The cap was made out a black plastic in order to minimize light transfer from the black plastic to the puck.

The alpha source and beam tests involved mounting the PMT on the end of DRAGON. Thus a combination puck holder and Marman flange was built. In this case the puck was bare to any radiation. Together the teflon tape and aluminized Mylar would have produced unwanted straggling. This is particularly true of the teflon tape since it would have been difficult to produce a uniformly thick layer.

5.1.2 Work Station, Electronics and Time Calibration

A series of off-line studies were conducted with the use of a Time to Amplitude Converter (TAC) and a Multi Channel Analyzer (MCA) as the data collection system. The MCA was the Nucleus personal computer analyzer II. The PCA card consists of a 100 MHz Wilkinson type Analog to Digital Converter (ADC). The memory consists of up to 8192 channels. The integral non-linearity is less than $\pm 0.1\%$ and the differential non-linearity is less than $\pm 1\%$ [50]. Integral nonlinearity is the deviation from ideal linear correspondence between pulse height and channel number. Differential nonlinearity is a measure of the inconstancy in the width of each channel [53]. The data from the computer were saved as an ascii file and read into the appropriate analysis package. A few of the minimum computer requirements were 512K RAM, DOS 3.0, and a hard drive.

Before any tests were done the MCA was calibrated using an ORTEC 462 time calibrator [51]. The time calibrator was adjusted to pulse every 40 ns over a range of 640 ns, and the TAC had a timescale of 500 ns. The resulting calibration is shown in Figure 5.1. The figure is a little deceiving at first since it looks as if each peak contains only one bin. However this is not the case as will be shown below. The errors used for each fit were purely statistical with Poisson weighting in a least squares minimization technique. The data analysis package used was Extrema[†] which was written at TRIUMF [52]. Briefly EXTREMA is a high level software package used for data analysis and visualization. Each peak was fit with the following formula:

$$f(x) = \frac{A}{2} \left[erf\left(\frac{x - x_0 + \frac{\delta}{2}}{\sigma\sqrt{2}}\right) - erf\left(\frac{x - x_0 - \frac{\delta}{2}}{\sigma\sqrt{2}}\right) \right] \quad (5.1)$$

where A is the normalization, x_0 is the mean of the fit, σ is the standard deviation of the distribution, δ is the width of the bins and erf is the error function defined by:

$$erf(x) = \frac{2}{\sqrt{\pi}} \int_0^x e^{-u^2} du \quad (5.2)$$

the meaning of the fit with equation 5.1 then becomes clearer with this definition of the error function. The first error function of equation 5.1 is the integral of a

[†]PHYSICA was also used but is essentially the same package as EXTREMA.

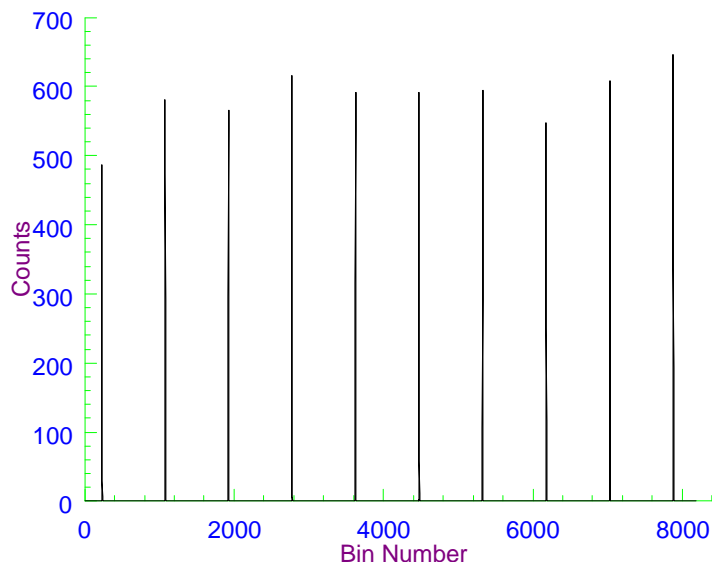


Figure 5.1: Calibration of the MCA scale using an ORTEC 462 Time Calibrator.

Gaussian function from 0 to right most portion of a given bin. The second error function is the integral of a Gaussian to the leftmost portion of a given bin. Thus the difference is just the area under a Gaussian curve (with mean x_0 , normalization A and width σ) within a particular bin. The χ^2 minimization then adjusts the Gaussian curve until the best fit is found. There was no background added in this fit as there was no background to be seen, i.e. zero counts in all bins between peaks.

Motivation for this technique is illustrated in Figure 5.2. In some cases, such as bin 231, the fitting distribution used varies dramatically. Using Poisson weighting the fit is adjusted such that the expected distribution of counts within the bin matches our data. All the peaks shown in Figure 5.1 were fitted as above and the results are shown in Table 5.1. The last column represents the number of bins between adjacent peaks.

The error shown in column 2 is the root mean square total error which comes from the covariance matrix of the fit. The error in the final column comes from the nonlinearity of the MCA ADC along with the above root mean square error.

It should also be mentioned that the reduced χ^2 , given in the penultimate column

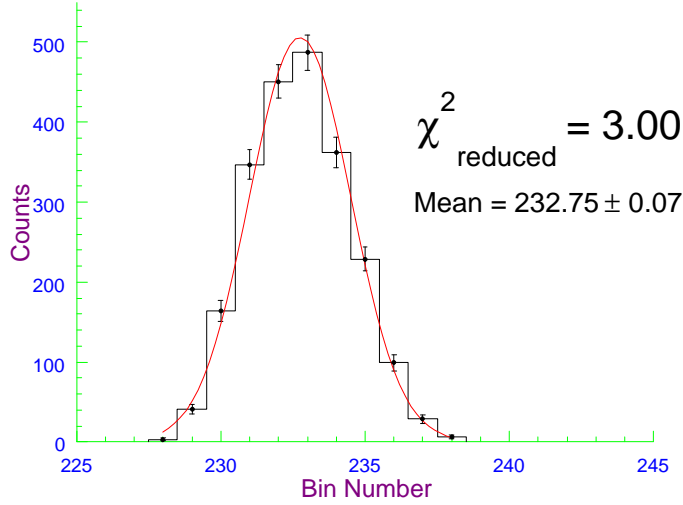


Figure 5.2: First peak of the calibration data in Figure 5.1 with the fit shown.

of Table 5.1, was a worry in some cases. However further analysis such as throwing away bad data points, or adding zeros to the left and right of the data did not change the mean of the fit, although it did provide slightly improved χ^2 . Also the above reduced χ^2 was improved with the use of equation 5.1, over a normal Gaussian fit with Poisson errors, in all cases except one. It could be that a Gaussian approximation was not correct, however the mean is all we want to extract and these fits are sufficient. As previously mentioned the time from peak to peak was 40 ns thus we can use the last row in Table 5.1 to extract our time calibration. The data from Table 5.1 was used to calibrate the MCA/TAC system. The results are shown in Figure 5.3.

A few things should be noted about this calibration. All the data were acquired near the central part of the MCA range and thus not all the calibration points were used, i.e. peaks 1,2 and 10 were not used in the calibration. The “local” slope plot shows there is non-linearity. Thus the final error in the fit was assigned the 0.14 % of the integral nonlinearity of the MCA plus that of the nonlinearity of the TAC; each was 0.1 % respectively. The period accuracy of the time calibrator was excellent (± 2 ps, for a 40 ns period) and did not make a contribution. The error from the fit of the slope was also negligible. The final result for the calibration was 47.00 ± 0.07 ps/bin.

Table 5.1: Summary of the Results from the analysis of the time calibration data.

Peak	Centroid (Bin Number)	$\chi^2/\text{d.o.f.}$	Peak-to-peak
1	232.75 ± 0.07	3.00	
2	1078.94 ± 0.04	1.35	846.2 ± 0.8
3	1926.11 ± 0.06	2.54	847.2 ± 0.9
4	2775.39 ± 0.05	2.06	849.3 ± 0.9
5	3625.98 ± 0.06	2.54	850.6 ± 0.9
6	4477.03 ± 0.07	4.06	851.1 ± 0.9
7	5328.26 ± 0.04	1.24	851.2 ± 0.9
8	6179.77 ± 0.04	1.17	851.5 ± 0.9
9	7031.73 ± 0.04	1.42	852.0 ± 0.9
10	7881.33 ± 0.05	1.95	849.6 ± 0.9

5.1.3 Studies using a ^{68}Ge Source

The MCP was purchased quite some time ago and had been worked on by other DRAGON personnel. Thus it was decided to start from square 1 and directly illustrate that the MCP was fast. To this end a ^{68}Ge source was used allowing coincidence measurements between the MCP and the puck/PMT combination. ^{68}Ge is a source which produces back-to-back 511s, via electron capture to ^{68}Ga and its eventual β^+ -decay.

The first test consisted of placing the source in the final slit box of DRAGON. The makeup of this box is shown in Figure 5.4. The source was placed just under the MCP and the PMT was setup below the box. The PMT bias was adjusted until the maximum output pulse was ≈ 1.5 volts. The electronics used for the test are shown in Figure 5.5. Although the LRS 621AL discriminator was not needed, it was included since it is required in the regular DRAGON MCP timing setup. The Ortec 9327 is the preamp/discriminator used to process the MCP timing signal. It uses a modified zero crossing technique which works with a range of signals with pulse widths from 250 ps to 5 ns. Thus for such fast signals as those from an MCP no pulse shaping cable or delay lines are needed. The output of the 9327 is a fast NIM signal. The

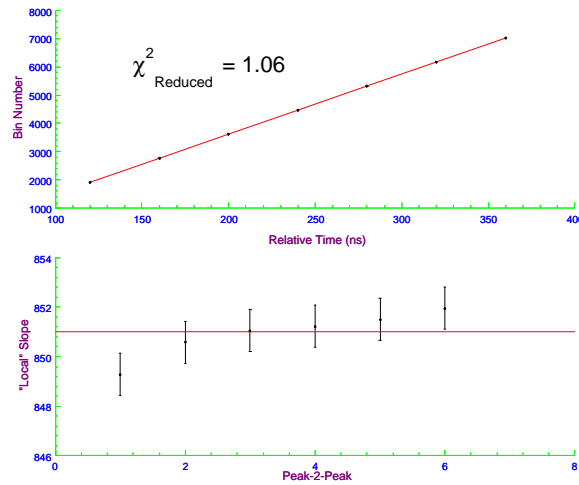


Figure 5.3: Top: Linear fit of the calibration of the MCA data from Table 5.1. Relative time is that from the first calibration peak. Bottom: fitted line along with the slope from peak to peak.

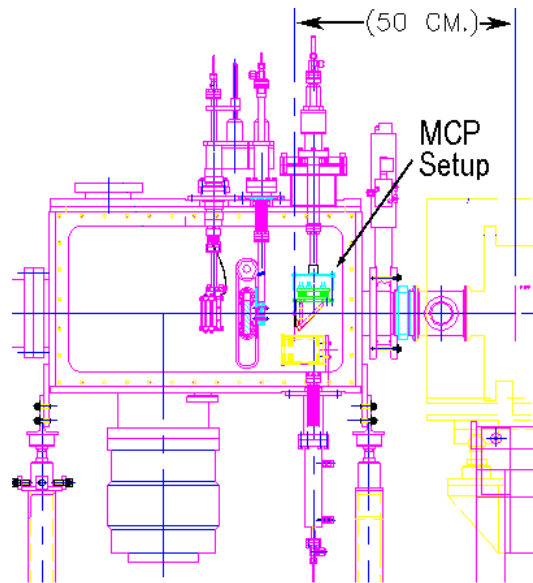


Figure 5.4: DRAGON “final slit” box components including the MCP setup as shown.
© TRIUMF, 2000, by permission.

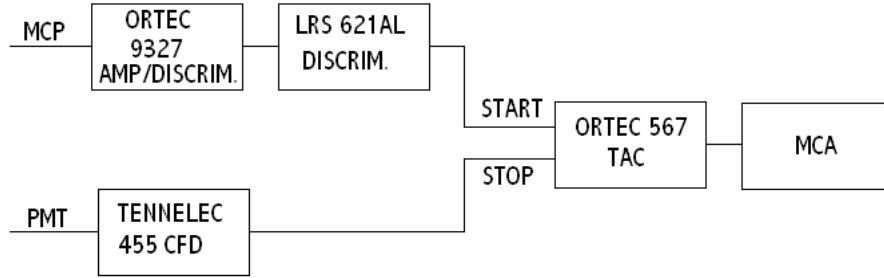


Figure 5.5: Box diagram of the electronics used for the PMT-MCP timing tests.

only adjustments made are the threshold and walk.

The results from the run are shown in Figure 5.6. The fit is a Gaussian with a constant background, done with Poisson weighting. In order to determine the timing capabilities of the MCP a second PMT was acquired. The characteristics of this PMT are not as well known; it was already constructed and the owner asked that we not disassemble it. The rise time was ≈ 3.5 ns. Thus it was not optimal for our application but would be sufficient as a third detector for timing measurements. Two other tests were then conducted: these were the coincidence of this second PMT with the MCP and the PMT-PMT coincidence. The results are shown in Figures 5.7 and 5.8.

With these results we can now determine the intrinsic timing resolution of the MCP. The total width of each of the peaks shown in figures 5.6 - 5.8 is a result of a folding of the resolution of each detector. These widths add in quadrature according to:

$$\sigma_{MCP}^2 + \sigma_{PMT1}^2 = (190 \pm 9 \text{ ps})^2 \quad (5.3)$$

$$\sigma_{MCP}^2 + \sigma_{PMT2}^2 = (322 \pm 12 \text{ ps})^2 \quad (5.4)$$

$$\sigma_{PMT1}^2 + \sigma_{PMT2}^2 = (318 \pm 7 \text{ ps})^2 \quad (5.5)$$

where σ_{MCP} is the standard deviation of the resolution of the MCP, and the two PMTs are designated $PMT1$ (“homemade” setup) and $PMT2$ (borrowed PMT)

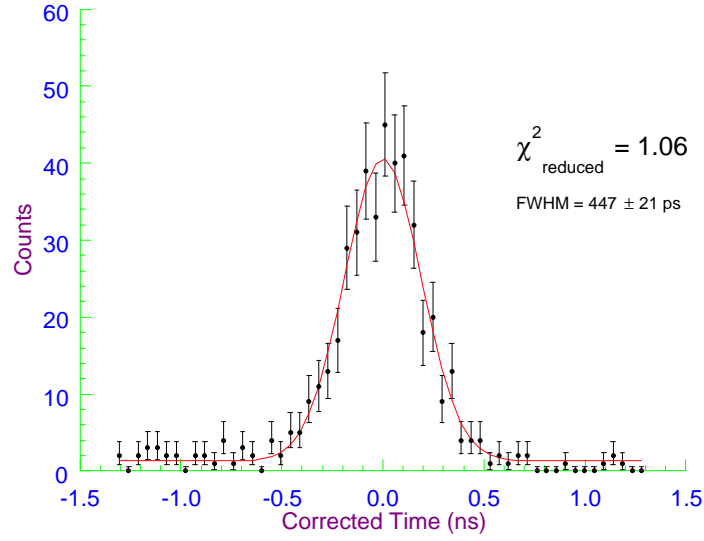


Figure 5.6: Results from the first run of a MCP-PMT1 coincidence with a ^{68}Ge 511 keV gamma source.

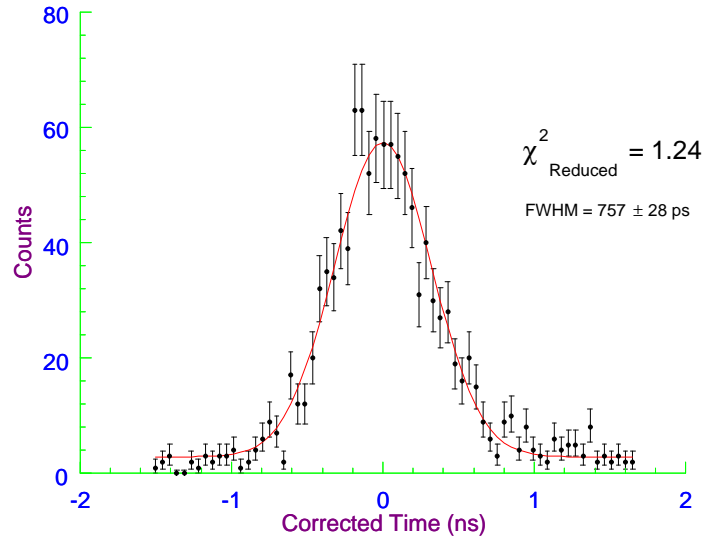


Figure 5.7: Results from the run of a MCP-PMT2 coincidence with a ^{68}Ge 511 keV gamma source.

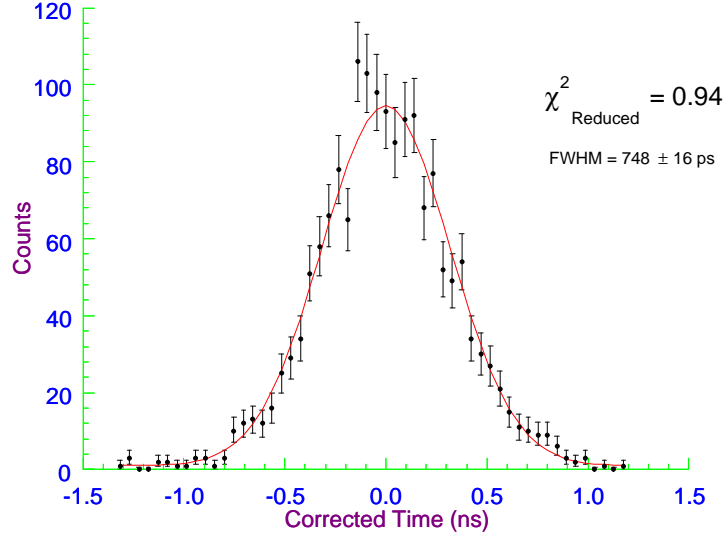


Figure 5.8: Results from the run of an PMT1-PMT2 coincidence with a ^{68}Ge 511 keV gamma source.

respectively. The result is $\sigma_{MCP} = 138 \pm 17$ ps. We were surprised to determine that the timing of the first PMT was just as good as that of the MCP. The two PMT setups resulted in $\sigma_{PMT1} = 130 \pm 18$ ps and $\sigma_{PMT2} = 412 \pm 8$ ps time resolutions. One might start to think about other possible sources of error involved in the tests to explain this result. Several runs were conducted in which variations in the CFD or MCP were investigated, such as walk and zero crossing. These tests showed that the zero crossing of the CFD had a definite effect and that our settings were optimized. That is, when we adjusted the zero crossing setting on the CFD such that we thought it got worse, the timing did in fact also become poorer. However the goal of the test was to ensure that we could attain good timing from the MCP and these results clearly illustrated that we could. It should be noted that these results are not just the detector resolutions but also that of the electronics used. However these timing widths are the ones we are interested in since they show that our entire setup can be used for fast timing applications. An upper limit on the capability of the TAC-MCA is given by the pulser tests, in which the resolution of each pulse was ≈ 80 ps. This gives a lower limit on the timing of the MCP of 112 ps. The setup may not be

completely optimized since sub 100 ps time resolution (σ) with the use of MCPs has been observed elsewhere [55, 57, 58, 59].

Generally when MCPs are used to detect photons a photocathode is placed in front of the MCP [35, 69]. The detection efficiency of the 511s would have been $< 1\%$ [43], however the lack of efficiency was not a worry. The one factor which would have contributed to the timing measurement was the very small signal produced by the MCP when using the ^{68}Ge source. It was not known where the 511s were interacting along the MCPs. The threshold on the discriminator was set such that the low energy pulses were not considered. However the pulses were still smaller than with any high Z element. For example these pulses were on the 1-3 mV level or less, whereas pulses up to 25 mV have been seen with ^{21}Ne . In any case this suggests that better timing is possible.

One final comment is that the calibration was checked by adding delays to the stop signal, a calibration of 45.6 ± 0.8 ps/bin was found, where the error here is attributed to the difference in cable lengths used during the runs. A 1.25 % tolerance was allotted to the cable lengths; this was found by comparing several 4 ns lemo cables to one another, it was found that the length of most were within 1 cm of each other while one was 2 cm away from the norm, the total cable length was ≈ 80 cm. In the end the time calibrator calibration was chosen due to its superior accuracy.

5.1.4 Studies using a ^{148}Gd Source

Now that it was established that the MCP was fast and we had at our disposal other fast detectors we moved on toward studies of the entire MCP setup. As mentioned previously the ^{68}Ge runs only tested the MCP itself. Recall that the DRAGON MCP setup involves an electrostatic mirror and carbon foil as well as the MCP. A new design for PMT1 was made such that it would fit at the end of DRAGON. This design included the same scintillation material size and thickness. No teflon tape or aluminized mylar were used since these would have produced unwanted straggling. The final configuration is shown in Figure 5.9, and a simplified setup of the experiment is shown in Figure 5.10. 3.183 MeV alphas from a ^{148}Gd source impinged on a $20\text{ }\mu\text{g}/\text{cm}^2$ carbon foil producing secondary electrons, the alphas then continued on to

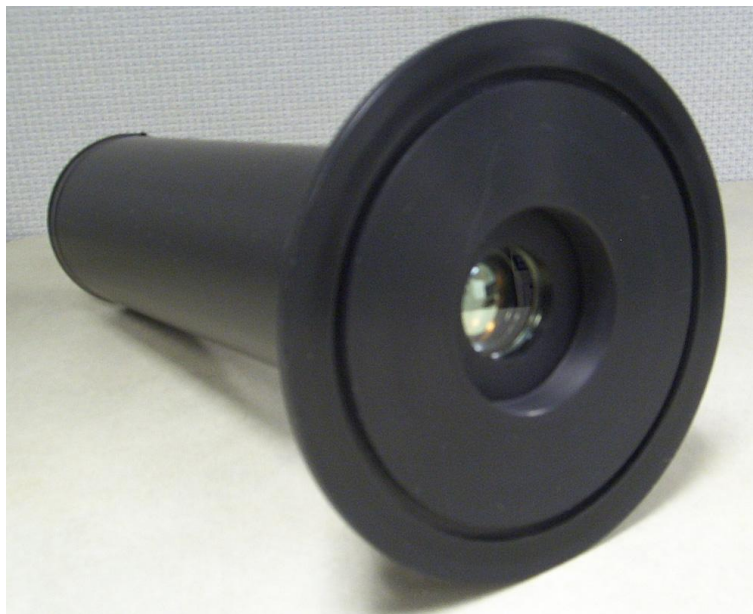


Figure 5.9: The fast PMT and puck used during the timing studies of the MCP.

the PMT; the MCP detected the electrons after they were accelerated and bent as described in section 2.2.4. The electronics used were the same as those described for the ^{68}Ge tests, see Figure 5.5.

When the PMT was first biased there was a large background at a signal pulse height of ≈ 250 mV, at a bias which gave pulse heights of ≈ 1.5 V from the alpha source. The rate of these pulses was ≈ 300 Hz. These were eliminated by applying a 750 mV threshold on the CFD input. Once this was done the S/N was about 18:1. The background and background subtracted pulse height distributions, above the threshold, are shown in Figure 5.11. The top figure is a background run with the alpha source blocked, while the bottom figure is a background corrected pulse height spectrum for the alpha source on the PMT. Clearly there is a background source in the final slit box producing events at a rate of about 1 Hz above our threshold. Most likely this is a β source. At the above S/N ratio and given our studies require a coincidence, its contribution is insignificant.

Figure 5.12 illustrates the coincidence results. As can be seen there is an apparent tail on the slow PMT or fast MCP side (the stop and start signal were inverted

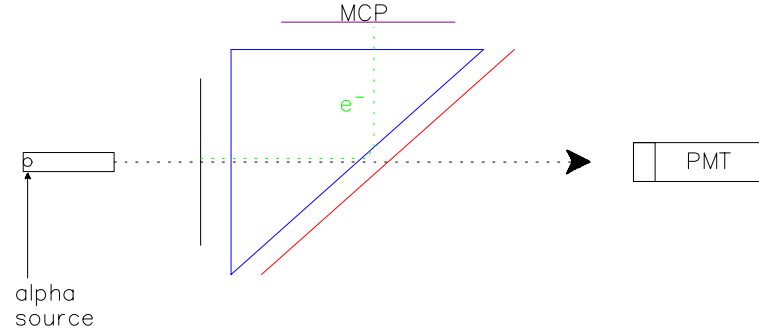


Figure 5.10: Simplified schematic of the timing studies performed with a ^{148}Gd alpha source.

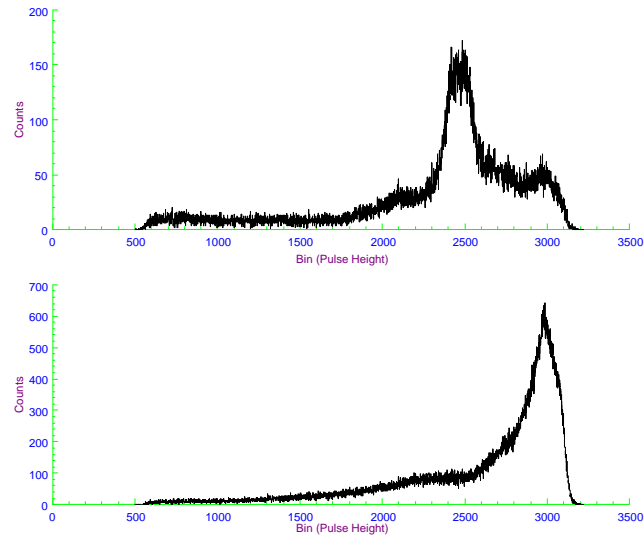


Figure 5.11: Top: Background pulse height spectra above the 750 mV threshold on the CFD. Bottom: Background corrected pulse height spectra from the 3.183 MeV ^{148}Gd alphas.

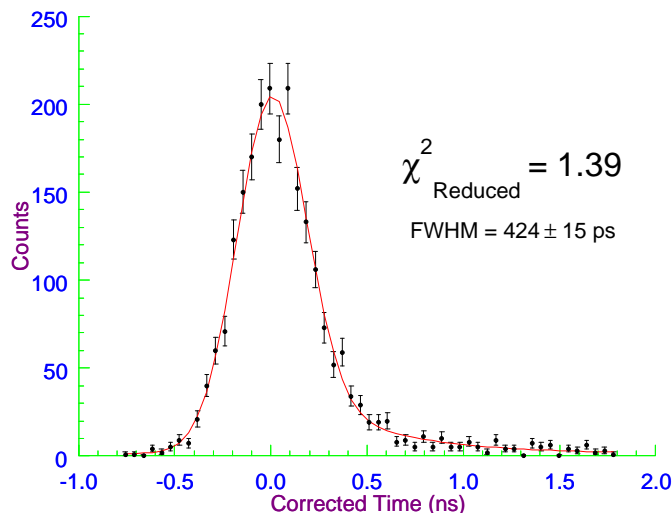


Figure 5.12: Coincidence spectrum between the MCP and PMT with a 3.183 MeV ^{148}Gd alpha source.

for this run). Generally it is hard to believe a signal might come faster than normal. However, according to the MCP 9327 ORTEC preamp manual [70] if pulses arrive just above threshold it can result in faster signal processing than that with a bigger pulse. Adjustment of the walk can be used to minimize this effect, and this was investigated. However no effects were seen. A second possible cause was an incorrect zero crossing setting on the CFD processing of the PMT signal. Again when investigated. No easily discernible effects were seen. Although the CFD zero crossing setting was investigated we believe this may have been the cause of the tail. We only ever tried cables of integer ns length. With such short rise times this may have a definite effect on the CFD processing, non-integer cable lengths such as 1.5 ns may have solved this problem.

The run shown has the worst reduced χ^2 (although still not bad) of all the runs analyzed. It is clear a simple Gaussian will not suffice as a decent model; reduced χ^2 between 2 and 5 are found if this is tried. Before an explanation of the fit it should be emphasized that the goal of this test was to show that the whole MCP setup was fast and to get a measure of the time resolution. A measurement of the detector

response function wasn't the primary goal. However in order to extract the timing resolution with a detector of similar rise time characteristics, for example a PGAC (see Reference [71]), this tail was modelled as an exponential tail smoothed by an error function. The fit used is given by Equation 5.6.

$$b + \frac{a}{\sigma\sqrt{2\pi}}e^{\frac{-(\bar{x}-x)^2}{2\sigma^2}} + \frac{1}{2}\left(1 - \operatorname{erf}\left(\frac{\bar{x}-x}{\sigma\sqrt{2}}\right)\right)ce^{\frac{\bar{x}-x}{d}} \quad (5.6)$$

Where b is a constant background, a is the normalization of the Gaussian, erf is again the error function defined previously by equation 5.2, c is the normalization of the exponential tail and d is the decay constant of the tail. Clearly these results illustrate that our entire detection system can be used for fast timing studies.

Some time had passed between these runs and those with the ^{68}Ge source, and the MCA was in use involving other studies. A check of the calibration was done again by adding a 4 ns delay to the stop signal. A fit to the peaks produced 45.6 ± 0.8 ps/bin, the same as the previous check. Thus the same time calibration as above was used, that is 47.00 ± 0.07 ps/bin.

5.1.5 Studies Using ^{21}Ne at $E_{cm} = 258.6$ keV

The final studies performed were with the use of a higher mass element, i.e. in the mass range of accepted DRAGON experimental proposals. These tests were performed in two phases one with the PMT placed at the end of DRAGON, and the second was under normal DRAGON operating conditions with a DSSSD as the end detector. The goal with the PMT was again an attempt at a fast timing measurement. While the goal with the DSSSD was to determine what kind of mass resolving power these DRAGON end detectors provided in an Et^2 analysis. Both cases involved the use of a TAC whose output went into one of the DRAGON Silena ADCs. The currently used LRS TDCs have minimum bin widths of 500 ps and thus were not useful.

PMT tests

The electronics are shown in Figure 5.13. ^{21}Ne was delivered to DRAGON from OLIS at $E_{lab} = 269.7$ keV/u. The MCP was used as the start signal. Since the pulses from the PMT were in the range 100 - 200 mV, and with a 75 mV threshold there was a

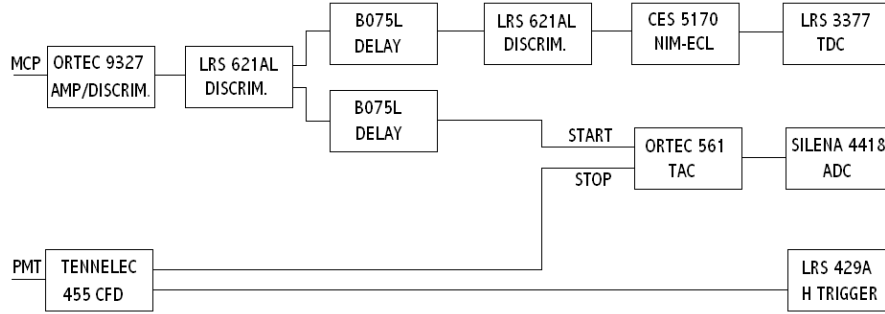


Figure 5.13: Electronics schematic with a PMT at the end of DRAGON.

large noise component. This noise, also mentioned in the previous section, was on the order 300 Hz, whereas the MCP noise was on the level 1 Hz.

Since we were now using a different ADC, the TAC/(Silena ADC) setup had to be calibrated. Several runs were done with a pulser using delay cables; that is the pulses from the pulser were split and fed into the start and stop signals of the TAC with varying delay on the stop signal. The final result was 42.1 ± 0.2 ps/bin, where a smaller fractional error has been allotted to the longer cables used than previously mentioned. Also with these beam tests the DRAGON data acquisition was used to collect the data. NOVA, a data analysis package, was used in an off-line analysis mode to replay the data. These data were then exported and again analyzed with the Extrema software package. NOVA is a versatile data analysis software package which takes as input the raw data and allows one to perform calculations and plot data. Information about the NOVA software package can be found from Reference [72].

Although the primary purpose of DRAGON is the measurement of reaction yields, the study of the $^{21}\text{Ne}(p,\gamma)^{22}\text{Na}$ reaction was done under much better conditions elsewhere see Reference [73]. The theory behind proton capture reactions can also be found in Rolfs and Rodney [54]. A resonance at $E_{cm} = 258.6$ keV (beam energy) in the $^{21}\text{Ne} + p$ system was selected due to its strength and the availability of a ^{21}Ne beam. During the first tests DRAGON was used as a transport system for attenuated ^{21}Ne , with no gas in the target. In this case the Ne was intentionally directed into the PMT puck.

Since the number of secondary electrons is proportional to the stopping dE/dx of

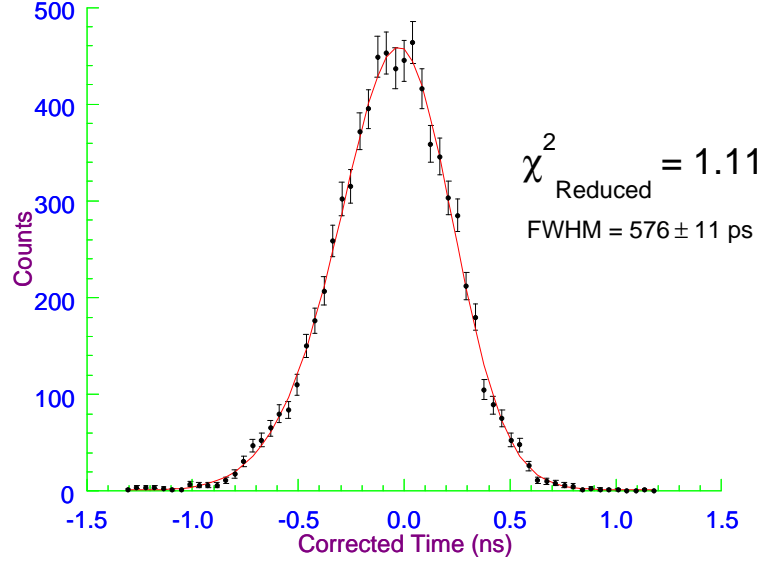


Figure 5.14: Coincidence spectra between the MCP and a PMT mounted at the end of DRAGON.

the particle, the pulses from the MCP in this case were much larger than those from the alphas. However the pulses from the PMT were much smaller, in the range 100 - 200 mV. This is to be expected from Birks formula, which illustrates the fact that for ions of larger dE/dx the luminescence per unit length is decreased.

The result of the coincidence is shown in Figure 5.14. The fit was again done utilizing equation 5.6, with $(\bar{x}-x)$ in this case being reversed. One of the non-negligible timing factors was the straggling of the beam and recoils through the thin foil ($20 \mu\text{g}/\text{cm}^2$). SRIM [75] was used to give an estimate of this straggling width. SRIM takes as inputs the beam mass, energy and foil thickness and performs a Monte Carlo simulation of the straggling through the foil. In this case the input parameters were 20.994 u, 5.664 MeV and a carbon thickness of $0.08877 \mu\text{m}$. SRIM then provides the energy of the ions after the foil, by starting off several initial ions of given energy the straggling through the foil is then known. The result is shown in Figure 5.15.

With the knowledge of this energy spread we can then estimate the spread in time over a 43 cm path length (\approx length between the puck and MCP foil). We find

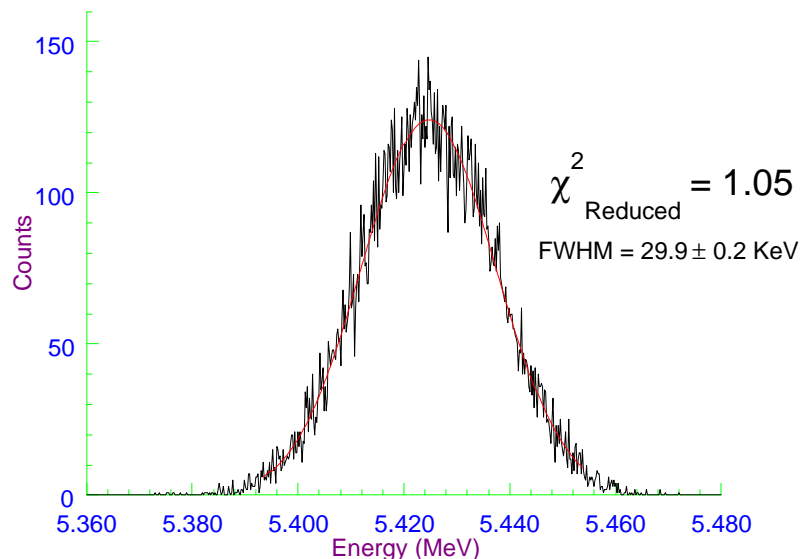


Figure 5.15: SRIM simulation of the spread in energy of 5.664 MeV ^{21}Ne after transmission through a $20 \mu\text{g}/\text{cm}^2$ carbon foil.

$\Delta t \approx 170$ ps. A similar calculation for ^{22}Na results in Δt of ≈ 260 ps, with the difference lying in the increased energy straggling from the increase in nuclear charge; and the larger mass. It will be seen below that this 260 ps contribution to the width is small since the energy spread is dominated by kinematic broadening due to gamma emission in the reaction. Using this information for ^{21}Ne we can make an estimate of our detector plus beam resolution. This leads to 550 ps. If we now assume our detector response was the same in the run with alphas and this beam test, we can get an estimate of the beam spread. Recall in Figure 5.12 that the timing with alphas was 424 ± 15 ps. This leads to a beam time spread of 350 ps, and an energy spread of 0.58 %. However a few words of warning should be mentioned about the assumptions going into this number. Any spread in energy from the alpha source has not been taken into account, and as mentioned above we have assumed the detector responses to be the same for alphas and higher mass elements. Also the beam delivered was not typical of that delivered by ISAC, transmission through the target degraded as time went along. The smaller pulses from the PMT may have also contributed to poorer

timing. Therefore we might consider the above number as an upper limit.

The next step was to run with gas in the target and DRAGON in recoil-beam separation mode. It was the hope that this would give us an opportunity to look at the timing between the recoils (^{22}Na) and the leaky beam. It was already known that at this energy the DRAGON EMS didn't suppress all the beam [73]. ^{21}Ne of energy $E_{lab} = 269.7$ keV/u impinged on a nominal pressure of 0.76 Torr H_2 and exited at an energy of 267.4 keV/u. Generally speaking DRAGON can run at much higher pressures, however larger pumping tubes and exit aperture were in place for a large recoil cone angle ^4He capture reaction. With the proper setup pressures of up to 10 Torr of H_2 may be reached. The resonance energy was known to be at $E_{Lab} = 268.9$ keV/u [73], and with an average energy loss of ≈ 2.3 keV/u at 0.76 Torr, the running conditions were adequate for our purposes.

The timing spectrum between the MCP and PMT is shown in Figure 5.16. Clearly the leaky beam is well separated from the recoils of interest. Also shown in blue are the counts in which a gamma trigger from the BGO array has been acquired in coincidence with a heavy ion. A few side notes here are that we can see that 2 of the leaky beam counts made it through the BGO coincidence cut. There are a total of 1674 “leaky” counts. This suggests a suppression factor on the order of 840:1. However this should certainly not be taken as an absolute suppression factor, since more statistics would be needed in order to make a proper estimation. The BGO efficiency can be determined from previous runs to be 41.0 ± 0.2 %. The measurement here suggests 35 ± 3 %, with the major portion of the error being statistical. However the MCP foil may have been cutting into some of the acceptance due to its small 19 mm diameter. Presumably events with a 90° gamma kick would be cut out; these events having a higher BGO efficiency would be lost, resulting in the slight decrease in overall BGO efficiency. The width of the ^{22}Na peak is dominated by the 7 MeV gamma ground state transition which has been observed to have a branching ratio of 51 % [77]. The upper and lower energy limits of the recoil can be shown to be that given by equation 5.7.

$$E_r = E_b \frac{M_b}{M_r} \left(1 \pm \frac{2E_\gamma/c}{\sqrt{2M_b E_b}} + O(E_\gamma^2) \right) \quad (5.7)$$

Where E_r and M_r are the recoil energy and mass, E_b and M_b are the beam energy and mass and E_γ is the gamma energy. The 7 MeV gamma leads to an energy spread

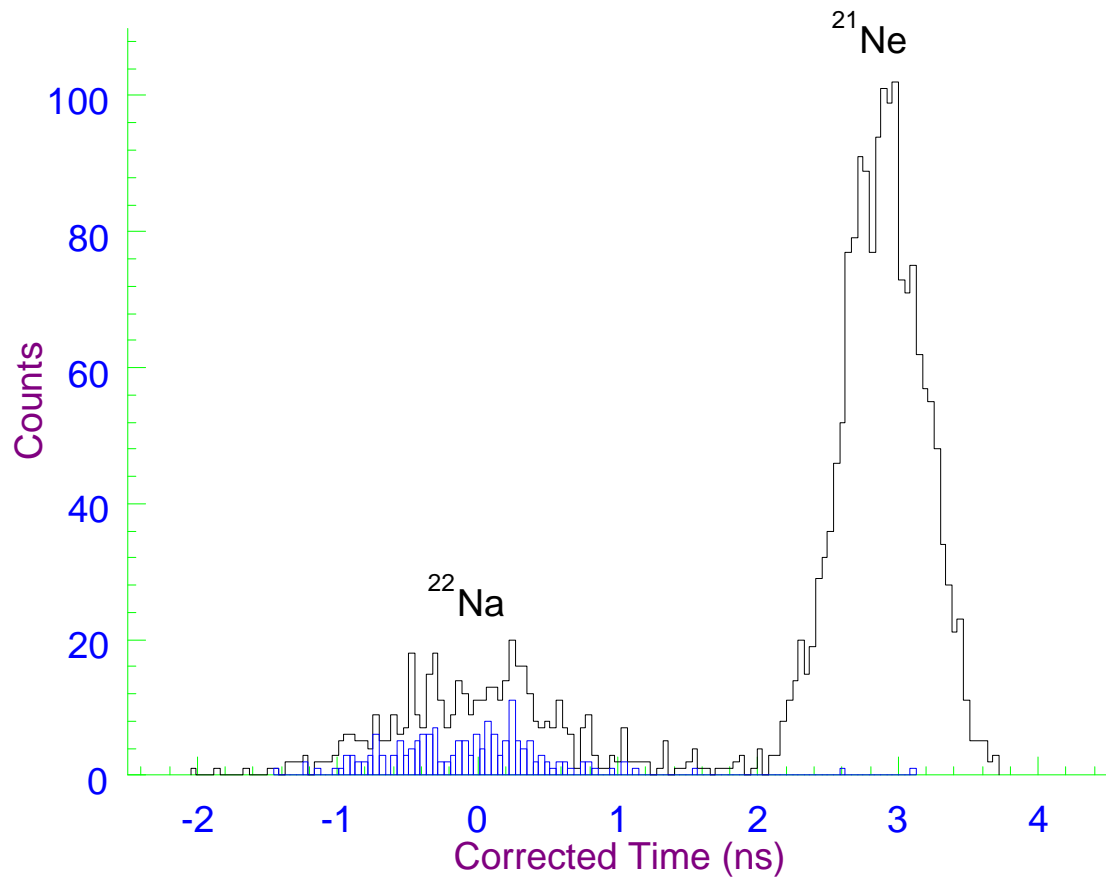


Figure 5.16: Timing spectra showing the clear separation of ^{22}Na from ^{21}Ne . Also shown in the blue curve are the counts in coincidence with the BGO array.

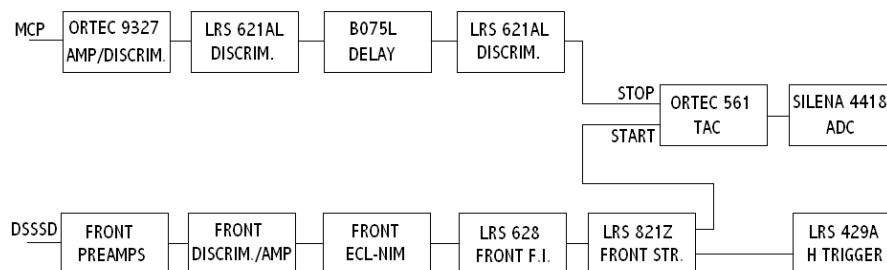


Figure 5.17: Electronics used with the DSSSD at the end of DRAGON.

of 200 keV, much larger than that of the beam spread or that from straggling in the thin MCP foil. Finally it is worth mentioning the timing limitations due to the beam energy spread, foil thickness and target thickness. At 4 Torr and 5.66 MeV the ^{21}Ne beam generally loses 14 keV/u; this energy loss is on the same order as that of the foil so we would expect the same straggling. Given the quoted 0.2 % beam energy spread and 200 ps for both the foil and gas target, this leads to a limitation of 318 ps FWHM (over a 50 cm path length). We also expect this to be larger for higher mass elements.

DSSSD Tests

Generally it may not be the case that the leaky beam and recoils of interest are so nicely separated in a singles time-of-flight spectrum. In this scenario one may employ an $E t^2$ analysis for mass identification, or any other technique in order to attain separation of the recoils from leaky beam. This requires the use of two fast timing detectors and a detector with good energy resolution. A DSSSD has been the preferred detector up to this point and since it gives good energy and decent timing signals it was used as a first test during these first studies of possible future setups with other detectors. The electronics setup is shown in Figure 5.17. The DSSSD was used as a start signal due to its low background rate.

The TAC was used again due to the binning of the DRAGON TDCs. The DSSSD was cooled in the hopes that its timing would improve, however no dramatic effects

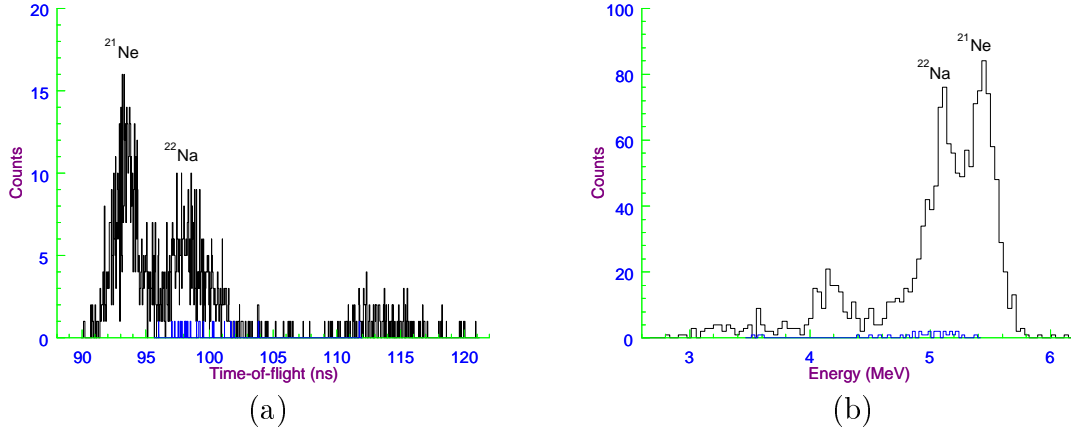


Figure 5.18: Data from the $^{21}\text{Ne}(p,\gamma)^{22}\text{Na}$ reaction. (a) Time of Flight spectra of ^{21}Ne and ^{22}Na between the MCP and DSSSD. (b) Energy spectra of ^{21}Ne and ^{22}Na from the DSSSD.

were seen. This setup allowed a slightly longer distance between the start and stop detectors (≈ 54 cm). The target was loaded with 0.76 Torr of hydrogen and the resulting data from the reaction is shown in Figure 5.18(a) and (b).

Figure 5.18(a) illustrates that the time-of-flight spectrum allowed very good separation. The time resolution between the DSSSD and the MCP was measured at 1.6 ns; however, better timing is possible as not all factors such as the DSSSD amplifier shaping time were investigated. The DSSSD signals are processed with the leading edge technique which has walk associated with it with varying pulse heights. This was not investigated so improved time resolution with the DSSSD is viable. Also shown in Figure 5.18(b) is the associated energy spectrum. Both figures also show the coincidence counts in blue. It is unknown why the number of coincidences were so low as compared to the expected BGO efficiency. Under normal running conditions this would have to be investigated. However due to the very short allotted beam time, data were taken as it seemed from the time spectra that ^{22}Na events were coming in. Even though the timing gives good separation we shall still discuss other techniques which could be pursued in the future.

As mentioned generally one employs whatever technique allows separation of the good recoil events from that of the leaky beam. Two of these are shown in Figures

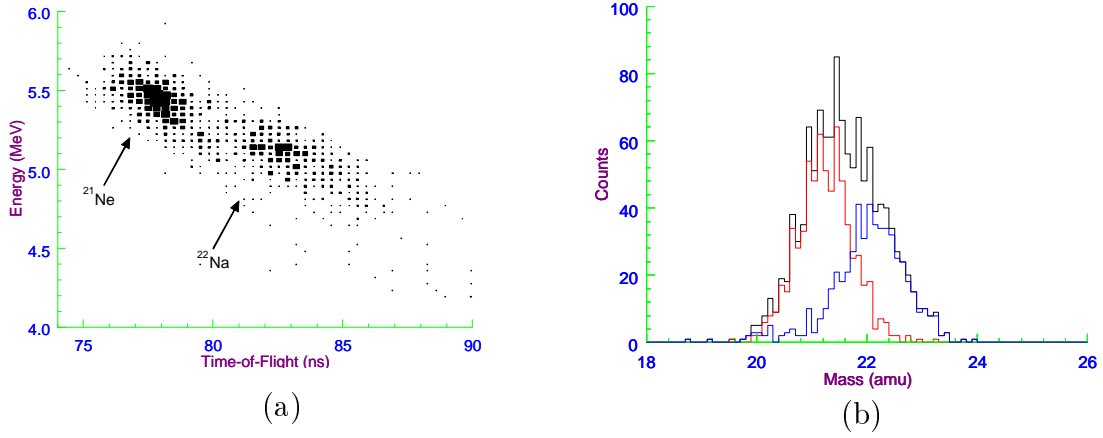


Figure 5.19: Data from the $^{21}\text{Ne}(p,\gamma)^{22}\text{Na}$ reaction. (a) Two dimensional plot of energy versus time of flight. (b) $E t^2$ mass spectra of the leaky beam and recoils.

5.19(a) and (b). The 2-d plot shows good separation due to the good separation in timing. The $E t^2$ plot requires more discussion.

The length between detectors was measured by using the timing spectra shown in Figure 5.18(a). That is the ^{21}Ne energy was determined using the NMR probe magnetic field measurement located at MD1. The energy after the thin carbon foil used with the MCP setup was determined using the SRIM software. The mean ^{22}Na energy was determined using equation 5.7, and its energy after the foil was also determined using SRIM. This energy loss agreed within 2 keV (out of ≈ 240 keV) with the energy determined using the DSSSD energy calibration (given below) before and after the MCP foil was put in. Then with the time calibration giving the difference in time between the beam and recoils the length was determined by equation 5.8 to be 65.7 ± 0.5 cm, where 5.8 comes from the classical kinetic energy equation[‡]. This length is almost 12 cm larger than the expected 54 cm path length. This lead to the source of a major problem which is still not understood.

$$l = \frac{c(t_{Na} - t_{Ne})}{\sqrt{\frac{M_{Na}c^2}{2E_{Na}}} - \sqrt{\frac{M_{Ne}c^2}{2E_{Ne}}}} \quad (5.8)$$

[‡]Relativistic effects are small in our case, using $T=mc^2(\gamma-1)$ we find for 1 MeV/u mass 20, $\gamma = 1.001$

To begin with the energy of the strip detector was calibrated using previous runs with ^{21}Ne . The run numbers as well as the beam energy are shown in Table 5.2.

Table 5.2: Previous runs used to calibrate the measured energy of the DSSSD.

Run #	Energy	Channel #
4955	5.5	5471
4989	5.5	5467
6898	10.66	10902
6902	10.89	11083
6907	10.61	10831
6925	15.5	15120
6931	16.2	15872

For reference to future NOVA users the calibration was determined to be:

$$E(\text{MeV}) = -0.2903 + 1.0287 \times 10^{-3} E_c \quad (5.9)$$

where E_c is the channel number in the DSSSD energy spectrum.

Using this energy calibration the resultant heavy ion peaks were on the order 0.8 MeV lower than that expected from the NMR and SRIM. A length estimation using this energy calibration, for both Ne and Na^* , was found to be 54.7 ± 0.4 cm. This agrees very well with the expected length of ≈ 54 cm. There are a few conflicting results with this finding. The first is that the MD1 NMR energy determination was calibrated with known resonance energies Reference [73], and its reliability is very good. Secondly we don't expect to see any recoils if we were off resonance, i.e. at the energy measured by the DSSSD. There are lower energy resonances in ^{22}Na , for example see Reference [77]. However the strength of these resonances are very weak. We would therefore expect small yields of ^{22}Na . It should also be noted that the mass selected by the magnetic and electric dipoles may be calculated using the squared magnetic to electric ratio. This can be seen if we solve for the magnetic field B in

*At these low energies the pulse height defect may play an important role in the energy determination.

equation 2.2, and the electric field \mathcal{E} from equation 2.5 and take the ratio B^2/\mathcal{E} and solve for the mass m we find:

$$m = \frac{B^2 \rho_{MD1}^2 q}{\mathcal{E} \rho_{ED1}} \quad (5.10)$$

where ρ_{MD1} is the MD1 bend radius and ρ_{ED1} the ED1 bend radius. This confirmed that our recoil tune was in fact set on mass 22. The lower energy is also not a result of an incorrect MCP carbon foil thickness, since attenuated ^{21}Ne beam with no gas in the target and no MCP or foil in, give the same 0.8 MeV energy offset. The evidence in favor of the lower energy is the energy calibration of the DSSSD and the good agreement with the length determination.

Both of the above length determinations depend on the time calibration. Our results could be greatly effected if this was incorrect. A smaller time/bin calibration could result in the correct path length with the use of the MD1 energy determination. However the problem is only exacerbated if we consider the following: the same time calibration was used in the case of the runs with the PMT and the calculated path length agreed well with the estimated length. A change in this would produce a change of ≈ 8 cm in the length of the PMT-MCP foil distance. The solution to this problem is still unknown.

An Et^2 analysis was attempted using both of the energy calibrations. The “zero” time was determined from the time of the ^{22}Na recoils. That is their mean time was determined from their energy and the time-of-flight length. The results shown herein are those using the DSSSD energy calibration. The mass in terms of the energy, time of flight and path length can be determined by the simple non-relativistic kinetic energy equation and yields:

$$m = \frac{2Et^2}{l^2} \quad (5.11)$$

Substituting the above length of 54.7 cm and changing to preferred units one can show that the mass is then given by equation 5.12.

$$m(\text{amu}) = 6.457 \times 10^{-4} E(\text{MeV}) t(\text{ns})^2 \quad (5.12)$$

Both analyses produce essentially the same result which is shown in Figure 5.19(b).

The result is a bit surprising since the elements are separated fairly well in timing. One factor which could affect the mass determination was the dead layer in the silicon detector, i.e., the energy loss of ^{21}Ne is different from that of ^{22}Na . This would result in a shifting of the determined mass. Given the effective dead layer thickness from Wrede [80], the difference in energy loss of the ^{21}Ne and ^{22}Na through the DSSSD dead layer, was determined using SRIM, it turned out to be ≈ 100 keV. This is on the order of 2 % of the total energy, which would have the effect of reducing the ^{22}Na mass by 0.4 to 0.5 mass units in comparison to ^{21}Ne . By placing cuts from the time spectrum on the mass spectrum we can see where each element resides. The Blue curve shown in Figure 5.19(b) shows the ^{22}Na events and the red curve is the ^{21}Ne events, give or take a few since the time cut is not perfect. A fit illustrates that the ^{22}Na lies on mass 22 and the Ne lies at 21.2 u.

In the end the limiting factors are the time and energy resolution. The mass resolution includes correlation between the energy and time terms. The general expression for the total variance of the mass m in terms of E , t and l is given by:

$$\sigma_m^2 = \lim_{N \rightarrow \infty} \frac{1}{N} \sum_{i=1}^N \left[(E_i - \bar{E}) \left(\frac{\partial m}{\partial E} \right) + (t_i - \bar{t}) \left(\frac{\partial m}{\partial t} \right) + (l_i - \bar{l}) \left(\frac{\partial m}{\partial l} \right) \right]^2 \quad (5.13)$$

where N is the number of measurements. In the limit of an infinite number of measurements, the means converge to their true mean. One can then show that the variance of the mass is given by:

$$\left(\frac{\sigma_m}{m} \right)^2 = \left(\frac{\sigma_E}{E} \right)^2 + 4 \left(\frac{\sigma_t}{t} \right)^2 + 4 \left(\frac{\sigma_l}{l} \right)^2 + 4 \frac{\sigma_{Et}^2}{Et} \quad (5.14)$$

Any correlation between energy and length or time and length doesn't exist so those terms drop out. The term σ_{Et}^2 is given by:

$$\sigma_{Et}^2 \equiv \lim_{N \rightarrow \infty} \frac{1}{N} \sum_{i=1}^N [(t_i - \bar{t})(E_i - \bar{E})] \quad (5.15)$$

We can understand the correlation between the energy and time by inspection of equation 5.15. Under perfect conditions these two terms are perfectly correlated, that is, when the energy is below the mean energy, the time-of-flight should be longer than its mean and vice versa. This results in a term which is always negative and reduces

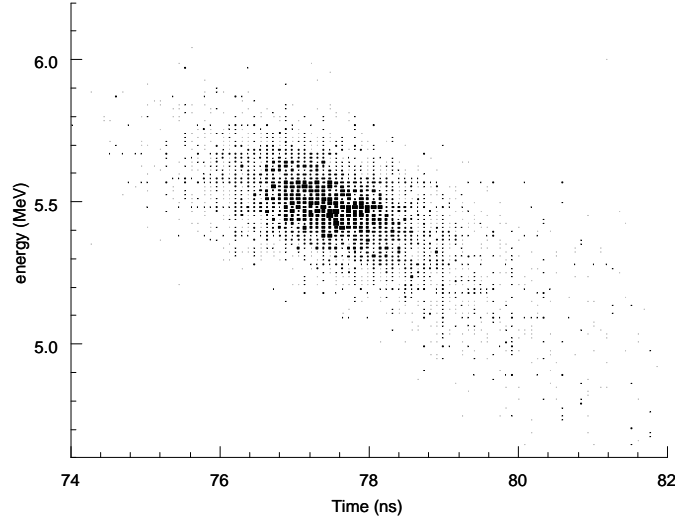


Figure 5.20: Blowup of the energy vs. time plot for attenuated ^{21}Ne beam from the MCP-DSSSD setup illustrating the strong energy-time correlation.

our error of the mass determination. If we neglected this term we would essentially be adding the same error twice. The energy loss through the DSSSD dead layer complicates things since this perfect correlation will be partly washed out. However on average we still expect a strong correlation between the energy and time-of-flight. During the run the low- β buncher was used to produce a time focus at the end of DRAGON. We expect this to increase the correlation due to the additional energy spread produced by the buncher to generate the time focus. Before the buncher was turned on we did see a strong correlation which is unexpected due to the combination of poor detector time resolution and the small, 0.2 %, beam energy emittance expected from ISAC. The correlation between the energy and time may be seen in Figure 5.20, which is from a run after the buncher was set at the desired voltage.

The time and energy resolution can be found from attenuated ^{21}Ne directed onto the MCP-DSSSD system. These data suggests energy and timing resolutions of 5.5 % and 2 %. Due to difficulties of extracting single data events out of the raw data files a two dimensional plot of energy vs. time was used to get the correlation term σ_{Et}^2 . The bins constructed had time and energy widths of 84.2 ps and 12.8 keV

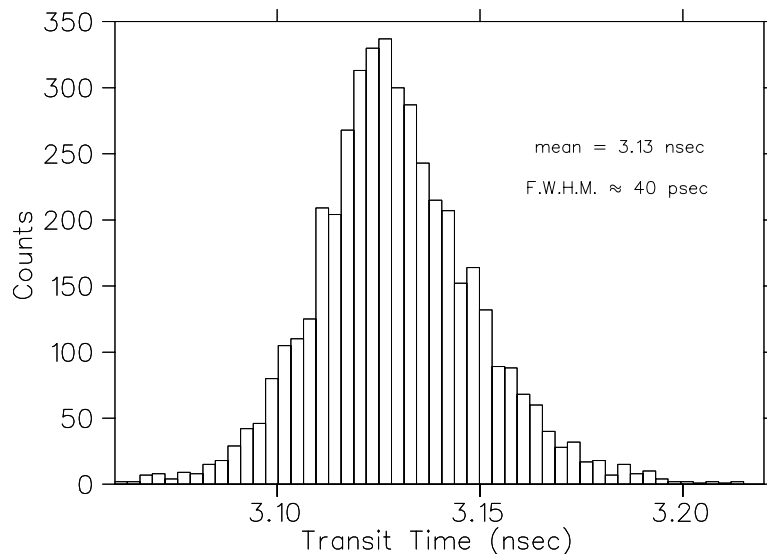


Figure 5.21: Transit time of the secondary electrons from the carbon foil to the MCP.

respectively. Neglecting any length errors, the above timing and energy resolutions along with the correlation term suggests a mass resolution of 0.62 u while the data suggests a mass resolution of ≈ 1 u. A simple calculation neglecting the correlation produces an underestimate of the mass resolution of 1.43 u. Additionally we expect poorer resolution from the ^{22}Na due to the spread in energies from the gamma kick, and increased straggling due to the higher atomic number.

5.1.6 Simulation results

It is well documented that the spread in transit time of the secondary electrons using a mirror arrangement is small (for example see References [55] or [57]). For completeness the spread given by our simulation described in chapter 4 is shown in Figure 5.21. As expected the transit time spread from the foil to the MCP of the secondary electrons is small, and we don't expect any significant timing resolution to be lost.

A small Monte Carlo simulation, given in appendix B, has been written to model

the correlation in an Et^2 analysis. It expects the user to have prior knowledge of several factors. These include: the energy spread of the beam after the MCP foil, the energy straggling due to the detector and the intrinsic time and energy resolutions of the detectors. The energy spread after the foil may be determined using SRIM or any similar package; generally this energy spread would include that of the straggling through the gas target, the MCP foil and the intrinsic beam emittance. The energy straggling through the energy detector, such as the DSSSD dead layer or the IC window and dead layer may also be determined using SRIM. The simulation assumes a Gaussian distribution for the energy spread and performs the Monte Carlo. A particle is given the mean energy convoluted with the energy width after the foil. The time-of-flight is then calculated for this energy and it is convoluted with the detector time resolutions. The particular particle energy is then convoluted with the intrinsic detector energy resolution and the energy spread through the dead layer (or foil and dead layer for the IC).

It was the hope that this Monte Carlo simulation would allow a determination of the timing needed for the various mass and energy ranges of experiments which have been accepted. The strong correlation we saw turned out to be quite useful in the sense that if a detection system with timing resolution around 500 ps is commissioned, we expect there to exist a strong correlation in an Et^2 study. This is because the beam energy spread, due to intrinsic beam spread and straggling in the gas target and foil, should also lead to time spreads on the order of 400 - 500 ps. It is unknown why the correlation was so strong since with the expected 0.2 % energy spread we would expect any observable correlation.

One way to estimate the energy spread was to look at the energy spread in the DSSSD before and after the use of the buncher. Before the buncher was turned on we saw a 4.7 % energy spread in the DSSSD while during its use we saw a 5.5 % energy spread. Thus we can estimate an energy spread produced by the buncher (2.85 %). A few things are strange here; we expect the energy spread of the beam without the use of the buncher to be 0.2 %. If this was the case we would expect to see virtually no correlation, given the time resolution of ≈ 1.6 ns, with such a small energy spread. The fact that we did before the buncher was in use is quite strange. As previously mentioned the beam quality was not very good since the transmission through the

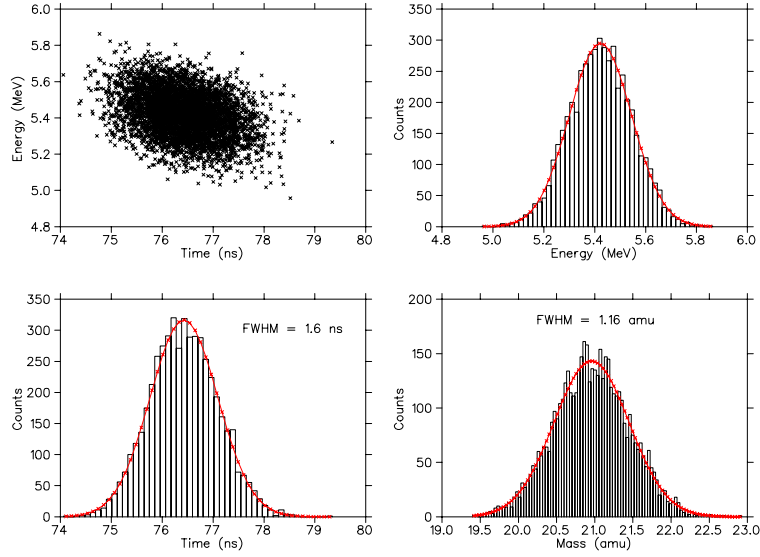


Figure 5.22: Results from the Monte Carlo simulation of an Et^2 analysis.

gas target declined with time. Its not clear if this was the result of a drift in position or energy spread from the DTL. However we can use the above difference in DSSSD energy resolutions as an estimate for the model.

Assuming the energy spread given above, the intrinsic timing resolution of the DSSSD of 1.2 ns from Wrede [80] and the energy spread of 4.7 % we can run the Monte Carlo simulation. The results are shown in Figure 5.22. The simulation reproduces the mass resolution much better than the above method using the data. Also the energy spread contributes to the observed time resolution and takes the 1.2 ns resolution from the DSSSD to 1.6 ns which is similar to that of the timing we observed. However given the peculiar beam properties before the use of the buncher more tests are needed.

We can predict the necessary time resolution for particular reactions with the Monte Carlo simulation. Two reactions in Table 2.1 were investigated. Originally 500 ps was quoted as the necessary time resolution. If we use this in our simulation along with a 2 % energy resolution, we arrive at the results for the $^{17}\text{F}(p,\gamma)^{18}\text{Ne}$ reaction shown in Figure 5.23. The mass resolution is acceptable. However much better suppression is provided by the time-of-flight measurement. The mass resolution was

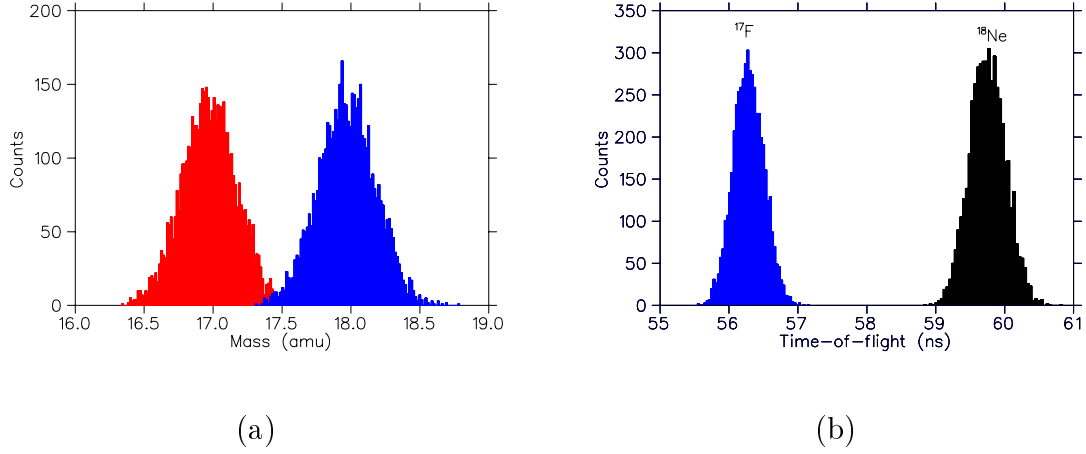


Figure 5.23: Simulated results for the $^{17}\text{F}(\text{p},\gamma)^{18}\text{Ne}$ reaction. (a) Mass plot of the ^{17}F and ^{18}Ne particles. (b) Time of flight of the ^{17}F and ^{18}Ne particles.

a little worse for the $^{26}\text{Al}(\text{p},\gamma)^{27}\text{Si}$ reaction, 0.7 u (FWHM) compared to that of the 0.5 u shown in Figure 5.23. The time spectra also showed good results due to a slightly longer time-of-flight difference. The energy chosen was that at the weakest yield strength for the two reactions, $E_{\text{lab}} \approx 233$ keV/u for ^{26}Al and ≈ 420 keV/u for ^{17}F . The width in energy of the recoils due to the gamma kick dominated the energy spread after the MCP foil. This width in energy of the recoils was assumed to be the width of a Gaussian at 10 % of its peak. A more thorough analysis might take the actual gamma branching into account.

If the additional suppression provided by the end detectors uses the local mass measurement technique, then time resolution on the order 500 ps may be required in order to provide decent suppression. However if the local time-of-flight alone does not have any associated problems with it, then 500 ps would not be required. The beam and recoils, at least in the above cases, would be well separated with 800 ps timing resolution. The bunch separation is 85 ns thus we wouldn't expect there to be problems associated with time-of-flight ambiguities. One possible problem with the time-of-flight technique by itself, would be the question of the leaky beam scattering somewhere along DRAGON, and losing energy such that it had the same time-of-flight of good recoil events. This possible problem could be investigated by going off

resonance or using ^4He in the gas target instead of H_2 .

5.2 Efficiency

The efficiency of the MCP system depends on the number of secondary electrons emitted at the foil and their transport through the mirror to the MCP. There is also the question of the MCP opacity to particles of interest due to the voltage mirror grid. In other words, beam or recoils from DRAGON must traverse the voltage mirror before being detected by a second or possibly third detector. Finally at some point there is a threshold dependance on the MCP signal and the quantum efficiency of the detector given the electron energy.

5.2.1 Optimization and Efficiency

A simple calculation of the geometrical transmission efficiency is given by the transmission probability through the MCP mirror. As shown in Figure 2.9, the particle of interest has to traverse three wire planes, one at 90° and two at 45° . The result is a 92.6 % transmission probability. To test this an alpha source was set up just in front of the MCP foil and a coincidence between the MCP and a DSSSD was taken. A few runs were done with varying foil and MCP positions in order to optimize the MCP to DSSSD transmission. The MCP was then taken out (foil still in) and a few runs were performed again. The transmission efficiency was found to be 93.0 ± 0.6 %, which agrees well with the above number.

The second number of interest is the efficiency of the MCP system itself. The geometric efficiency of a particular electron created at the foil and reaching the MCP can be shown to be 90.7 %. Reference [43] states that the MCP efficiency for electrons reaches a maximum between the energies of 500 - 1000 keV. As can be seen from Figure 2.9 the bias at the front face of the MCP lies in this range under normal operating conditions. This electron detection efficiency is very close to the open area ratio of the MCP; for the DRAGON MCP this is 63 %. With this number and the transmission through 4 wire planes, one can calculate the efficiency of detection for various numbers of secondary electrons started off at the foil. This is shown in Table 5.3. Clearly with

the average number of secondary electrons produced for heavy ions, shown previously, we expect a large number to make it to the MCP.

Table 5.3: MCP detection efficiency for various numbers of secondary electrons.

Number of Secondary electrons	Efficiency of signal production (%)
3	92.1
4	96.6
5	98.55
6	99.4
7	99.7
8	99.89
9	99.95

With an average number of electrons around 20 we expect the efficiency of the MCP to be high. Boccaccio and Vannucci [78] also investigate the detection efficiency due to mirror bias, specifically the efficiency due to the ratio, R , of the total mirror bias to the accelerating bias. An optimum ratio of 2 is given. Throughout all our runs the mirror potentials V_+ and V_- were held at the same potential, i.e. $R = 2$.

The efficiency was studied with a ^{20}Ne beam at 400 keV/u. The threshold dependence of the efficiency was investigated. It should be noted that there are also considerations with the MCP bias and fine gain adjustment on the 9327 preamp. The following results assume that the bias and gain have been adjusted such that the peak pulses from the MCP are just under the “over range” LED of the 9327. This fine gain has a range of 0.5 to 2x amplification, and can thus vary the efficiency greatly. The efficiency tests were done with a DSSSD. Under these conditions the DSSSD acted as the start signal opening a gate for the MCP stop signal. The results are shown in Table 5.4.

Where the threshold is given at the output of the amplification stage in the 9327, the actual MCP timing input signal is less than 30 mV. The errors were derived in the following way: let N_s and N_c be the the number of singles counts (total counts minus coincident counts) and the number of coincidence counts respectively. Then

Table 5.4: MCP system detection efficiency as a function of preamplifier discriminator threshold.

Threshold (mV)	Efficiency (%)
-139	$99.0^{+0.3}_{-0.4}$
-150	$99.0^{+0.4}_{-0.5}$
-180	98.1 ± 0.5
-210	96.8 ± 0.6
-250	91.4 ± 1.0
-270	87.1 ± 1.1
-300	80.6 ± 1.2
-330	72.1 ± 1.3

the efficiency is given by equation 5.16.

$$\epsilon = \frac{N_c}{N_s + N_c} \quad (5.16)$$

It can be shown that this leads to an error formula given by equation 5.17.

$$(\Delta\epsilon)^2 = \frac{N_s^2(\Delta N_c)^2 + N_c^2(\Delta N_s)^2}{(N_c + N_s)^4} \quad (5.17)$$

In the case of large N this becomes:

$$(\Delta\epsilon)^2 = \frac{N_s N_c}{(N_c + N_s)^3} \quad (5.18)$$

Equation 5.17 is shown since in the case of some runs N_s is less than 10 and Poisson errors were used. High efficiencies with heavy ions have been measured elsewhere as well (see References [55], [57] or [60]).

5.2.2 Simulation Results

5000 electrons, given initial random conditions, were started off as a point source and incremented in 0.2 mm steps. The electrons were tracked through the mirror and the

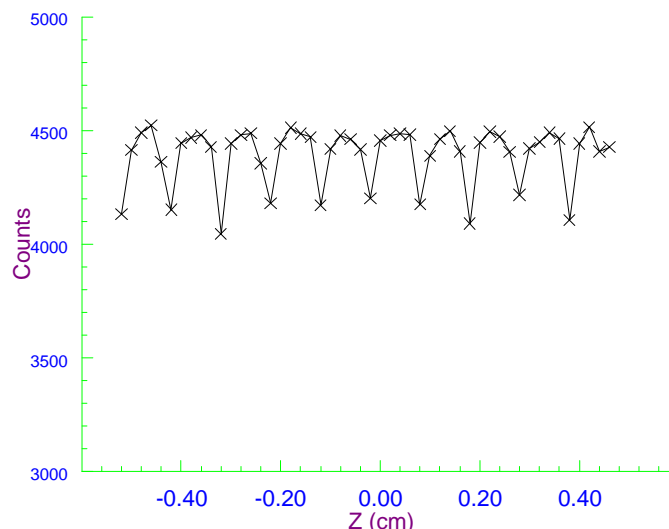


Figure 5.24: Number of secondary electrons reaching the MCP, from a point source stepped in 0.2 mm intervals. 5000 electrons were started in each case.

resulting number of electrons hitting the MCP is shown in Figure 5.24. It should be noted that in the tracking program the $20\ \mu\text{m}$ wires were simulated as $25\ \mu\text{m}$ diameter wires. This was done to avoid any problems which may arise with the potentials near the wires. Thus we may expect a slight global increase in the number of electrons reaching the MCP over the results shown. The dips in the number of counts shown in the figure, are a result of electrons whose initial Z coordinate coincided with that of a wire on grid 1. The key feature is that even for electrons created in front of the first plane of wires, we still expect a large number to reach the MCP, and thus don't expect to see any dip in MCP efficiency relating to the position where the beam hits the foil.

5.3 Position Resolution and Linearity

The position resolution may aid in the reconstruction of particle trajectories for use with a second 2d position system such as a PGAC or second MCP setup. There may

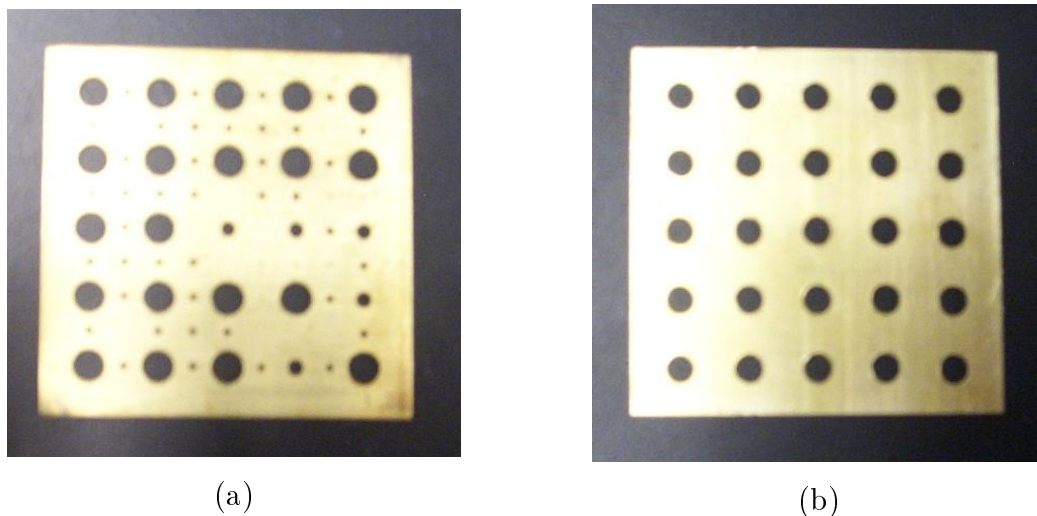


Figure 5.25: (a) Mask used to test the position resolution of the MCP/RAE system. (b) Mask used to test the 2-d linearity of the RAE.

be some suppression related to the difference in leaky beam and recoil trajectories or positions at the final focus. However there would be limitations to these setups relating to scattering in the thin MCP foil, and the IC foil if the PGAC was used.

The position resolution and linearity tests were conducted with the use of two masks placed at the foil position. Since the position resolution from the position of the foil was the parameter of interest, the thin carbon foils were mounted on the mask. These masks are shown in Figure 5.25. Figure 5.25(a) corresponds to a grid comprised of 4 mm, 2 mm, 1 mm and 0.5 mm holes with grid spacing of 4 mm center-to-center. Figure 5.25(b) corresponds to a 5 x 5 grid of 3.5 mm diameter holes with center-to-center spacing of 8 mm. Carbon foils were floated and mounted on these masks, which have thicknesses of 0.45 mm. SRIM suggests a range for 3.183 MeV alphas of $\approx 10 \mu\text{m}$.

The four position signals are shown in Figure 5.26. These signals were processed with Canberra 2003BT preamps and ORTEC 570 amplifiers. The Poisson like distribution is a result of the Poisson like chevron configuration MCP amplification, and the Poisson like distribution of the number of secondary electrons emitted.

Off-line studies were first conducted with an alpha source. One of these runs resulting from the mask of Figure 5.25(a) is shown in Figure 5.27(a); cuts may be

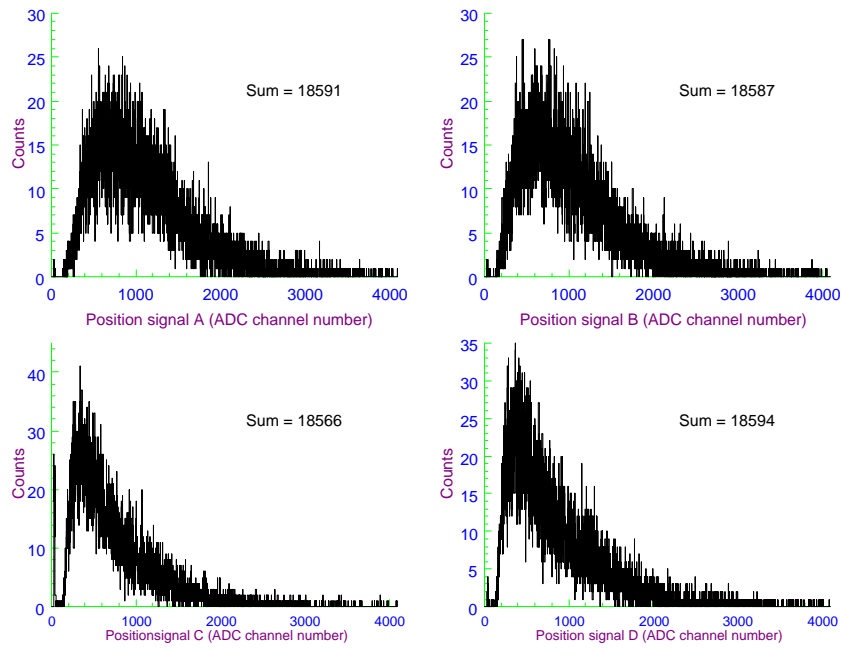


Figure 5.26: The four position signal extracted from the RAE. The Poisson-like distribution is a result of the Poisson-like behaviour of the MCP amplification and the number of secondary electrons produced.

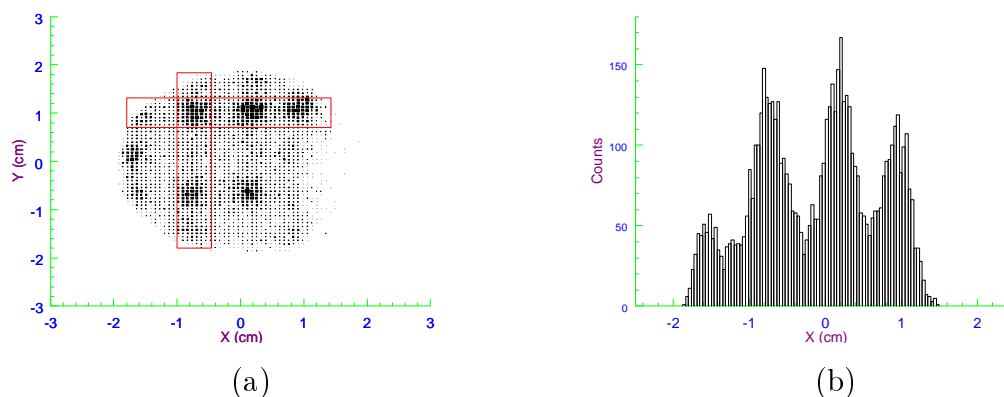


Figure 5.27: (a) 2-d spectra resulting from a mask placed at the foil position. (b) X spectra of the projection along a line of mask holes.

taken as shown by the red boxes and the resulting x-projection of the counts in a cut along y is shown along side in Figure 5.27(b). The position resolution is not very impressive at all. Any hole smaller than 4 mm could not be resolved. That is all the peaks shown have 8 mm distance between peaks (ignoring for now any non-linearity effects near the edges, which will be discussed shortly).

Shapira et al. [67] suggest that the best position resolution one expects to achieve with MCP to foil distance ≥ 5 cm is 2 mm (FWHM). Shapira et al. use an alternative electron transport system but the results should be similar. They illustrate that multiple scattering in the foil produces spreading less than 0.4 mm, and go on to suggest an alternative secondary electron spectrum which would produce the observed position spectrum. We believe the problem regarding the position resolution in our case includes a few more variables. The first of these regards the number of electrons produced at the foil; this has a great effect on the position resolution. Recall from equation 4.13 the number of secondary electrons produced was on average 23.5 for ^{21}Ne at 300 keV/u. A similar formula is given for the number of secondary electrons produced by alpha particles, in this case $C_f = 0.65$. The yield is ≈ 3.5 electrons (for ^{148}Gd alpha source). Thus on average we expect ≈ 12 (for ^{21}Ne) and ≈ 1.8 (for ^4He) electrons to reach the MCP at the given energies. Due to the small spread in transit time and longer amplifier integration times ($\approx 2 \mu\text{s}$), all these electrons will contribute to the determination of the position. That is the 12 or 1.8 electrons will average out

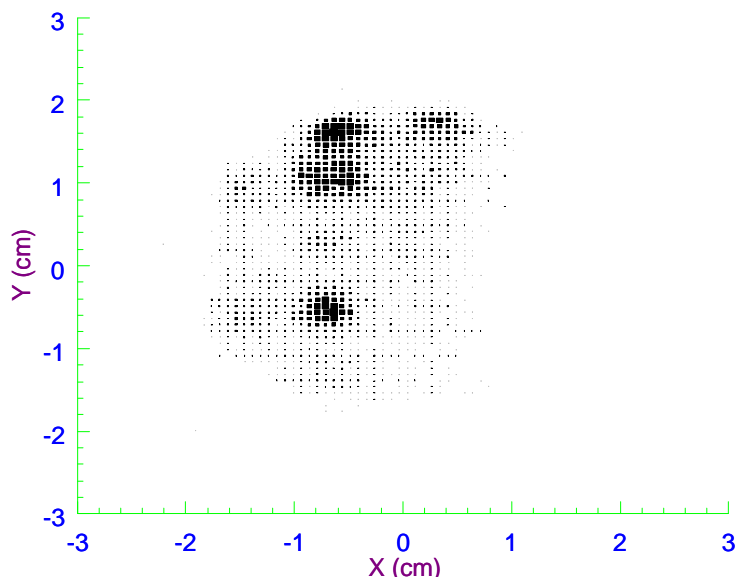


Figure 5.28: 2-d spectrum obtained with ^{21}Ne bombarding the mask shown in Figure 5.25(a).

to produce the measured position signal. We will soon see that this is a non-negligible effect. Thus a measurement of the position resolution from alphas is not a fair test of the position resolution. However it may provide a test of the simulation.

The mask shown in Figure 5.25(a) was installed and a position spectrum using ^{21}Ne beam was obtained and is shown in Figure 5.28. Due to the optics of DRAGON it was difficult to irradiate the entire foil with a uniform beam; quads 9 and 10 were turned off to produce the Figure shown. Cuts were then taken to produce the data shown in Figures 5.29(a) and (b). Clearly the position resolution is much better than that produced with the alpha source. The small middle peak in Figure 5.29(b) results from a 2 mm diameter hole in the mask. These were not as easily visible with the alpha source tests.

In order to extract the position resolution we must look at the expected position spectra from the projection of a circular hole with events randomly distributed in it. This may not be entirely accurate since the ^{21}Ne beam used was most likely not

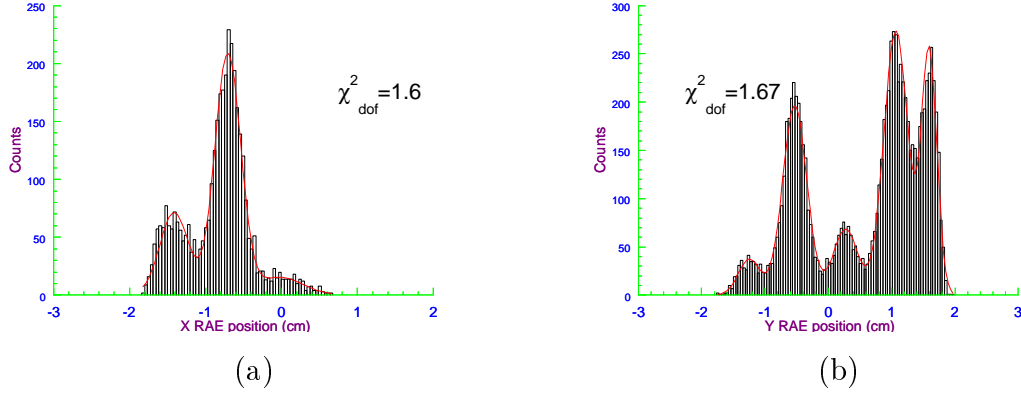


Figure 5.29: (a) Z spectrum of the projection along a line of mask holes. (b) Y spectra of the projection along a line of mask holes.

distributed uniformly. However this should give us a decent estimate of the position resolution. A more detailed analysis could measure this distribution with the MCP or DSSSD, and fold it into the position distribution. The method of determining the resolution went as follows. We randomly populate a circle of given radius, and then take each individual event, in x, and introduce Gaussian noise. The width of the Gaussian noise is then varied until the resulting width of the projected x distribution matches that of our measurement; we then claim to have position resolution given by the width of the Gaussian noise introduced. The resulting folding is shown in Figure 5.30. The Gaussian fit shown modelled the width fairly well. The result was 3.8 mm in the y direction (vertical on MCP); the z, or horizontal position on the MCP, produced two wildly different results. Two of the “blobs” from Figure 5.28 near the center were projected on the horizontal axis and the resulting position resolutions were 3.3 and 6.3 mm respectively. These results are a bit suspect since the gaussian fit to the data is not the best model. More data with high Z particles and analysis of the position signal is required.

Clearly Figure 5.29(b) demonstrates there exists a nonlinearity in the position spectrum near the edges of the MCP system. The peaks result from mask holes which are all separated by 8 mm. Although the design of the anode offers theoretical linearity, imperfections in practice lead to nonlinearities. Lampton and Carlson [40] illustrate that this nonlinearity is small compared to that seen above. Our nonlinearity

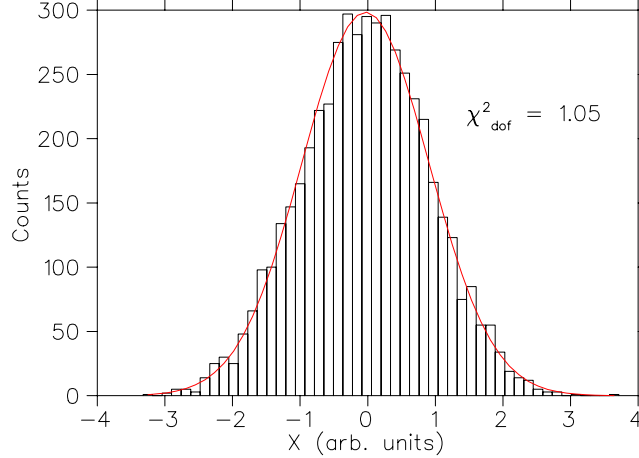


Figure 5.30: Folding of the projection of a circular hole and Gaussian noise.

is more likely a direct result of the position spread of the electrons arriving at the MCP, which will be discussed below.

5.3.1 Simulation results

For purposes of the simulation, 5000 electrons were started off near the center of the foil and given the initial conditions according to the distributions shown in Figure 4.4. The resulting spatial distribution on the MCP is shown in Figure 5.31. The y direction is along the length of the wires and thus we expect its resulting distribution to be given by the convolution of the angular distribution and the energy distribution. There is a large spread in electron position at the MCP in the z direction. We gain some understanding of this by tracking the electrons through the mirror. Figure 5.32 shows several electron trajectories started off with random initial conditions. Clearly there is a large spread in these trajectories.

References [87] and [88] discuss the focusing properties of a grid of wires on electron trajectories. The results from our Monte Carlo simulation are shown in Figure 5.33. The trajectories shown are those at the first grid, the fields around grid 2 are much stronger; we then expect this de-focusing effect will also be stronger. Shapira et al.

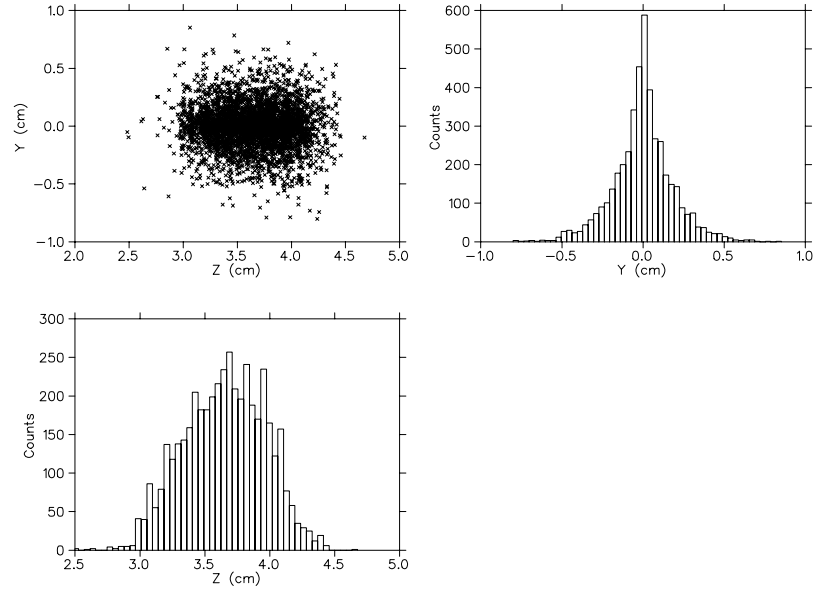


Figure 5.31: Z and Y spatial distributions resulting from 5000 electrons started off at the center of the foil.

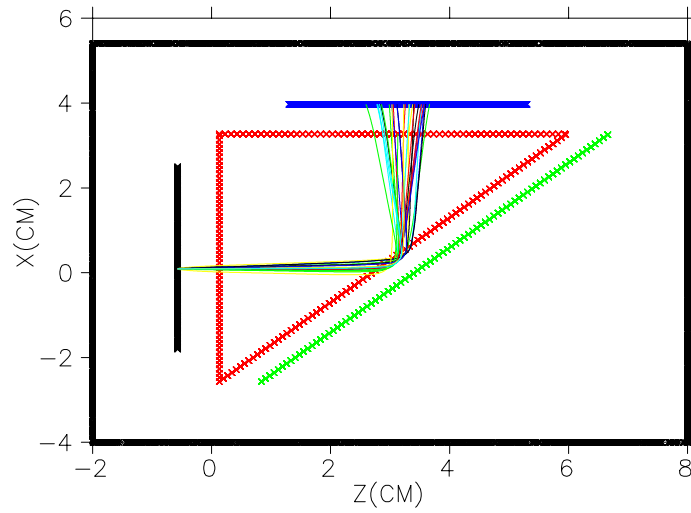


Figure 5.32: Trajectories of several electrons started out with random initial conditions.

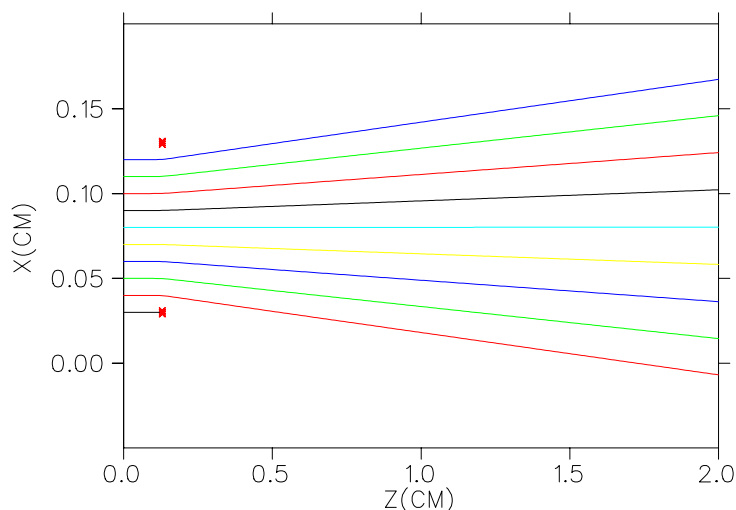


Figure 5.33: Illustration of the focusing properties of the wire plane used for the electron mirror setup. Shown are several electron trajectories and the effect the field around the wire's on their path.

[67] notes that no matter how high they increase their accelerating potentials, their position resolution does not get any better. This de-focusing mechanism resulting from the field around the wires may be the cause. We also expect there to exist chromatic aberrations as a result of small variances in the electron velocities.

Acceptable position resolution may seem not attainable. However we expect that for heavy ions several electrons should reach the MCP (around 10-12 on average). Thus, as previously mentioned, the position of the electrons should average out due to the much longer integration times compared to the spread in flight times. 20000 electrons at the same location were started out near the center of the foil. After recording the X and Z distributions of each electron reaching the MCP, 11 of these at a time were averaged, producing the expected position resolutions shown in Figure 5.34. The averaging of the electron positions at the MCP has produced position resolutions of 2.34 ± 0.13 mm and 1.23 ± 0.07 mm. A 5 % systematic error has been added to the error in the fit to account for the RELAX3D solved potentials and the tracking of the electrons through the fields. The most dramatic result from the simulation is the

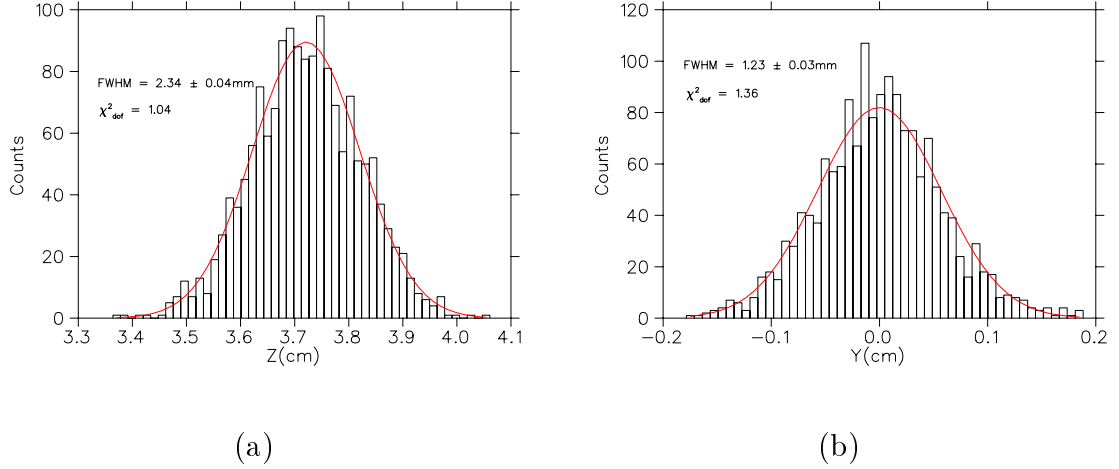


Figure 5.34: (a) Resulting Z position spectra from a point source after averaging the position of every 11th electron. (b) Resulting Y position spectra from a point source after averaging the position of every 11th electron.

prediction of poorer resolution along the Z-direction (horizontal plane) of the MCP. It also shows that the position resolution is more affected by the trajectories through the wires than that of the initial electron conditions, whose contribution is given by the Y-distribution. It should also be mentioned that an MCP-RAE system without a voltage mirror achieved position resolutions on the order 0.1 mm see Downie et al. [41]. Thus we expect the initial conditions of the electrons and the spread of the electron paths through the mirror to dominate the position resolution.

Since Rothard et al. [85] state that the prediction of the number of secondary electrons produced for heavy ions is only good to within a factor of 2, we may then ask the question if we reduce the number of secondaries produced, would this agree with the measured data? The results are shown in Table 5.5. Clearly even if we reduce the average number of electrons reaching the MCP by a factor of two or more, we still end up with better position resolution than that of the data. More work is required with the use of heavy ions in the future, to fully understand this problem.

The final result of the simulation is the prediction of the non-linearity of the MCP-RAE system. As illustrated in Figure 5.32 the spread of electrons from an initial point source is quite large. If the point is such that its image is near the edge of the

Table 5.5: Selected properties of the DRAGON MCP detection setup.

Number of electrons averaged	Z (FWHM, mm)	Y (FWHM, mm)
5	3.5	2.0
4	3.9	2.2
3	4.5	2.5
2	5.5	3.1

MCP we expect losses due to electrons missing the detector. The resulting position measurement would be shifted away from the true centroid due to these losses. The shift will be toward the center of the MCP, resulting in a non-linearity near the edges. If the centroid is within 2 mm of the edge of the MCP, along the Z-axis the simulation predicts a 1.5 mm shift of the centroid. The non-linearity which can be seen from Figure 5.28 results from a hole whose edge rests right at the edge of the MCP. If we eliminate events which are simultaneously 2 mm away from the MCP edge in Z and Y we see shifts in the position of ≈ 1.5 mm in Z and ≈ 0.5 mm in Y. This is consistent in the Z direction with that shown however it underestimates the shift in Y, which is about 3 mm from the data. This could result if the mask was not exactly centered on the MCP. Currently this does not pose a problem for the position measurement since the foil in use is 25.4 mm in diameter.

CHAPTER 6

Future Considerations

As has been pointed out, several authors have produced MCP time signals with FWHM resolutions on the order 100 ps, about 3 times better than that obtained here. However due to the straggling through the target and foil such timing would not increase suppression of beam contamination at DRAGON by a large factor. The current timing resolution is adequate given our circumstances.

There exist setups which have measured more accurate position resolutions. These employ the use of parallel electric and magnetic fields. A simple schematic of such a setup is shown in Figure 6.1. The electrons spiral around the magnetic field lines with the transport provided by the electric field. Using this setup Odland et al. [89] has achieved a position resolution of 0.7 mm. However, a possible drawback of this technique is the increased straggling due to the increased carbon foil thickness. If a thinner carbon foil can support itself and still give the same effective thickness no timing resolution would be lost. In such a setup typically the beam would traverse two wire planes, which are placed on either side of the foil to keep it from flexing in the electric field.

The use of a second fast detector has illustrated that excellent separation in a singles time-of-flight can be attained. Such a setup under normal running conditions would provide a very useful tool for mass separation. A second detector which can be used at the final focus of DRAGON should be commissioned. Such a detector might be a PGAC or another MCP. The setup with another MCP would have the advantage that the timing properties of one have already been shown to be quite good. However this would call for the introduction of another thin foil in the path of the beam. Such a foil would not degrade the timing resolution any further, but

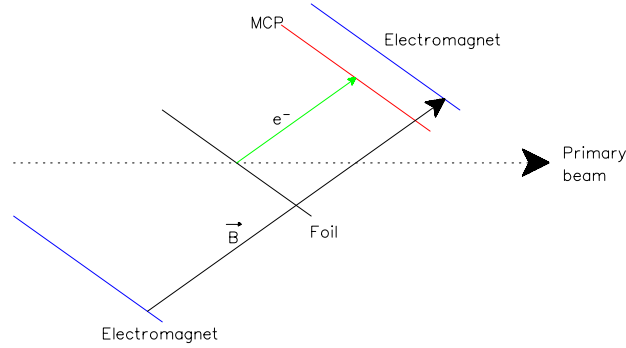


Figure 6.1: Illustration of a possible setup with magnetic fields in order to attain improved position resolution.

would introduce further straggling before the use of an energy detector. Another complication introduced involves the optics of the beam 50 cm further downstream of the current MCP. There could be acceptance problems introduced with beam spot sizes at the end of DRAGON. The current MCP is 40 mm in diameter so larger diameter foils could be used. However a 40 mm diameter, $20 \mu\text{g}/\text{cm}^2$ foil may require a supporting mesh which would introduce losses. A second MCP, if constructed like the current version, would also introduce another 7 % loss of beam transmission. The PGAC on the other hand would not have any beam acceptance problems. However its wires are $50 \mu\text{m}$ diameter wires, which implies a geometrical transparency of $\approx 86 \%$. The energy loss through the PGAC and therefore the straggling is a bit larger but still comparable to that lost through the MCP foil. For the ^{21}Ne beam used here we expect to lose $\approx 310 \text{ keV}$ through the PGAC compared to $\approx 240 \text{ keV}$ through a second MCP foil.

More detailed studies with beams are required to fully study the possible position resolution of the system. The simulations performed suggest much better resolution is attainable and may provide a valuable tool for the suppression of leaky beam.

As previously pointed out several authors have reported position resolutions similar to those our simulation predicts. One author in particular, Busch et al. [57], has attained a position resolution of 1.3 mm (FWHM) with this electron mirror setup. These results were produced with a Xe beam at an energy where SRIM estimates the stopping power to be 6.3 times larger than that of our ^{21}Ne example, leading to 6.3 times more electrons (i.e. ≈ 60) to be averaged for the position resolution.

CHAPTER 7

Conclusions

The goal of this study was to commission a fast timing, focal plane detector for the DRAGON facility to improve beam suppression. A 3394A MCP/RAE detection system sensor purchased from Quantar technologies has been commissioned for the DRAGON facility. The system has been used successfully in separating beam from recoils, using a local time-of-flight at the end of DRAGON, for the $^{21}\text{Ne}(p,\gamma)^{22}\text{Na}$ reaction at $E_{cm} = 258.6$ keV. Three major properties were studied; the timing resolution, the efficiency and the position resolution. The use of a fast photomultiplier tube in conjunction with the MCP system has demonstrated that the timing resolution is no worse than 325 ± 40 ps (FWHM). The detector efficiency itself for heavy ions has been shown to be $99.0^{+0.3}_{-0.4}\%$, and the transparency of the detection system has been shown to be $93.0 \pm 0.6\%$. The current position resolution determined with the use of ^{21}Ne beam, was found to be 3.3 mm in the horizontal plane and 3.8 mm in the vertical plane.

A simulation has been written to track the electrons produced from a thin carbon foil to the MCP. It has shown that the transit time spread is negligible compared to the intrinsic timing resolution of the detector. It demonstrates a small dip in the number of electrons reaching the MCP from the foil if the starting position corresponds to a wire of the first grid. However this small dip should not be noticeable given the large number of average electrons expected. The simulation also predicts better position resolution along the vertical axis of the MCP than the horizontal axis, and its position resolution prediction is comparable with that measured with similar electron transport detection systems. Finally non-linearity of the position signal may be understood from the results of the simulation. Further studies are necessary in order to fully understand

the poor position resolutions obtained.

A second Monte Carlo simulation has been written to model the possible suppression relating to a local mass measurement at the end of DRAGON. It has shown, along with the data obtained during this study, that superior suppression of leaky beam may be obtained from a simple time-of-flight measurement. However further consideration relating to the optics of DRAGON, and the progress of the current PGAC is required before the suggestion of a second MCP system.

APPENDIX A

MCP Mirror Assembly

The mirror setup used to deflect the secondary electrons produced at the foil, consists of four wire planes. Two of these are identical, detailed schematics of these are shown in Figures A.1-A.3. The wires are 20 μm diameter Gold plated Tungsten, with a 1 mm pitch.

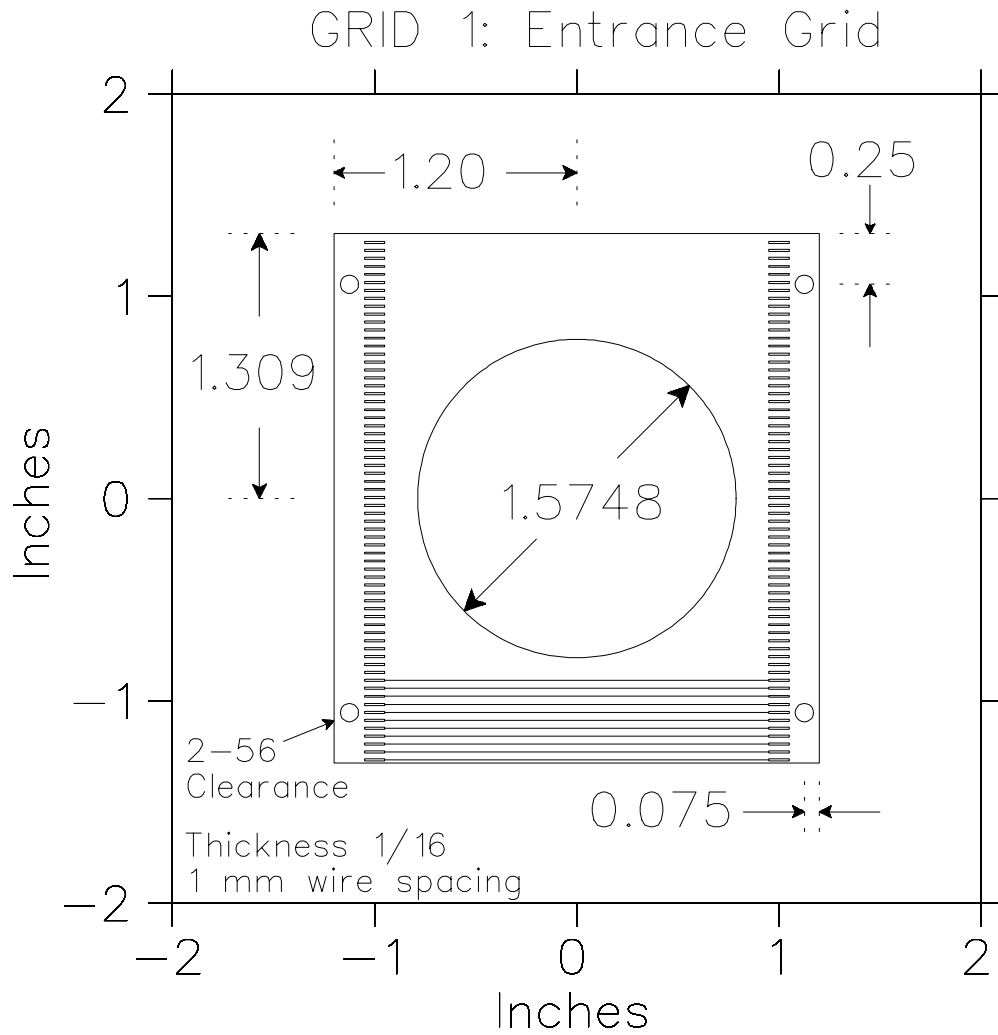


Figure A.1: Detailed schematic of the entrance grid (grid 1), with a few of the $20\ \mu\text{m}$ wires shown. All dimensions are in inches unless otherwise stated.

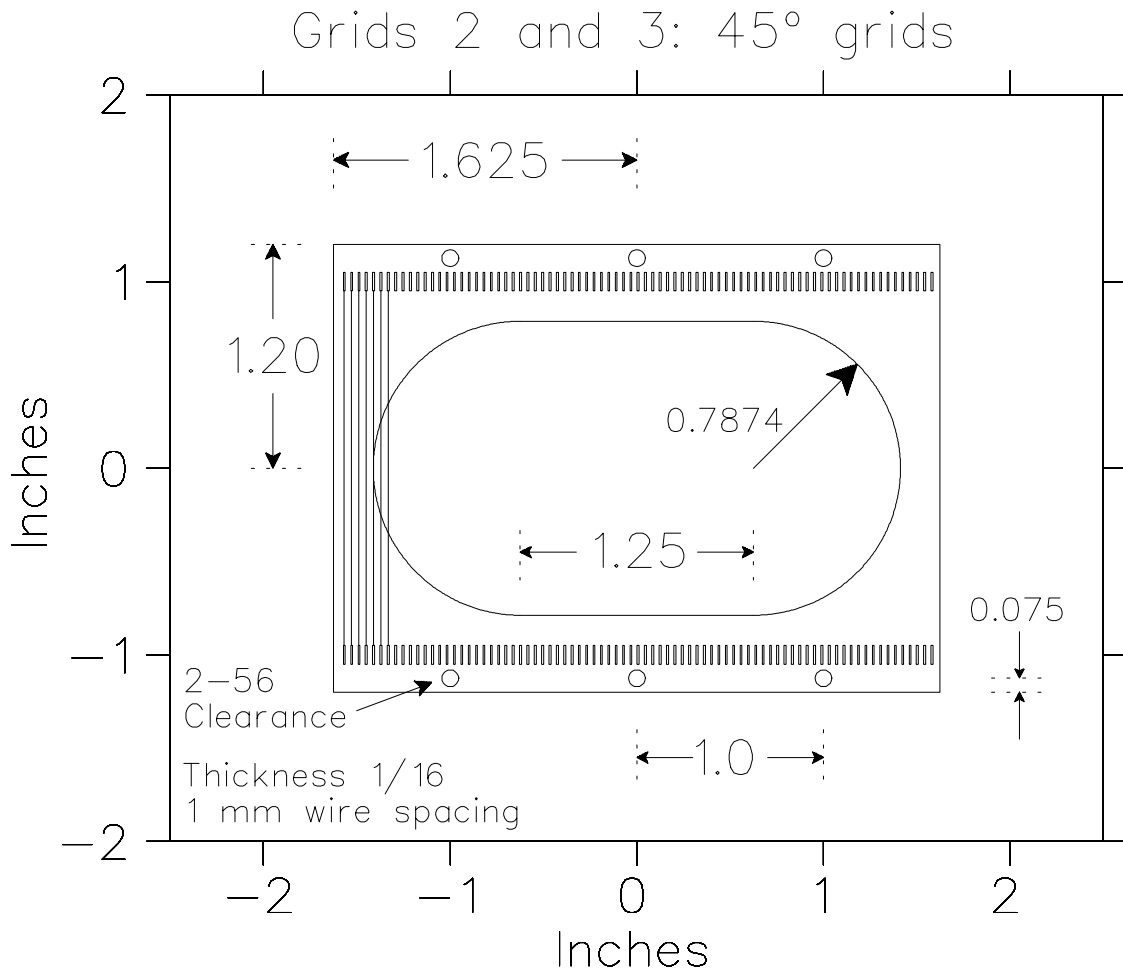


Figure A.2: Detailed schematic of the 45° grids (grids 2 and 3), with a few of the 20 μm wires shown. All dimensions are in inches unless otherwise stated.

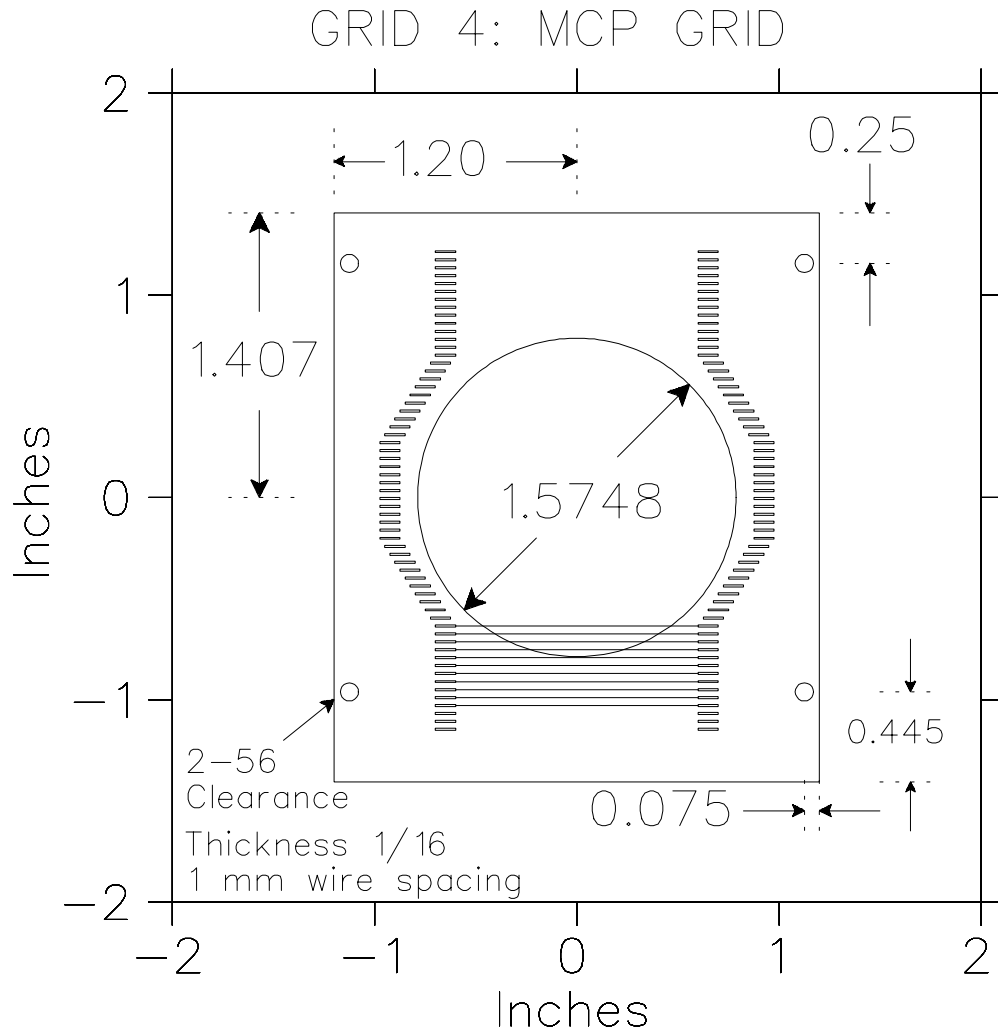


Figure A.3: Detailed schematic of the grid just in front of the MCP (grid 4), with a few of the $20\text{ }\mu\text{m}$ wires shown. All dimensions are in inches unless otherwise stated.

APPENDIX B

Mass Monte Carlo

```
*****
      PROGRAM ET_CORR
*****
*      THIS PROGRAM WILL PERFORM A MONTE CARLO OF THE      *
*      ENERGY AND TIME CORRELATION IN AN ET**2 ANALYSIS *
*      IT IS ALSO USED AS A MODEL FOR THE POSSIBLE MASS *
*      RESOLVING POWER GIVEN SEVERAL KNOWNNS SUCH AS      *
*      DETECTOR RESOLUTIONS AND BEAM ENERGY SPREAD.      *
*****
C

C VARIABLES

C
      REAL*8 X1, X2, R, Z1, TIME, TIME_MEAS, ENERGY_MEAS
      REAL*8 ENERGY, BE_WIDTH, WE_LOSS, MASS_AMU, TOT_E_RES
      REAL*8 NUM_PART, LENGTH, DET_TIME, DET_ENERGY, TIME_BW
      REAL*8 ENERGY_PART
      CHARACTER*80 FILE_NAME

C
      WRITE(*,*) 'ENTER THE MEAN ENERGY AND THE ENERGY WIDTH'
      WRITE(*,*) '(FWHM) OF THE BEAM AFTER THE FOIL (MEV)'
      READ(*,*) ENERGY, BE_WIDTH
```

```
WRITE(*,*) 'ENTER THE WIDTH OF THE MEAN ENERGY LOSS THRU'
WRITE(*,*) 'THE DSSSD DEAD LAYER (FWHM)'
READ(*,*) WE_LOSS
WRITE(*,*) 'ENTER THE COMBINED DETECTOR TIMING WIDTH (NS)'
WRITE(*,*) 'AND THE ENERGY RESOLUTION (%) BOTH FWHM'
READ(*,*) DET_TIME, DET_ENERGY
WRITE(*,*) 'ENTER THE TOF LENGTH (METERS) THE MASS(AMU)'
WRITE(*,*) 'AND THE NUMBER OF PARTICLES'
READ(*,*) LENGTH, MASS_AMU, NUM_PART
WRITE(*,*) 'ENTER THE OUTPUT FILE NAME'
READ(*,*) FILE_NAME

C

C   CONVERT INPUTS TO REQUIRED VALUES.
C

DET_ENERGY=DET_ENERGY/100.0*ENERGY
DET_TIME=DET_TIME/2.355
BE_WIDTH=BE_WIDTH/2.355
TOT_E_RES=SQRT(WE_LOSS*WE_LOSS+DET_ENERGY*DET_ENERGY)/2.355
OPEN(UNIT=57, FILE=FILE_NAME, STATUS='NEW')

C
C
C

C   THIS SECTION CALCULATES THE TIME OF FLIGHT OVER A GIVEN

C LENGTH FOR A SPECIFIED ENERGY, THE ENERGY IS DETERMINED BY A

C GAUSSIAN DISTRIBUTION OF WIDTH BE_WIDTH. THEN MIXES IN THE

C DETECTOR RESOLUTION.
```

```
C
C      CALCULATE THE TIME IN NSEC  $10^9/C = 3.333564$ 
C
C      DO I=1, NUM_PART
C
1      X1=2*RAND(0)-1.0
      X2=2*RAND(0)-1.0
      R=X1*X1+X2*X2
      IF (R .GT. 1.0 .OR. R .EQ. 0.0) GOTO 1
      Z1=X1*SQRT(-(2.0)*LOG(R)/R)
      ENERGY_PART= ENERGY+BE_WIDTH*Z1
      TIME=SQRT(MASS_AMU*931.5/2.0/ENERGY_PART)*LENGTH*3.333564
C
C      NOW PUT IN TIME RESOLUTION FROM DETECTORS.
C
C      METHOD FOR GAUSSIAN TAKEN FROM PHYSICAL REVIEW D50 PG 1284.
C
2      X1=2*RAND(0)-1.0
      X2=2*RAND(0)-1.0
      R=X1*X1+X2*X2
      IF (R .GT. 1.0 .OR. R .EQ. 0.0) GOTO 2
      Z1=X1*SQRT(-(2.0)*LOG(R)/R)
      TIME_MEAS= TIME+DET_TIME*Z1
C
C
C      THIS SECTION WILL CALCULATE THE DISTRIBUTION OF MEASURED
C
C      ENERGIES BY USING THE CONVOLUTION OF WIDTH OF THE ENERGY
C
C      LOSS IN
```

```
C      THE DSSSD DEAD LAYER AND FROM THE INTRINSIC ENERGY

C      RESOLUTION.

C
C
3      X1=2*RAND(0)-1.0
      X2=2*RAND(0)-1.0
      R=X1*X1+X2*X2
      IF (R .GT. 1.0 .OR. R .EQ. 0.0) GOTO 3
      Z1=X1*SQRT(-(2.00)*LOG(R)/R)
      ENERGY_MEAS= ENERGY_PART+TOT_E_RES*Z1

C
C
C      WRITE(57,*) TIME_MEAS, ENERGY_MEAS
      ENDDO

C
C      CLOSE(57)
      END
```


Bibliography

- [1] J. Chadwick, *Radioactivity and Radioactive Substances*. Sir Isaac Pitmann and Sons Press, London (1947).
- [2] F. Hoyle, *Essays in Nuclear Astrophysics*. Cambridge University Press, New York (1982).
- [3] E. Anders and M. Grevesse, *Geochim. Cosmochim. Acta*, 53 (1989) 197.
- [4] H. Schatz et.al., *Physics Reports*, 294 (1998) 167.
- [5] R.P. Kraft, *Ap. J.* 139 (1964) 457.
- [6] R.A. Ward, M.J. Newman and D.D. Clayton, *Ap. J. Suppl.* 31 (1976) 33.
- [7] S.A. Glasner, E. Livine, J.W. Truran, *Astropys. J.* 475 (1997) 754.
- [8] J.W. Truran, *Essays in Nuclear Astrophysics*. Cambridge University Press, New York, 1982.
- [9] S.Starrfield, *Classical Novae*. John Wiley and Sons Ltd., Oxford, 1989.
- [10] E. Chaisson, S. McMillan, *Astronomy Today*. Prentice Hall, New Jersey, 1996.
- [11] M. Wiescher, H. Schatz and A.E. Champagne, *Phil. Trans. R. Soc. Lond. A* (1998) 356, 2105-2136.
- [12] L. Bildsten, In *The many faces of neutron stars*. (ed. A. Alpar, L. Boucheri and J. van Paradijs). Proceedings of the NATO Advanced Study Institute, Lipari, Italy, September 30–October 11, 1996.

-
- [13] S.E. Woosley and T. A. Weaver, In *High Energy Transients in Astrophysics*(ed. S.E. Woosley). AIP Conference Proceedings, vol. 115.
- [14] R. Wallace and S.E. Woosley, Ap. J. Suppl. 45 (1981) 389.
- [15] T.A. Weaver, S.E. Woosley, Phys. Rep., 277 (1993) 65.
- [16] F.-K. Thielemann, T. Rauscher, C. Freiburghaus, K. Nomoto, M. Hashimoto, B Pfeiffer and K.-L. Kratz, <http://xxx.lanl.gov/abs/astro-ph/9802077>.
- [17] A.E. Champagne, M. Wiescher, Annu. Rev. Nucl. Part. Sci., 42 (1992) 39.
- [18] R.E. Laxdal et al., ISAC at TRIUMF: recent achievements and future goals. Proceedings LINAC2000, XX International Linac Conference, Monterey.
- [19] J. M. D'Auria, Journal of Radioanalytical and Nuclear Chemistry, vol. 243 no. 1 (2000) 59.
- [20] G.C. Ball et al., www.triumf.ca/people/baartman/ISAC/ball.html.
- [21] C. Jewett, *Excited States in ^{22}Mg and the $^{21}\text{Na}(p,\gamma)^{22}\text{Mg}$ Reaction* . Ph.D Thesis, in preparation, Colorado School of Mines, Golden Colorado, USA.
- [22] Dario Gigliotti, *Efficiency Calibration Through GEANT Simulation for the DRAGON γ Array at TRIUMF*. M.Sc. Thesis, University of Northern British Columbia, Prince George, B.C., Canada. (2004)
- [23] W. Liu, *Charge State Studies of Heavy Ions Passing Through Gas*. MSc. Thesis, Simon Fraser University, Burnaby, B.C., Canada. (2001) <http://www.triumf.ca/dragon/docs/wenjiethesis.pdf>.
- [24] D. Seweryniak et al., Phys. Lett. B590 (2004) 170.
- [25] S. Bishop et al., Nucl. Phys. A718 (2003) 263c.
- [26] Experimental Physics and Industrial Control System (Epics), <http://www.aps.anl.gov/epics/index.php>

-
- [27] S. McGee, D. Hunter, *Parallel Grid Avalanche Counter*. DRAGON internal report.
- [28] R. Kotte, H.J. Keller, H.G. Ortlepp and F. Stary, Nucl. Instr. Meth., A257 (1987) 244.
- [29] D. Fabris, G. Fortuna, F. Gramegna, G Prete and G Viesti, Nucl. Instr. Meth., 216 (1983) 167.
- [30] W. C. Wiley and C. F. Hendee. IRE Trans. Nucl. Sci. NS-9 (1962) 103.
- [31] <http://hea-www.harvard.edu/HRC/HomePage.html>.
- [32] D. Washington, V. Duchenois, R. Polaert, and R. M. Beasley, Acta Electronica 14 (1971) 201.
- [33] J. L. Wiza, Nucl. Instr. and Meth. 162 (1979) 587.
- [34] T. Gibson, <http://www.pvs7.com/works2.htm>.
- [35] J. E. Lees, G.W. Frasier, and D.Dinsdaleb. Nucl. Instr. and Meth. 392 (1997) 349-353.
- [36] D. T. Young, B. L. Barraclough, D. J. McComas, M. F. Thomsen, K. McCabe, R. Vigil. Journal of Spacecraft and Rockets, Vol. 29, No. 4, pp 596-598.
- [37] M. Trinczek et al., Phys. Rev. Lett. 90 (2003) 012501.
- [38] C. W. Gear, Proc. for the Skytop Conf. on Computer systems in Experimental Nuclear Phys., 1969, USAEC Conf-670301, p. 552.
- [39] G.W. Fraser and E. Mathieson, Nucl. Instr. Meth., 180 (1981) 597.
- [40] M. Lampton and C.W. Carlson, Rev. Sci. Instr., 50(9) (1979) 1093.
- [41] P. Downie, D. Litchfield, R. Parsons, D.J. Reynolds and I. Powis. Meas. Sci. Tech., 4 (1993) 1293.
- [42] Quantar Technology Inc. <http://www.quantar.com/>.

-
- [43] Technical Information Sheet, MCP Assembly, Hamamatsu, Hamamatsu city (1991).
- [44] Stanford Research Systems, <http://www.thinksrs.com/products/PS300.htm>.
- [45] ACF Metals, The Arizona Carbon foil Co. inc., 2239 E. Kleindale Road, Tucson, Arizona 85719-2440.
- [46] C.J. Kost and F.W. Jones, *RELAX3D User's Guide and Reference Manual*. TRIUMF Computing Document 1992.
- [47] C. Weber, Numerical Solution of Laplace's and Poisson's equations and the calculation of electron trajectories and electron beams, *Focusing of Charged Particles*. (ed. A. Septier), Academic Press, 1967.
- [48] H. Kume et.al., IEEE Trans. nucl. sci. Ns-33(1), 364 (1986).
- [49] H. Coombs, private communication.
- [50] The Nucleus Inc. Series II Personal Computer Analyzer. Operation and Manual (1990).
- [51] <http://www.ortec-online.com/>.
- [52] Joe Chuma. <http://www.exware.com/extrema/>
- [53] W.R. Leo. *Techniques for Nuclear and Particle Physics Experiments*. Springer-Verlag, Germany, 1987.
- [54] C.E. Rolfs and W.S. Rodney, *Cauldrons in the Cosmos*. University of Chicago Press (1988).
- [55] W. Starzecki, A.M. Stefanini, S. Lunardi and C. Signorini, Nucl. Instr. Meth. 193 (1982) 499.
- [56] R.D. Heil, J. Drexler, K. Huber, U. Kneissl, G. Mank, H. Ries, H. Stroher, T. Weber and W. Wilke, Nucl. Instr. Meth., A239 (1985) 545.

-
- [57] F. Busch, W. Pfeffer, B. Kohlmeyer, D. Schull, F. Puhlhofer, Nucl. Instr. Meth. 171 (1980) 71.
- [58] A. Oed, G. Barreau, F. Gonnemann, P. Perrin, C. Ristori and P. Geltenbort, Nucl. Instr. Meth. 179 (1981) 265.
- [59] E.C. Pollacco, J.C. Jacmart, Y. Bulmenfeld, Ph. Chomaz, N. Frascaria, J.P. Garron and J.C. Roynette, Nucl. Instr. Meth. 225 (1984) 51.
- [60] G. D'erasmo, V. Patricchio and A. Pantaleo, Nucl. Instr. Meth., A234 (1985) 91.
- [61] V.T. Koslowosky, H.R. Andrews, W.G. Davies and K. Murnaghan, Nucl. Instr. Meth., B123 (1997) 144.
- [62] R.E. Renfordt, H. Noll and K. Sapotta, Nucl. Instr. Meth., 185 (1981) 157.
- [63] J.K. Kim, Y.S. Kim, G.D. Kim, H.W. Choi, H.J. Woo, S.Y. Cho and C.N. Whang, Nucl. Instr. Meth., B140 (1998) 380.
- [64] J. Girard and M. Bolore, Nucl. Instr. Meth., 140 (1977) 279.
- [65] G. Gabor, W. Schimmerling, D. Greiner, F. Bieser and P. Lindstrom, Nucl. Instr. Meth., 130 (1975) 65.
- [66] A.N. Andreyev, V.V. Bashevoy, D.D. Bogdanov, V.I. Chepigin, A.P. Kabachenko, O.N. Malyshev, J. Rohac, S. Saro, A.V. Taranenko, G.M. Ter-Akopian and A.V. Yeremin, Nucl. Instr. Meth., A364 (1995) 342.
- [67] D. Shapira, T.A. Lewis, L.D. Hulet Jr. and Z. Cui, Nucl. Instr. Meth., A449 (2000) 396.
- [68] D. Shapira, T.A. Lewis, L.D. Hulet, Nucl. Instr. Meth., A454 (2000) 409.
- [69] M. Clampin, J. Crocker, F. Paresce and M. Rafal, Rev. Sci. Instr. 59 (8) (1988) 1269.
- [70] EG&G ORTEC, *Model 9327 1-GHz Amplifier and Timing Discriminator Operating and Service Manual*. Manual Revision A.

-
- [71] D. Fabris, G. Fortuna, F. Gramegna, G. Prete, Nucl. Instr. Meth. 216 (1983) 167.
- [72] P. Green, <http://daq.triumf.ca/nova/>.
- [73] S. Engel, *Awakening of the DRAGON*. PhD. Thesis, Ruhr-Universitat Bochum, Germany, (2003) http://www.triumf.ca/dragon/docs/sabine_thesis.pdf.
- [74] S. Bishop, *Direct Measurement of the $^{21}\text{Na}(p,\gamma)^{22}\text{Mg}$ resonant reaction rate in nova nucleosynthesis*. PhD. Thesis, Simon Fraser University, Burnaby, B.C., Canada. (2003) http://www.triumf.ca/dragon/docs/bishop_phd.pdf.
- [75] J. F. Ziegler, <http://www.srim.org>.
- [76] D.A. Hutcheon et al. Nucl. Instr. Meth. 498 (2003) 190.
- [77] J. Görres, C. Rolfs, P. Schmalbrock, H. P. Trautvetter, and J. Keinonen, Nucl. Phys. A385 (1982) 57.
- [78] P. Boccaccio and L. Vannucci, Nucl. Instr. Meth. A243 (1986) 599.
- [79] R.E. Laxdal, *Design Specification for ISAC HEBT*. TRIUMF design note (2000). <http://www.triumf.ca/download/lax/>
- [80] C. Wrede, *A Double Sided Silicon Strip Detector as an end Detector for the DRAGON Recoil Mass Separator*. MSc. Thesis, Simon Fraser University, Burnaby, B.C., Canada. (2003) <http://www.triumf.ca/dragon/docs/wredethesis.pdf>.
- [81] H. Rothard et al. Nucl. Instr. Meth., B48 (1990) 616.
- [82] L.D. Landau, E.M. Lifshitz, *The Classical Theory of Fields*. Pergamon Press, New York (1962).
- [83] H. Bruining, *Secondary Electron Emission*. Pergamon Press, New York. 1954.
- [84] J. Schou, Physical Review B22, no. 5 (1980) 2141.

-
- [85] H. Rothard, K. Kroneberger, A. Clouvas, E. Veje, P. Lorenzen, N. Keller, J. Kemmler, W. Meckbach and K.-O. Groeneveld, *Physical Review A* 41, no. 5 (1990) 2521.
- [86] C.R. Shi, H.S. Toh, D. Lo, R.P. Livi, M.H Mendenhall, D.Z. Zhang and T.A. Tombrello, *Nucl. Instr. Meth. B* 9 (1985) 263.
- [87] B. Paszkowski, *Electron Optics*. Iliffe books ltd. London (1968).
- [88] T. Bergmann, T.P. Martin and H. Schaber, *Rev. Sci. Instr.*, 60(3) (1989) 347.
- [89] O.H. Odland, W. Mittig, A. Lepine-Szily, G. Fremont, M. Chartier, M. McCormick, J.M. Casandjian, *Nucl. Instr. Meth.*, A378 (1996) 149.